Mesozoic-Cenozoic mafic magmatism in Sanandaj-Sirjan Zone, Zagros Orogen (Western Iran): geochemical and isotopic inferences from Middle Jurassic and Late Eocene gabbros

R. Deevsalar [a]*, R. Shinjo [b], M. Ghaderi [a], M. Murata[c], P.W.O. Hoskin [d], S. Oshiro [e], K. L. Wang [f], H. Y. Lee [f], I. Neill [g]

[a] Department of Geology, Tarbiat Modares University, Tehran 14115-175, Iran

[b] Department of Physics and Earth Sciences, University of the Ryukyus, Japan

[c] Department of Geosciences, Naruto University of Education, Japan

[d] Netherlands Maritime Institute of Technology, Johor Bahru, Malaysia

[e] Cabinet office, Okinawa General Bureau, 376-3 Kanegusuku, Itoman, Okinawa 901-0303, Japan

[f] Institute of Earth Sciences, Academia Sinica, Nankang, Taipei 115, Taiwan

[g] School of Geographical and Earth Sciences, University of Glasgow, Lilybank Gardens, Glasgow G12 8QQ, Scotland

* Corresponding author: Reza Deevsalar

E-mail: Deevsalar@modares.ac.ir

ABSTRACT

One of the consequences of Neo-Tethys ocean subduction beneath the Central Iranian Microcontinent (CIMC) is the development of rare gabbroic intrusions in the Malayer-Boroujerd Plutonic Complex (MBPC) located in the Sanandaj-Sirjan Zone (SaSZ) of the Zagros Orogenic belt. The MBPC is a suite of extensive felsic and lesser mafic magmatic products in the northern SaSZ with geochemical signatures of arc-like magmatism during the Middle Jurassic (Ghorveh-Aligudarz arc) and intraplate type in the Late Eocene. Middle Jurassic gabbros (non-cumulate and cumulate) have low-Ti concentrations (< 1 wt. %) and quite uniform isotopic compositions (initial $^{87}Sr/^{86}Sr$: 0.7035–0.70593 and εNd(t): -6.18–-0.7), enriched LILE relative to HFSE, variable fractionation between the LREE and HREE $((La/Yb)_{cn}$: 2.27–7.45) and both negative to positive Eu anomalies. These distinctive features of arc-type magmatism are consistent with a subduction-modified mantle source for these rocks. Trace element and REE models indicate ~ 15% melting of a metasomatized amphibole-bearing garnet-spinel lherzolite (garnet:spinel ~ 7:3) in the sub-arc mantle wedge. The cumulate gabbros and non-cumulates belong to common liquid line of descent, with complementary trace element patterns. Much of the variation between samples can be modeled by fractional crystallization (FC) of a common parent; only one cumulate gabbro from this suite exhibits isotopic evidence of contamination, probably by Rb-depleted crustal materials. The Late Eocene gabbros have relatively high-Ti (>1 wt. %) and display isotopically depleted Sr-Nd values (initial $^{87}Sr/^{86}Sr$: 0.7044–0.7087, $\varepsilon_{Nd}(t)$: 1.9–+3.2, barring one crustally-contaminated sample). OIB-like trace element characteristics such as enriched HFSE, and only minor enrichment of LILE and LREE, reflect a within-plate character and asthenospheric source. Trace element modeling indicates small degree melting ($f_{melting}$: 0.05) of upper mantle lherzolite (garnet:spinel ~ 3:1) followed by higher degree melting ($f_{melting}$: 0.15) at shallower depths (garnet:spinel ~4.5:2). The Eocene parental magma underwent FC of olivine and clinopyroxene. We propose that Eocene asthenospheric upwelling was triggered by slab tearing

in response to slab-rollback, which is elsewhere reported to have triggered a ‘flare-up’ of extension-related magmatism across Iran. Three stages of tectono-magmatic evolution in the Ghorveh-Aligudarz arc segment of the N-SaSZ are represented by: 1) arc-like magmatism during active subduction of the Neo-Tethys seaway at Middle Jurassic, 2) magmatic quiescence during an interval of shallow-angle or highly oblique subduction during the Cretaceous–Paleocene, and 3) asthenosphere melting during slab tearing shortly before the onset of the Arabia-Eurasia collision.

Keywords: Zagros Orogen, Neo-Tethys Ocean, Ghorveh-Aligudarz arc, Gabbro, trace element modeling, convecting enriched asthenosphere, Mantle wedge

1. Introduction

Changes in the rate and angle of subduction through time appear to be primary factors controlling mantle or crustal melting processes in continental arc settings (e.g., Stern 1989; Pearce et al., 1990; Davidson, 1996; Macdonald et al., 2000; Winter, 2001). The magmatic products of continental subduction zones can be derived from the subducting crust, the convecting mantle wedge, continental lithospheric mantle or the continental crust (Moyen et al., 2001; Hofmann, 2005; McDermott et al., 2005; Zellmer et al., 2005). Of these igneous products, the mantle-derived mafic rocks are crucial in helping us understand the tectono-magmatic evolution of continental subduction zones, since they are our best window on mantle sources and melting conditions. This fact is highlighted by the study of rare mafic intrusive rocks from the Sanandaj-Sirjan Zone (SaSZ), W Iran. The Sanandaj-Sirjan Zone (SaSZ), the Urumieh-Dokhtar Magmatic Arc (UDMA) and the Zagros Folded-Thrust Belt (ZFTB) are three major terranes of the Zagros Orogen located in the extensive Tethyan orogenic belt of western Asia (Fig. 1a). The widespread presence of mappable plutonic rocks in the Mesozoic–Cenozoic SaSZ and the Cenozoic UDMA, is one of the major geological features of the Zagros Orogen. These plutonic rocks lie in parallel linear bands (Fig. 1a). Plutonic rocks in the SaSZ are of Middle Jurassic (Ahmadi-Khalaji et al.,

2007; Ahadnejad et al., 2010; Shahbazi et al., 2010; Mahmoudi et al. 2011, Agard et al., 2011, Sepahi et al., 2014), Middle to Late Cretaceous (Azizi and Jahangiri, 2008; Azizi and Asahara, 2013) or Eocene (Nogole Sadat and Houshmandzadeh, 1993; Mazhari et al., 2009) age. These intrusive bodies are mostly granitoids but minor mafic rocks are also present. Most geologists consider that the plutonic rocks from the Zagros Orogen are derived from subduction-modified mantle sources, ultimately the product of Neo-Tethyan plate subduction beneath the Central Iranian Micro-Continent (CIMC) in the Mesozoic and Cenozoic (e.g., Ahmadi-Khalaji et al., 2007; Omrani et al., 2008; Ghalamghash et al., 2009a, Ghalamghash et al., 2009b; Shahbazi et al., 2010; Ahadnejad et al., 2010; Mahmoudi et al., 2011; Esna-Ashari et al., 2012; Azizi et al., 2013, Chiu et al., 2013). Other more complicated models for Mesozoic-Cenozoic tectonic include that of Azizi et al. (2015), who ascribed the generation of the mafic plutonic rocks from southwest of Ghorveh (Fig. 1b) to the opening of a back-arc basin within an intra-oceanic subduction-arc system which then collided the SaSZ during the Late Jurassic (Azizi et al., 2014). Nevertheless, one of the main topics of continuing debate amongst regional geologists concerns the apparent decrease in abundance of mafic plutonic rocks southwards within the SaSZ, yet little attention has been given to the geochemistry and petrogenesis of these less abundant facies. In some localities, the SaSZ felsic rocks were intruded by mafic magma now preserved as stocks, dykes, mega-enclaves and microgranular enclaves (Ghalamghash, 2003; Ahmadi-Khalaji et al., 2007; Sepahi, 2008; Ghaffari et al., 2013; Kheirkhah et al., 2013). The focus of this study is the Malayer-Boroujerd Plutonic Complex (MBPC) which is a suite of widespread Middle Jurassic granitoid intrusions and associated gabbro-dioritic rocks and Late Eocene gabbros (in the forms of intrusions and dykes) in the northern SaSZ (N-SaSZ). Because of different strategies required for different petrogenetic scenarios, detailed discussion of the geochemistry and petrogenesis of whole spectrum of compositions from the MBPC (including granitoids and gabbro-dioritic dykes) falls outside the scope of the present paper. Our goal is to investigate the key petrological, elemental

and isotopic signatures of the MBPC mafic intrusive rocks (mainly non-cumulate rocks) in order to better constrain the tectono-magmatic evolution of this part of the SaSZ.

2. The Malayer-Boroujerd Plutonic Complex (MBPC)

The NW-SE striking MBPC outcrop is approximately 10 km wide by 100 km long in the northern part of the SaSZ (Fig. 1a, b). The main episode of magmatism in the Middle Jurassic generated predominantly felsic magmas which were emplaced into Triassic–Jurassic metamorphic crust (Ahmadi Khalaji et al., 2007; Ahadnejad et al., 2010). The presence of inherited zircons with Proterozoic–Paleozoic ages in the MBPC granitic rocks (Ahadnejad et al., 2010) indicates that this part of the SaSZ was also intruded through metamorphosed sediments, similar to the Golpayegan Neoproterozoic rocks which contain old detrital zircons (e.g., Hassanzadeh et al., 2008; Saki, 2010). According to published age data, the subduction-related felsic plutonic rocks of the northwestern part of the MBPC (NW-MBPC, Fig. 1c) belong to the Middle Jurassic (161.95 ± 0.7–186 ± 0.3 Ma; U-Pb on zircons; Ahadnejad et al., 2010). Likewise, U-Pb zircon dating of the felsic plutonic rocks from southeastern areas (S-MBPC, Fig. 1c) gave ages of 169.6 ± 0.2–171.3 ± 1.1 Ma (Ahmadi-Khalaji et al., 2007). New zircon U–Pb ages acquired by laser ablation-inductively coupled plasma mass spectrometry (LA-ICP-MS, section 4.1) for the MBPC mafic intrusive rocks indicate the mafic magmatism occurred in two stages, first in the Middle Jurassic and the other in Late Eocene time (section 4.1). The youngest known granitic rocks of the Gousheh–Tavandasht granite body have similar ages to the youngest mafic rocks (34.9 Ma, Mahmoudi et al., 2011). In some places, the MBPC granitoids host mafic dykes, however, they do not occur in direct contact with mafic intrusive rocks. Mafic intrusive rocks are more typically found as discrete bodies hosted between the main granitic intrusions (Supplementary Item 1, Fig. 1), but they neither cross-cut each other nor mafic-intermediate dykes.

Within the MBPC, some of the mafic intrusive rocks are not mappable at the scale of Fig. 1c. The largest recognized outcrop occurs at Tangsaran Hill (Fig. 1c, 2 km^2, Supplementary Item 1,

Fig. 1). The mafic intrusive bodies do not show any systematic age distribution pattern, but as shown in this map, do mainly occur to the east of the main granitic body.

3. Petrography

The MBPC mafic rocks are texturally and mineralogically diverse, and at an outcrop scale may exhibit cumulate layering. From among the collected samples, thirty representative rocks were selected for petrographic study. The mafic intrusions of both ages comprise two main groups of samples with cumulate and non-cumulate textures and range in composition from olivine gabbro- to hornblende- and hornblende-clinopyroxene bearing gabbros (after Streckeisen, 1976). However, those olivine gabbros are divided into two groups based upon the abundances of olivine and clinopyroxene. Despite being similar mineralogically, the Middle Jurassic cumulate and non-cumulate gabbros related to the same rock type categories show differences to those Late Eocene gabbros in terms of texture and fabric (Table 1).

3.1. Cumulate gabbros

The cumulate gabbros are found in both Middle Jurassic and Late Eocene suites. By the existence of cumulate texture, poikilitic hornblende and orthopyroxene oikocryst, coarse grained olivine and Ca-rich plagioclase cumulus phases, cumulate gabbros can be distinguished clearly from non-cumulate ones. Besides textural and mineralogical evidence indicating a cumulative nature, they show distinct geochemical characteristics that will be further discussed in the later sections. They have two end-members of plagioclase-rich and olivine-rich composition (shown by stars in Table 1). In these rocks, early cumulate phases including subhedral plagioclase and olivine surrounded by interstitial, post-cumulate hornblende and orthopyroxene oikocrysts. Of the four cumulate gabbros selected from the Middle Jurassic suite, two are hornblende-plagioclase gabbro (M_{07} and M_{14}, Table 1) and two others are olivine gabbro (M_{44} and BR_{Q2}, Table 1). Among the late Eocene gabbros, only two samples with hornblende-clinopyroxene gabbro (i.e. GU) and olivine gabbro (i.e. M_{41}) composition show cumulate texture which are described

126 in Table 1. In contrast to the cumulate hornblende gabbros with simple mineralogy (Hbl + Pl ±
127 Bio ± Fe-Ti Oxides, Table 1), olivine gabbro cumulates from both suites show a complex miner-
128 alogy due to presence of accessory minerals and inclusions. In contrast to olivine gabbro cumu-
129 lates, the hornblende gabbro and hornblende-clinopyroxene gabbros are slightly altered. The se-
130 ricitization of plagioclase and uralitization of hornblende respectively produced sericite, biotite
131 and chlorite in these samples (Table 1).
132 The Middle Jurassic olivine gabbro cumulates (i.e. sample BR_{Q2} and M_{44}) are mesocratic rocks of
133 medium grain size (0.1-2 mm, Hibbard, 1995), composed of olivine (20 and 30 vol%), plagio-
134 clase (40 and 35 vol%), hornblende (30 and 15 vol%) and clinopyroxene (5 and 20 vol%) ± spi-
135 nel, pyrite, apatite, ilmenite (~ 1–3 vol.%) (Supplementary Item 1, Fig. 2a, b). In sample M_{44}
136 spinel either occurs as large inclusions within olivine (Supplementary Item 1, Fig. 2c) or co-
137 exists with ilmenite and pyrite in cracks of olivine. Sericite and chlorite are both the secondary
138 minerals formed as alteration products of plagioclase (sericitization) and horn-
139 blende/clinopyroxene (uralitization) in slightly altered BR_{Q2} (Supplementary Item 1, Fig. 2a).
140 Amphiboles have granular habit, sometimes with poikilitic textures in these rocks. Thin layers
141 and clots rich in amphibole and chlorite in the sample/ location M_{44} represent reaction of plagio-
142 clase and olivine with the interstitial liquid to form amphibole as suggested for other early-
143 formed cumulates (e.g., Meurer and Claeson, 2002).
144 The Late Eocene olivine gabbro cumulate (i.e. sample M_{41}) has fine grains (0.1-1 mm, Hibbard,
145 1995) composed of olivine (~ 35 vol%), plagioclase (~ 40 vol%), hornblende (~ 15 vol%) and
146 clinopyroxene (~ 10 vol%) ± magnesio-chromite, ilmenite and hematite (< 5 vol.%) (Supplemen-
147 tary Item 1, Fig. 2d). Olivine is enclosed with plagioclase laths or interstitial hornblende, often
148 anhedral and with a well-developed reaction rim composed of andesine-labradorite and chlorite
149 where in contact with Ca-rich plagioclase. Figure 2e shows spinel grains (magnesio-chromite)
150 with hematite and chlorite concentrated in olivine.

3.2. Non-cumulate gabbros

Like the cumulate gabbros, samples with olivine gabbro (i.e. BR_{18}) and hornblende gabbro (i.e. BRQ_1, M_{44b}) composition are found within the Middle Jurassic non-cumulate rocks. Sample M_{41b}, with higher modal clinopyroxene (up to 16%), is thus a clinopyroxene-bearing hornblende gabbro. The Middle Jurassic non-cumulate olivine gabbro (BR_{18}) is fine grained, composed of olivine (~ 8 vol%), plagioclase (~ 45 vol%), hornblende (~ 28 vol%), clinopyroxene (~ 10 vol%) and orthopyroxene (< 5 vol.%) ± quartz, apatite, ilmenite and zircon (< 3 vol.%). The non-cumulate hornblende gabbros are dark in colour, with an equigranular texture, and consist mainly of hornblende and Ca-rich plagioclase as the main phases and minor amount of Fe-Ti oxides, zircon and apatite with or without clinopyroxene. Hornblende is present as anhedral crystals (up to 2mm), which contain plagioclase and ilmenite inclusions. Subhedral to euhedral plagioclase ranging from 1-3 mm in length, does not display chemical zonation. Clinopyroxene is unzoned and contains inclusions of plagioclase. The plagioclase and hornblende in Middle Jurassic non-cumulate hornblende gabbros are slightly altered. The alteration products are sericite and chlorite (Supplementary Item 1, Fig. 2g, h). Different types of non-cumulate gabbros of Late Eocene age are represented by olivine gabbro (M_{25a}), olivine free hornblende-clinopyroxene gabbros (BR_{13b}) and hornblende gabbros (BR_{13a}, BN_{07b} and BR_{02b}) (Table 1). Compared with the Middle Jurassic non-cumulate olivine gabbro (BR_{18}), sample M_{25a} is a porphyritic rock composed of higher modal clinopyroxene (up to 15%) and olivine (up to 10%). In this sample, large euhedral hornblende and plagioclase (slightly sericitized) in this sample are surrounded by equant, subhedral to euhedral fine-grained groundmass of olivine, hornblende (slightly chloritized), clinopyroxene and plagioclase (Supplementary Item 1, Fig. 2f). The dark, medium- to fine-grained hornblende gabbros and hornblende-clinopyroxene gabbros form bodies up to a maximum of 500 m across, containing plagioclase (35–55 vol%), orthopyroxene (0–5 vol%), hornblende (33–45 vol%; slightly chloritized in sample M_{41b}), biotite (0–7 %), clinopyroxene (0–15 vol%) ± apatite, zircon, hema

tite and ilmenite (< 3 vol%) (Supplementary Item 1, Fig. 2g-i). Tabular plagioclase occurs either as a subhederal separate phase or enclosed within poikilitic amphiboles (Supplementary Item 1, Fig. 2j). There are little textural differences between Middle Jurassic non-cumulate hornblende gabbros and hornblende-clinopyroxene gabbros with those from Late Eocene, which are represented in Table 1.

4. Results

4.1. New U-Pb zircon age for gabbroic intrusions

Two samples of gabbroic intrusions from SE-MBPC (BR_{18}, BN_{07b}) and two from NW-MBPC (M_{44b} and M_{25a}) were chosen for LA-ICP-MS U-Pb zircon dating. The analytical methods and procedure are in Supplementary Item 2, Section A. Zircon U–Pb ages for approximately 141 analytical points on zircon grains are given in Supplementary Item 3, Table 1. The selected zircons were mostly transparent and colorless with no evident inclusions and show oscillatory zoning (Fig. 2) indicative of magmatic origin (Hoskin and Schaltegger, 2003).

Forty-two points from sample BR_{18} have $^{206}Pb/^{238}U$ ages clustered between 158 and 173 Ma, giving a weighted mean age of 168.54 ± 0.85 Ma (2σ) (Fig. 3a; Supplementary Item 3, Table 1), apart from two analyses with younger ages, likely due to large analytical uncertainties (spots. 15, 21). Seventy-one points from sample M_{44b} gave a weighted mean $^{206}Pb/^{238}U$ age of 169.6 ± 2.6 Ma (2σ) (Fig. 3b; Supplementary Item 3, Table 1). These Middle Jurassic ages are consistent with zircon U–Pb ages of felsic magmatism throughout the SaSZ (Ahmadi-Khalaji et al., 2007; Ahadnejad et al., 2010; Mahmoudi et al., 2011; Esna-Ashari et al., 2012; Chiu et al., 2013; Sepahi, 2014) and imply that gabbroic intrusions were closely related in time and space to granitic magmatism.

Of the seventeen points analyzed for sample BN_{07b}, 13 points gave a concordia age of 40.3 ± 6.7 Ma (Fig. 3c; Supplementary Item 3, Table 1), and four zircons yield significantly higher ages (spots: 3, 6, 9, 10; Supplementary Item 3, Table 1) albeit with large uncertainties. Analyses of

fourteen grains from sample M_{25a} yielded a weighted mean age of 38.5 ± 2 (Fig. 3d; Supplementary Item 3, Table 1). On the basis of recently published data and our new U-Pb dating, two periods of magmatic activity have been identified in the N-SaSZ, one around 170 Ma and the other around 40 Ma, with no published evidence for significant magmatic activity during the Cretaceous and Paleogene.

4.2. Major element oxides

The whole-rock major element composition of the MBPC gabbros is given in Table 2. The analytical methods are in Supplementary Item 2, Section B. The MBPC gabbros yielded low loss on ignition (LOI) values (mostly < 3 wt. %) indicating low levels of hydrothermal alteration. Moreover, the positive correlation between mobile trace elements (sensitive to alteration) and immobile elements (such as Nb vs. Rb and Yb vs. Rb; Supplementary Item 1, Fig. 3) indicate insignificant sub-solidus alteration in both suites. The secondary minerals generated in slightly altered gabbros are listed in Table 1.

4.2.1. Middle Jurassic low-Ti gabbros

The Middle Jurassic MBPC gabbroic intrusions display a sub-alkaline character on the total alkalis-silica diagram (TAS, Fig. 4a) (Irvine and Baragar, 1971). On a FeO_T/MgO vs. SiO_2 plot (Fig. 4b), these rocks have mainly calc-alkaline characteristics, however some samples exhibit transitional tholeiitic affinity. These rocks have variable $Mg^{\#}$ ~ 0.45–0.66 and Al_2O_3 concentrations (~13–29 wt. %), a product of their heterogeneous cumulate and non-cumulate textures, Na_2O > K_2O (Table 2) and low FeO_T (up to 11 wt. %). As they are characterized by low TiO_2 (<1 wt. %) concentrations overall, these Jurassic samples will be called the *Low-Ti gabbros*.

4.2.2. Late Eocene high-Ti gabbros

The Late Eocene gabbroic intrusions have an alkaline affinity on the TAS diagram (Fig. 4a). Of eight samples, three non-cumulate gabbros with highest FeO_T concentrations display transitional tholeiitic affinity (BR_{02b}, BR_{13a} and BR_{13b}). The samples from this group have lower $Mg^{\#}$ ~ 0.27–

226 0.46 and Al_2O_3, similar Na/K ratios, but higher FeO_T (10–15 wt. %) relative to the Low-Ti gab-
227 bros (Table 2). They are characterized by high TiO_2 (1.9–5.5 wt. %) and will henceforth be
228 called the *High-Ti gabbros*. The high-TiO_2 in these rocks is due in part to the presence of high-Ti
229 hornblende (kaersutite) and ilmenite in hornblende gabbros and kaersutite + high-Ti clinopyrox-
230 ene in hornblende-clinopyroxene gabbros (Supplementary item 3, Table 2a, b).

231 **4.3. Trace elements**

232 The whole-rock trace element composition of the MBPC gabbros is given in Table 2. The analyt-
233 ical methods are reproduced in Supplementary Item 2, Section B. The trace element composi-
234 tions of the MBPC gabbroic intrusions clearly correlate with the classification/groups defined by
235 age and major element composition. The MBPC mafic plutonic rocks divide into two broad
236 groups. These sample groups can be readily recognized based on their Zr and Nb contents. The
237 absolute abundances of Nb and Zr in high-Ti gabbros (Nb: 16.2–37.54 ppm, Zr > 90 ppm) are
238 higher than older low-Ti type (Nb: 1–9.36 ppm, Zr: 25–77.8 ppm) samples. Trace element data
239 are plotted on primitive mantle-normalized and chondrite-normalized diagrams in Figs. 5 and 6,
240 and discussed in the sections below.

241 *4.3.1. Middle Jurassic low-Ti gabbros*

242 The low-Ti gabbros are split into two groups characterized by either (1) distinctive negative Nb-
243 Ta and Sr anomalies on normalized plots (Non-cumulate gabbros, Fig. 5a); or (2) by those with
244 positive Sr and negative Zr anomalies (Cumulate gabbros, Fig. 5b). In general, the MBPC low-Ti
245 gabbros are slightly enriched in light rare earth elements (LREE) and show variable degrees of
246 LREE/HREE fractionation ($(La/Yb)_{cn}$ values in Fig. 6a; Table 2), similar to continental arc
247 magmas. The MBPC cumulate gabbros exhibit lower total REE concentration than those in non-
248 cumulate gabbros. Total REE concentrations decrease between the non-cumulate gabbros and the
249 cumulate gabbros (Fig. 6a), indicating an important role for fractionation of the phases that ex-
250 clude REE (bulk distribution coefficients (D) for REEs < 1). In other words, the compositional

heterogeneity preserved in these rocks is mainly controlled by the composition of their constituent minerals rather than by the source or partial melting conditions. Among the cumulate gabbros, sample M_{44}, with its flat chondrite-normalized REE-pattern and low REE concentrations, contains a high abundance of accumulated olivine in which all the REE are strongly incompatible. The non-cumulate gabbros show slightly LREE-enriched chondrite-normalized patterns ($(La/Yb)_{cn}$ ratios vary from 2.3 to 6.1) with negative Eu anomalies (Eu/Eu* = 0.49–0.63, except for the small positive anomaly of BR_{18} with Eu/Eu* = 1.19, Fig. 6a). In contrast, there are distinctive positive Eu anomalies (Eu/Eu* = 1.28–1.76, Fig. 6b) in cumulate gabbros. The covariation of Eu and Sr anomalies on the trace element patterns of the two groups of low-Ti gabbros strongly indicates a role for plagioclase fractionation in non-cumulate gabbros and accumulation for the latter.

4.3.2. Late Eocene high-Ti gabbros

These gabbros have no negative Nb-Ta anomaly, and exhibit variable enrichment or depletion in the LILE (Figs. 5c, d). Among the non-cumulate gabbros (Fig. 5c), two samples (i.e. M_{25a} and BR_{2c}) are characterized by lower $Mg^{\#}$ (< 0.4), Ni, Cr, Co and Zr and higher Sr (> 450 ppm) than others ($Mg^{\#}$ > 0.4, Sr≈ 300 ppm, Table 2). Those samples plotted in Fig. 5d comprise two cumulate gabbros (M_{41} and GU) with low Zr concentrations and $Mg^{\#}$ values (Table 2). The high field strength elements (HFSE: Zr, Hf, Ti) show enrichment relative to nearby REE on Figure 5, and the Nb–Ta enrichment relative to the LREE is comparable to ocean island basalts (OIB; Weaver, 1991; Altunkaynak and Dilek, 2013). Ti enrichment in two cumulate gabbros (Fig. 5c, M_{41} and GU) may relate to accumulation of Fe-Ti oxides (Supplementary item 1, Fig. 2e) or concentration of Ti in major constituent minerals of cumulate gabbros (i.e. hornblende and clinopyroxene). The remaining samples (BR_{02}, BR_{13a} and BR_{13b}) form concave up profiles in primitive mantle normalized trace element patterns (Fig. 5c). The high Zr and Nb contents in this group are further consistent with the within-plate character of these rocks (Tatsumi et al., 1995). The high-Ti gab

bros are moderately enriched in LREE and show limited degrees of LREE–HREE fractionation ($(La/Yb)_{cn}$ = 5.95–10.39). The total REE abundances decrease between the non-cumulate and cumulate gabbros. In contrast to cumulate gabbros with significant positive Eu anomalies (1.22–1.32), the non-cumulate gabbros have no or only slight positive or negative Eu anomalies (Eu/Eu* = 0.87–1.13, Fig. 6b). The positive Eu-anomaly in cumulate gabbros indicates low oxygen fugacity $f(O_2)$ of the parental magma which is consistent with crystallization of ilmenite in these rocks (Vogel et al. 1999; Meurer and Claeson, 2004; René, 2011). Such trace element and REE patterns are also typical of OIB and within-plate alkaline mafic rocks (Sun and McDonough, 1989; Wittke and Mack, 1993).

4.4. Sr-Nd-Pb isotopes

Whole-rock Sr-Nd-Pb isotopic compositions of representative samples from both suites are shown in Tables 3, 4. The combined Sr-Nd-Pb isotopic plots are shown in Fig. 6a-e, in which the MBPC gabbros are plotted in comparison with mafic magmatism in the modern Turkish-Iranian Plateau (TIP), which is largely derived from lithospheric mantle sources metasomatised during Mesozoic to Cenozoic subduction processes (Neill et al., 2015). Few contemporary analyses exist for the older subduction-related rocks of the region. The analytical methods are in Supplementary Item 2, Section C. Initial values of $(^{87}Sr/^{86}Sr)_i$ and $(^{143}Nd/^{144}Nd)_i$ were calculated for 168 Ma and 40 Ma, respectively for the low-Ti and high-Ti gabbros.

4.4.1. Middle Jurassic low-Ti gabbros

The $(^{87}Sr/^{86}Sr)_i$ of the low-Ti gabbros varies from 0.7035 to 0.70594, and εNd(t) from -6.2 to -0.7. The non-cumulate low-Ti gabbros, with negative Sr anomalies (in Fig. 5a) and higher total REE concentrations (Fig. 6a) show approximately similar whole-rock $(^{87}Sr/^{86}Sr)_i$ values (0.7051–0.70594) to those of cumulate gabbros (except of sample M_{44}, Table 3). In $(^{87}Sr/^{86}Sr)_i$ vs. εNd(t) space (Fig. 6a), all low-Ti gabbros plot within or close to PM (primitive mantle) in the mantle array except M_{44} (olivine gabbro cumulate). The low-Ti gabbros have limited Pb-isotope

variation and are quite clustered in $(^{143}Nd/^{144}Nd)_i$ and $(^{87}Sr/^{86}Sr)_i$ vs. $(^{206}Pb/^{204}Pb)_i$ space (Fig. 6b, c). Likewise these rocks are clustered in $(^{207}Pb/^{204}Pb)_i$ and $(^{208}Pb/^{204}Pb)_i$ vs. $(^{206}Pb/^{204}Pb)_i$ plots above the NHRL (Northern Hemisphere Reference Line; Hart, 1984) (Fig. 6d, e). The cumulate- and non-cumulate gabbros have similar $(^{206}Pb/^{204}Pb)_i$ for a given $(^{207}Pb/^{204}Pb)_i$ and $(^{208}Pb/^{204}Pb)_i$ (Table 4, Fig. 6d, e). The low-Ti gabbros have lower εNd(t)-values but similar $(^{87}Sr/^{86}Sr)_i$ ratios (Fig. 6a) to Upper Jurassic-Lower Cretaceous mafic rocks from the Kapan Arc in Armenia, one of few suites of a similar age to have been analysed recently (Mederer et al., 2013). The low-Ti gabbros also plot close to field of younger (Cenozoic–Quaternary) mafic rocks from the Maha-bad area in the UDMA (Kheirkhah et al., 2013). The gabbros also display similar εNd(t)-values but lower $(^{87}Sr/^{86}Sr)_i$ ratios compared to the Mesozoic gabbro-dioritic dykes, calc-alkaline gran-itoids from the MBPC and the Alvand Batholith (Shahbazi et al., 2010). In $(^{206}Pb/^{204}Pb)_i$ vs. $(^{87}Sr/^{86}Sr)_i$ plots (Fig. 6b-e), the Middle Jurassic gabbros show isotopic correspondence to the BSE (Bulk Silicate Earth) and, perhaps surprisingly, within-plate basaltic samples from E Iran (Kheirkhah et al., 2015).

4.4.2. Late Eocene high-Ti gabbros

The $(^{87}Sr/^{86}Sr)_i$ of the non-cumulate high-Ti gabbros varies from 0.70443 to 0.70635, and εNd(t) values are positive (+1.9 to +2.5, Table 3). The two cumulate gabbroic rocks from this group show higher $(^{87}Sr/^{86}Sr)_i$ and negative to positive εNd(t) (Table 3). The cumulate gabbros lie out-side the mantle array on Figure 7a, but the non-cumulate samples plot within the array, close to the PM value. The high-Ti gabbros have respectively $(^{206}Pb/^{204}Pb)_i$ = 18.35–18.68, $(^{207}Pb/^{204}Pb)_i$ = 15.64–15.67 and $(^{208}Pb/^{204}Pb)_i$ = 38.60–38.82. In $(^{208}Pb/^{204}Pb)_i$ and $(^{207}Pb/^{204}Pb)_i$ vs. $^{206}Pb/^{204}Pb$ space (Fig. 6d), high-Ti gabbros cluster above the NHRL (Table 4, Fig. 6d, e). Com-pared to mafic rocks derived from different mantle sources beneath the modern Turkish–Iranian Plateau (Table 5), two non-cumulate gabbros from this group have similar εNd(t) and $(^{87}Sr/^{86}Sr)_i$ to Cenozoic alkaline mafic rocks from E Iran, Georgia and Armenia (Fig. 6a). In $(^{206}Pb/^{204}Pb)_i$

vs. ($^{87}Sr/^{86}Sr)_i$ plots (Fig. 6b-e), the high-Ti gabbros plot in the areas defined by Cenozoic mafic rocks from E Iran and Quaternary mafic rocks from S Turkey (Table 5). The MBPC gabbros of both ages have relatively similar Pb-isotopic ratios and they cluster in a field defined by Quaternary mafic rocks from S Turkey (Fig. 6d) and cannot be separated based upon their correspondence to any of those individual fields in Pb-Pb isotopic plots.

5. Discussion

5.1. Evaluation of crustal contamination

Mafic magma intruding continental crust can be chemically modified by assimilation of crustal materials (Sandeman et al., 2003; Khalaf et al., 2010). It is essential to evaluate if our samples have undergone crustal contamination before speculating on their mantle sources. High SiO_2 and alkali but low MgO, which are expected in ascending magma after substantial assimilation of crustal materials (e.g., Jahn et al., 1999; Zhang et al., 2002), were not observed in MBPC non-cumulate gabbros. Elsewhere in the Arabia-Eurasia collision zone, crustal contamination has been particularly difficult to identify owing to the chemical similarities between studied samples and the older arc-related crust through which they ascended as magmas (Neill et al., 2013). In the Middle Jurassic gabbros, we found no zircon inheritance and so the only realistic way to identify crustal contamination is through analysis of Sr isotopes and LILE abundances. The assimilation of the crustal materials is expected to increase the $^{87}Sr/^{86}Sr$ ratios as high as 0.711 (observed in Middle Jurassic MBPC granitic rocks, Ahadnejad et al. 2010). In this regard, just three cumulate gabbros do display significant deviation from the other samples on Fig. 6a, so may have experienced assimilation of crustal materials. However, such a conclusion must be countered by the possibility of some mobilization of Sr and other LILE during sub-solidus modification.

Very low ($^{87}Sr/^{86}Sr)_i$ ~ 0.7035 and negative εNd(t) (-6.2) in sample M_{44} of the low-Ti gabbros is characteristic of samples which may have interacted with Rb-depleted continental materials typical of the lower crust (e.g., Wolff et al., 2005; Fowler et al., 2008, Petrone et al., 2010). Howev

er, the low LILE/HFSE and LREE/HREE ratios of M_{44} (Figs. 5b, 6a) indicate only limited lower crustal contamination. This sample will be excluded from further discussion on source region and only the remaining samples will be used.

In the Eocene high-Ti gabbros, there is also no evidence for zircon inheritance Two of the Eocene cumulate gabbros (i.e. samples M_{41} and GU) have high initial $^{87}Sr/^{86}Sr$ (~ 0.7075 and 0.709). Given the lack of typical "crust-like" signatures in these samples (Ti, Nb and Zr depletion, Fig. 5d) and the occurrence of sub-solidus alteration in sample GU (Table 1), some caution should be taken in the interpretation of the high $(^{87}Sr/^{86}Sr)_i$. Thus, these will be excluded from further discussion. Hence, it seems that there is limited evidence for assimilation processes in the evolution of the gabbroic intrusions, particularly during the Middle Jurassic. Firstly, initial $^{87}Sr/^{86}Sr$ ratios do not correlate with SiO_2 content for the high-Ti gabbros and remain constant for the older low-Ti ones (Supplementary Item 1, Fig. 4a). Secondly, initial $^{87}Sr/^{86}Sr$ ratios, over a narrow range of 1/Sr values, remain constant for the low-Ti samples and negatively correlated for high-Ti ones (Supplementary Item 1, Fig. 4b). Finally, Nb/La ratios are relatively constant irrespective of MgO for both groups (Supplementary Item 1, Fig. 4c). Furthermore, any assimilation process coupled with fractional crystallization would result in progressive decreases in compatible element concentrations (such as Cr, Ni, Co) with a concomitant increase in $^{87}Sr/^{86}Sr$ ratios and decrease in $^{143}Nd/^{144}Nd$ ratios. These patterns are not observed in the MBPC gabbros. The rapid upward movement of magma through crustal-scale shear-zone systems with a major transpressional or transtensional component (Ahadnejad et al., 2012; Mohajjel and Fergussen, 2000) could explain insignificant crustal contamination in MBPC gabbros, especially for those of Eocene ages given the likely extensional tectonic setting (Verdel et al., 2011).

5.2. Fractional crystallization

5.2.1. Middle Jurassic low-Ti gabbros

Having discounted the few samples with possible evidence for crustal contamination, we turn to fractional crystallization processes. The derivation of low-MgO, high-alumina rocks by fractional crystallization of high-MgO basaltic magma is typical of magmatic arcs (Bartels et al. 1991, Draper and Johnston 1992). The low-Ti gabbros have high concentrations of compatible elements, concurrent with their derivation from mantle-derived magmas (Table 2). However, they exhibit large changes in MgO (7.92–21.93 wt. %), Ni (12.6–615.4 ppm) and Cr (7.8–1068 ppm) contents (Table 2) over a modest SiO_2 range (43.34–49.87 wt. %) suggesting that they are not primary mantle magmas and have undergone accumulation or fractionation processes consistent with textural evidence. Similar isotopic composition of non-cumulate and cumulate gabbros indicates they were likely derived from common parental magmas. The occurrence of cumulate gabbros with lower REE concen trations than the non-cumulates, positive Eu-anomalies and chondrite-normalized patterns which mirror the non-cumulates (Fig. 6a) is good evidence of crystal fractionation of parent magma en route towards the surface.

However, because of the small data set of non-cumulate samples, the trends observed in Harker-style diagrams are difficult to interpret (Supplementary Item 1, Fig. 6). Nevertheless, the decrease in MgO and (FeO_T) with increasing Zr (ppm) may indicate a role for olivine or clinopyroxene fractionation and decreasing Al_2O_3 with increasing Zr (ppm) indicates plagioclase fractionation. The sequence of olivine, clinopyroxene, hornblende and plagioclase crystallization as well as negative Eu-anomalies (except of sample BR_{18}) in the non-cumulate gabbros is consistent with the known association between high water content of the parent magmas and the suppression of initial plagioclase fractionation to shallow levels (e.g., Richard et al. 2006; Feig et al., 2010). The high water content of the parental magma is further indicated by early crystallization of hornblende relative to plagioclase (both cumulus and primary magmatic types). Such a parent magma with high H_2O content (> 3 wt. %; Tatsumi and Suzuki, 2009) generates a liquid line of descent dominated by olivine and clinopyroxene.

Furthermore, changes in plagioclase An-content (An_{92-37}) of those cumulate samples with tholeiitic affinity (core to rim in Supplementary item 3, Table 2c) indicate changes in the H_2O-pressure during fractional crystallization. This is consistent with variations in An% and FeO concentration observed in plagioclase traverse profiles (Supplementary Item 1, Fig. 7). Decreasing water contents in the magma induce crystallization of sequentially more albitic plagioclase (e.g., Takagi et al. 2005; Hamada and Fujii 2007). The petrography of the MBPC olivine gabbro cumulates indicates that olivine, clinopyroxene and plagioclase are cumulus phases, whereas hornblendes are present as both cumulus and interstitial late crystallizing phases.

5.2.2. Late Eocene high-Ti gabbros

The high-Ti gabbros from the Late Eocene are characterized by moderate to low $Mg^{\#}$ values (0.33–0.46) (Table 2). So, they are unlikely to represent primary mantle melts, corroborated by their wide range of MgO concentrations (4.34–11.47 wt. %), low Ni (12.2–202.6 ppm), Cr (0.5–263.8 ppm) and V (43–243.9 ppm) concentrations (Table 2). Assuming ∑REE gradually increased during ongoing fractional crystallization of parent magma, the positive correlation between ∑REE and SiO_2 content in high-Ti gabbros, indicates that fractional crystallization is an important factor in the evolution of the mafic magmas. Moreover, the approximately parallel REE patterns in high-Ti gabbros reflect evolution through sequential fractionation of common mineral phases from parental magmas along single liquid line of descent.

The increasing Al_2O_3 concentration over a small range of SiO_2 (46.16–48.85 wt. %) also indicates early fractionation of Al_2O_3–poor phases such as olivine and clinopyroxene. Given the delayed fractionation of plagioclase, it seems that these magmas too contained moderate to high H_2O concentrations (>3 wt. %). In addition, the decrease in FeO_T (and MgO) with increasing SiO_2, in line with negative correlations between highly compatible elements (including Cr, Ni and CO) and FeO_T (Supplementary Item 1, Fig. 8) showing an important role of olivine and clinopyroxene fractionation during magmatic evolution of non-cumulate high-Ti gabbros. This liq

uid line of descent is typical for a moderately hydrous magma being characterized by early fractionation of Fe–Mg-rich phases and subsequent low-pressure fractionation amphibole, Fe–Ti-oxides, and An-rich plagioclase. The high Ti concentrations in these rocks indicates differentiation of parental magma at low $f(O_2)$ which excludes early fractionation of Fe-Ti-Oxides.

This sequential crystallization of minerals is also consistent with the presence of cumulus olivine + clinopyroxene + plagioclase and clinopyroxene + plagioclase in Late Eocene olivine gabbro (i.e M_{41}) and cumulus hornblende + clinopyroxene enclosed by hornblende oikocrysts. The crystallization of hornblende oikocrysts from post-cumulus trapped melt supports the presence of a hydrous parental magma for the Late Eocene olivine gabbro cumulate. The high water concentrations are not unusual in rocks displaying within-plate character: such rocks are found in non-subduction settings and particularly where small volume melting takes place, given that water can be treated as an incompatible component (Bai and Kohlstedt, 1992; Braun et al., 2000).

5.3. Petrogenesis

5.3.1. Middle Jurassic low-Ti gabbros

5.3.1.1. Nature of the mantle source

High concentrations of compatible elements (i.e. V, Cr and Ni) in non-cumulate low-Ti gabbros are consistent with derivation from the mantle (e.g., Perfit et al., 1980). These rocks are characterized by enrichment in LILE and depletion of HFSE with all the distinctive features of arc-type magmatism derived from a subduction-modified mantle source. Since the zircons separated from low-Ti gabbros non-cumulate gabbros show no evidence of inheritance from continental basement or wall rocks, their negative Nb–Ta anomalies are related to subduction zone processes rather than continental contamination. Nb, Ta, Zr and Yb are immobile elements in slab-derived aqueous fluids (Pearce and Peate, 1995; Eiler et al., 2007) so can normally be used to indicate the mantle source composition prior to enrichment. However, the non-cumulate low-Ti gabbros display lower Nb/Ta ratios than that of primitive mantle source (PM-1 and PM-2, Fig. 8a), but giv

en low Zr/Nb ratios, a depleted mantle origin for them is unlikely. It appears that they were originated from a PM-like source that had not previously been significantly depleted by melting event(s). Moreover, the La/Yb and Zr/Ta vs. Zr/Nb diagrams (Fig. 7b, c) indicate enriched mantle components were involved in the petrogenesis of these rocks.

Ignoring the single low-$^{87}Sr/^{86}Sr$ outlier, the low-Ti gabbros have consistent isotopic compositions which lie below Bulk Earth (BSE) in the mantle array (Fig.7a). The isotopically enriched Sr-Nd-Pb signatures imply partial melting of metasomatised mantle wedge peridotite, or of subcontinental lithospheric mantle (SCLM). These two possible sources are difficult to distinguish from one another, but given consistent geological evidence for Tethyan subduction on the Eurasian margin throughout the Mesozoic and Paleogene (Koop et al., 1982; Dilek and Sandvol, 2009 Agard et al., 2011; Verdel et al., 2011; Chiu et al., 2013), it is likely that mantle wedge melting was a major contributor to magmagenesis. Among those mafic rocks from the Arabia-Eurasia collision zone plotted in Fig.7, the low-Ti gabbros from the MBPC correspond to those of with a subduction-related metasomatised mantle source (listed and described in Table 5). These comparisons (Fig.7a-e, Table 5) agree with the trace element and isotopic signatures of an enriched mantle source for the Middle Jurassic gabbros.

5.3.1.2. Nature of the subducted component

Owing to negligible Ta mobility in slab-derived aqueous fluid, the addition of such fluids will increase the Th/Yb ratio at approximately constant Ta/Yb in arc magmas (Pearce et al., 1995). Therefore, according to the Th/Yb vs. Ta/Yb plot (Fig. 8d), mantle wedge peridotite was likely to have been metasomatised by slab-derived aqueous fluid (e.g., Sun and McDonough, 1989), comparable to those Mesozoic mafic rocks from Kapan arc (Armenia: Mederer et al., 2013). Highly variable Ba/Rb ratios (1.9–19.44) and near-constant low Nb/La (0.12–0.46) ratios in Middle Jurassic low-Ti gabbros also imply metasomatism in the source region by slab-derived components (Supplementary Item 1, Fig. 5a). Most of the samples fall above and close to the line

475 Pb/Th = 1 in the Nd-normalized Th vs. Pb plot (Supplementary Item 1, Fig. 5b) which, consider-
476 ing the higher solubility of Th in silicate melts versus Pb in hydrous fluids (Gómez-Tuena et al.,
477 2003), reflects a more significant role for subducted sediment-related fluids relative to sediment
478 melts. High Sr/Nd ratios (7.14–128.3, Table 2) and moderately high LILE/HFSE ratios together
479 with radiogenic εNd(t) values in these rocks corroborate the addition of slab-derived fluids to the
480 mantle wedge (e.g., Davidson, 1987; Elliott et al., 1997; Kepezhinskas et al., 1997).

481 5.3.1.3. Mineralogy of the mantle source

482 In the absence of mantle xenoliths, whole-rock geochemistry can provide some constraints on
483 mantle source mineralogy. The moderately steep REE-patterns (chondrite-normalized La/Yb ra-
484 tios: (La/Yb_{cn})= 3.05–7.45, Table 2) and HREE depletion (Yb <4) may indicate the presence of
485 garnet in the melt residue (Fig.6a). Because of different phase/melt partition coefficients of Yb
486 and Gd for garnet and spinel (McKenzie and O'Nions, 1991), a mantle source with residual spi-
487 nel will produce $(Gd/Yb)_{cn}$ ratios ~ 1.2, whereas those melts originated from garnet-bearing
488 source are expected to have higher values (Allen et al., 2013; Kelemen et al., 2003). Therefore,
489 the $(Gd/Yb)_{cn}$ ratios ranging from 1.62 to 3 in the non-cumulate gabbros indicate moderate frac-
490 tionation between MREE and HREE and probable derivation from the garnet-spinel transition
491 zone. $(Dy/Yb)_{cn}$ ratios of non-cumulate gabbros (1.67−2.58) are also between values suggested
492 for spinel-bearing mantle sources (< 1.5) and garnet-bearing sources (> 2.5) (e.g., Chang et al.,
493 2009; Jiang et al., 2010). The presence of residual amphibole is consistent with high Nb/Ta ratios
494 in these rocks (e.g., Foley et al., 2002; Hofmann et al., 2011), particularly the non-cumulate gab-
495 bros.

496 5.3.1.4. Melting and fractional crystallization model

497 To constrain the formation conditions of the MBPC mafic magma, non-modal batch melting
498 models were considered for two different possible mantle sources: 1) metasomatized amphibole-
499 bearing lherzolite from the garnet-spinel transition zone; 2) garnet-free spinel lherzolite. The

500 numerical models favor the former as potential mantle source, because it generates residual melts
501 with REE concentrations (Supplementary Item 3, Table 3 and 5; Fig. 9a) and chondrite-
502 normalized La/Yb ratios consistent with those of the low-Ti gabbros, considering that only minor
503 changes to these ratios will occur during subsequent fractional crystallization processes. Models
504 show the mantle source region for the low-Ti gabbros was most likely a metasomatised amphi-
505 bole-bearing lherzolite (up to 2% Amp) from the garnet-spinel transition zone with up to 7 vol.%
506 garnet, and up to 3 vol.% spinel (Supplementary Item 3, Table 3). The result is shown as a melt-
507 ing trajectory ($f_{melting}$= 0.15) on a chondrite normalized REE plot (Fig. 8a) and on a primitive
508 mantle-normalized trace element plot (Fig. 9b). The low TiO_2 content in these rocks is consistent
509 with relatively high degree melting in the source region, however this is also likely to be due to
510 retention of Ti in rutile in the subducting slab, and Ti-depletion in the calc-alkaline parent mag-
511 ma as a consequence of high oxidation early differentiation of Fe-Ti oxides (e.g., Snyder et al.
512 1993; Frost et al. 1988; Vogel et al. 1999). The lower REE concentrations in melt generated by
513 partial fusion (15%) of the chosen mantle source relative to the non-cumulate low-Ti gabbros
514 does indicate some modification of the parental magmas occurred, consistent with the above dis-
515 cussion on FC (Fig. 9a). To quantify the effect of fractional crystallization, the separation of the
516 mineral assemblage comprising 0.2 Ol + 0.05 Cpx + 0.45 Pl + 0.3 Amp ± 0.005 Ap (mineral ab-
517 breviations are from Whitney and Evans, 2010) — equivalent to the modal composition of sam-
518 ple BR_{Q2} — from the primary magma has been modeled (Fig. 9a, b; results and parameters in
519 Supplementary Item 3, Tables 3, 4, 5). Based on this model, the trace element concentrations of
520 the non-cumulate gabbros are close to a hypothetical melt produced by 35% fractionation of cu-
521 mulate gabbros (i.e. BR_{Q2}) from a mantle-derived parental magma. The presence of hematite
522 (probably in equilibrium with magnetite)alongside negative Eu-anomalies in the non-cumulate
523 gabbros (save for BR_{18}) supports a high oxidation state of the parent magma at emplacement lev-
524 el. However, the existence of ilmenite, lack of magnetite or hematite and the presence of positive

Eu-anomalies in the Middle Jurassic cumulate gabbros are favored by low $f(O_2)$ (Synder et al., 1993; Namur et al., 2010). Therefore, the system may have experienced an increase in $f(O_2)$ after separation of cumulus phases, probably either by extraction of FeO due to ilmenite fractionation (Snyder et al. 1993).

5.3.2.Late Eocene high-Ti gabbros

5.3.2.1. Nature of the mantle source

There are several lines of evidence unsupportive of a subduction-modified mantle source as the major contributor to the Late Eocene mafic magmatism. Lower K/Nb (66–486) and Rb/Nb (0.35–1.99) ratios than those of subduction-related Middle Jurassic gabbros, no depletion of HFSE (e.g., Nb–Ta and Ti) (OIB-like), only minor enrichment of LILE relative to HFSE, and no significant Eu anomalies (Fig. 6b), indicate an origin as within-plate type rocks originating either from the convecting asthenosphere (Hofmann, 1988; Sun and McDonough, 1989; Wittke and Mack, 1993; Allen et al., 2013), or an enriched upper mantle source (e.g., Hastie et al., 2011).

Non-cumulate high-Ti gabbros have higher Nb/Ta ratios than Zr/Nb and plot close to the OIB field in Fig.8a. Likewise, the low Zr/Nb (OIB < 10; Pearce and Norry, 1979), moderate La/Yb (Fig.8b) and low Zr/Ta ratios (Fig.8c) indicate that they were originated from an enriched mantle source. The high Zr/Y (4.55-7.26) and Nb/Y (0.69-1.81) in this group also suggest their origin from an enriched mantle source. As documented in Fig.8b, the mantle source for high-Ti gabbros was more enriched than E-MORB and WAM-like sources (Western Anatolian Mantle, Aldanmaz et al., 2000). These rocks also plot in the OIB field in the Th/Yb vs. Ta/Yb diagram of Pearce (1983) (Fig.8d), close to fields defined by Early Cenozoic tholeiitic dykes from the MBPC (area 3 in Fig.8d; Deevsalar, 2015) and Late Cenozoic mafic alkaline rocks from East Iran (area 4 in Fig.8d; Kheirkhah et al., 2015). There is no elemental or isotopic evidence for addition of subducted sediment-derived melt or fluid during magma genesis. The relatively small volume of Late Eocene exposed mafic intrusive rocks can be interpreted to reflect that they were

originated from small-moderate melting degrees of enriched upper mantle asthenosphere (e.g., Ramos and Key, 1992; Gorring et al., 1997) rather than a fertile lower mantle-derived plume (e.g., Cheadle and Petford, 1993; Marquez et al., 1999) or depleted asthenosphere.

5.3.2.2. Mineralogy of the mantle source

The relatively depleted HREE in non-cumulate high-Ti gabbros ($(Gd/Yb)_{cn}$: 2.1–2.44, $(Dy/Yb)_{cn}$: 2.12–2.67, and $(Tb/Yb)_{cn}$: 1.75–2.12), indicates that garnet was probably a residual phase in the mantle source. Given the $(Dy/Yb)_{cn}$ ratios of (2.19–2.67) in the non-cumulate gabbros, both garnet and spinel may again have been present in the mantle melting residue (e.g., Chang et al., 2009; Jiang et al., 210).$(Sm/Yb)_{cn}$ ratios (2.45–3.57) are slightly higher than average values suggested for spinel lherzolite (McDonough, 1990) and little varying $(La/Sm)_{cn}$ ratios (2.61–3.26) can be explained either by melting of a mantle source with both garnet and spinel mineralogy (garnet–spinel transition zone) or mixing between melts originated from garnet-bearing peridotite (deep mantle) and spinel-bearing peridotite (shallower depth). As the source for Late Eocene mafic magmatism within the MBPC, asthenosphere upwelling is consistent with the second model that require a drastic change in depth of partial melting.

5.3.2.3. Melting, mixing and fractional crystallization model

Depletion in isotopic ratios relative to BSE (Fig. 6a) and enriched OIB-like trace element composition in non-cumulate high-Ti gabbros suggest that the enrichment of the magma is a recent event and not a long-term source characteristic.

Two alternative scenarios invoke the addition of incompatible element-enriched fluid and/or melt advancing ahead of the uprising plume or the incorporation of enriched conductive convective mantle to incompatible element-depleted mantle source (e.g., Lassiter et al., 2000; Lundstrom et al., 2003). Fig. 10a shows that the non-cumulate high-Ti gabbros have La concentrations and La/Sm ratios greater than those of DMM, PM- and WAM-like mantle sources, indicating they could be generated by small-moderate degree melting of a mantle source with slightly more en

575 riched character than these sources. The classic, non-modal batch melting model is shown as tra-
576 jectories on Fig. 10a (melting equation of Shaw, 1970). The trace element modeling indicates
577 low degree melting (non-modal batch melting model, $f_{melting}$ = 0.05) of a garnet-spinel lherzolite
578 (garnet ~ 6 vol%, spinel ~ 2 vol%), probably followed by relatively high degree melting ($f_{melting}$
579 = 0.15) at shallower depth (garnet ~ 4.5 vol%, spinel ~ 2 vol%) but still within the garnet-spinel
580 transition zone (Fig. 10b; results and the parameters used for trace element modeling are in Sup-
581 plementary Item 3, Tables 3, 4 and 6).
582 Alkaline affinity in mantle-derived basaltic rocks is most consistent with low-degree melting of
583 lherzolitic mantle in the garnet stability field as frequently documented in the literature (e.g.,
584 Green and Ringwood, 1967; Jaques and Green, 1980; Hirose and Kushiro, 1993; DePaolo and
585 Daley, 2000; Macpherson et al., 2010). The high TiO_2, Zr and Nb content in these rocks is also
586 consistent with low degree melting in the source region. Higher degree melting (~ 15%) at a
587 shallower depth generates primary tholeiitic magma (Green and Ringwood, 1967; Jaques and
588 Green, 1980; Hirose and Kushiro, 1993; DePaolo and Daley, 2000). The trace element modeling
589 indicates that a hybrid melt — shown as a trajectory on the Figure 10b (f_{mixing}= 0.6) — could be
590 considered as a parental magma for the Late Eocene high-Ti gabbros.
591 The modelling results for fractional crystallization ($f_{crystallization}$= 0.05) of an assemblage compris-
592 ing 20% Ol + 40% Cpx + 30% Amp + 10% Pl from an assumed parent magma are shown in
593 comparison with high-Ti non-cumulate gabbros (Fig. 10b; Supplementary item 3, Table 6). The
594 existence of ilmenite together with positive Eu-anomaly in cumulate gabbros indicate low $f(O_2)$
595 for the parent magma whereas, lacking positive Eu-anomaly and ilmenite in the presence of
596 hematite suggest high $f(O_2)$ for non-cumulate gabbros.

597 **5.4. Contemporaneous melting of mantle and crustal sources**

598 The Middle Jurassic arc-like mafic magmatism in the SaSZ is coeval with widespread granitic
599 magmatism (Ahmadi-Khalaji et al., 2007; Ahadnejad et al., 2010; Shahbazi et al., 2010;

Mahmoudi et al. 2011, Agard et al., 2011, Sepahi et al., 2014). Recent studies on the MBPC granitoids demonstrate that they are products of crustal melting (e.g., Deevsalar 2009, Ahadnejad et al., 2010, Ahmadi-Khalaji et al., 2007). Middle Jurassic granitic rocks have much more radiogenic $^{87}Sr/^{86}Sr$, but similar εNd(t) ($(^{87}Sr/^{86}Sr)_i$ = 0.70798–0.71087 and εNd(t)= -1–-5; Ahadnejad et al., 2010) to contemporaneous gabbroic intrusions.

The Middle Jurassic mafic magmatism in MBPC provides clear evidence of an active subduction system located in in the southwestern margin of the Iranian portion of the Eurasian plate. Melting of mantle peridotite in the garnet-amphibole stability field (60–100 km; Robinson and Wood, 1998; McBride and Gilmour, 2003), may indicate a significant thickness of Eurasian crust above the subduction zone. The model that we favour for combined mafic and felsic magmatism is that of hydrous basaltic magma ascending to the bottom of continental lithosphere and triggering melting of lower crust. Lower crustal melting driven either by heat supply from uprising basaltic magma (e.g., Petford and Gallagher, 2001) or through heat transfer and fluid fluxing from underplated crystallizing basalts seems an appropriate model for extensive granitic magmatism of Middle Jurassic age in the MBPC. This finding is consistent with field evidence of I-type metaluminous and mafic microgranular enclaves (MMEs) as well as peraluminous S-type granites, micaceous enclaves and metapelitic xenoliths in MBPC granitoids, which collectively indicate both crustal melting and interaction between mafic and felsic magmas (e.g., Deevsalar 2009, Ahadnejad et al., 2010, Ahmadi-Khalaji et al., 2007). Because of their low viscosity, some rapidly ascending hydrous mantle-derived magmas clearly did not undergo substantial enough differentiation to generate intermediate magma compositions, nor were they affected by significant assimilation of crustal materials. Except for some the MMEs, there is no clear petrogenetic association between gabbroic intrusive rocks and granitoids from the MBPC (Deevsalar 2009, Deevsalar et al., 2010, 2012). They do not show similarity in terms of major, trace and isotopic signatures either, so it is unlikely that the granitoids are evolved equivalents of the mafic rocks

from this study (data for the MBPC granitoids are from Deevsalar 2009; Ahmadi-Khalaji et al., 2007; Ahadnejad et al., 2010). However, the small volume of mafic plutons in the SaSZ, presumably representing small batches of mafic melts which could ascend through the SaSZ crust, may not fully represent the extent of mafic magmatism, as large volumes of mafic magma could be trapped and partly crystallized (underplated) at the crust-mantle boundary (e.g., Xu et al., 2004; Annen et al., 2006), or deeper in the crust, and would be responsible for large scale crustal melting and extensive felsic plutonism in the MBPC during the Middle Jurassic. Moreover, the large-scale melting in the deep crust generates a barrier of more viscous, less dense and colder felsic melts which would impede the further ascent of mafic magma. Since the granitoid bodies were fully locked up by the time the mafic magmas arrived (evidenced by the MMEs), the easiest route towards the surface was likely to have been through the still-hot granitoids. The lack of Late Eocene felsic magmatism in the MBPC indicates a lower thermal flux and limited crustal anatexis during the Cenozoic.

6. Geodynamic model of magmatic evolution in N-SaSZ

Changing sources and conditions of magma generation between the Middle Jurassic and Late Eocene clearly indicate changing geodynamic settings. Given the long-lasting history of Tethyan subduction in this region (~ 150 Ma of Andean-like arc magmatism, Mouthereau et al., 2012), changes in rate, angle and depth of the subduction will have been important in controlling the location and chemistry of magmatic activity. The Middle Jurassic consumption of a NE–dipping Neo-Tethyan oceanic lithosphere, mantle-wedge peridotite melting and crustal recycling led to contemporaneous felsic and minor mafic magmatic events throughout the N-SaSZ. From the Late Jurassic to the Early Eocene, magmatic activities in the SaSZ were limited to its northwesternmost region (Nogole Sadat and Houshmandzadeh, 1993; Azizi and Jahanrigi, 2009; Mazhari et al., 2009). The general lack of Late Jurassic–Paleocene igneous rocks in large parts of the N-SaSZ, including the MBPC, Hamadan and Ghorveh regions and further south in Aligudarz (e.g.

Mohajjel et al., 2014) has been taken to indicate a long period of low-angle subduction, which would serve to shut down magmatic activity in the SaSZ and explain an inboard retreat of magmatic activity to northern Iran during the Cretaceous (e.g., Guest et al., 2006; Verdel et al., 2011). Late Cretaceous magmatic activity in northwest Iran (N-SaSZ) along with northern Iran (alkaline and tholeiitic rocks in the western Alborz zone, Salavati, 2008) do seem to indicate that the Neo-Tethys slab locally descended at steeper angle relative to elsewhere in the N-SaSZ following Early-Middle Cretaceous slab flattening (cf. the segmented Laramide slab of Saleeby, 2003). Therefore, the Neo-Tethys plate of SaSZ at Late Cretaceous was probably segmented into components of differing dip, some of which subducted sub-orizontally (Ghorveh–Aligudarz segment) and others at a much steeper angle (Sanandaj and N Iran).

However, a Late Paleocene to Late Eocene phase of extension and an increase in magmatism across much of Iran has been ascribed to pre-collision roll-back and retreat of the Tethyan slab (Verdel et al., 2011; Ballato et al., 2011; Morley et al., 2009; Verdel et al., 2007; Vincent et al., 2005). The intraplate mafic magmatism in the MBPC indicates that the subduction-related magmatism in the Ghorveh-Aliqudarz segment of the Eurasian margin was replaced by asthenospheric melting in the Late Eocene.

Since published models demonstrate the probable onset of continental collision between Arabia and Eurasia at or shortly after the Eocene-Oligocene transition (e.g., McQuarrie and van Hinsbergen, 2013; Allen and Armstrong, 2008), the Late Eocene gabbros therefore formed shortly before the onset of terminal collision. However, the model of Verdel et al. (2011) does not argue for extensive asthenospheric melting until the Early Oligocene to Miocene times, when the Tethyan slab had rolled back sufficiently to allow for widespread asthenospheric upwelling. Hence the role of asthenospheric mantle in the generation of MBPC Late Eocene gabbros as documented in this work requires some modification to the hypothesis of Verdel et al. (2011). The SaSZ lies furthest west and southwest of all Iranian loci of arc magmatism, and as such

675 would have been the last to experience the roll-back of the Tethyan slab and subsequent mantle
676 upwelling. Either slab roll-back was quicker than modelled by Verdel et al. (2011), or a process
677 such as ridge subduction, slab tearing or slab break-off managed to rapidly remove much of the
678 Tethyan slab from beneath the SaSZ. We have no further data with which to speculate the extent
679 of ridge subduction, tearing or lithospheric removal, but highlight the importance of accounting
680 for all occurrences of mafic, mantle-derived magmatic activity in collisional tectonic regimes in
681 order to build the most consistent geodynamic model.
682 We consider a reduction in the rollback velocity and subsequent segmentation of the subducting
683 slab (Sacks and Secor, 1990; Govers and Wortel, 2005, Rosenbaum et al., 2008) to be a good
684 explanation for the Late Eocene within-plate-style magmatism of the SaSZ. This scenario is also
685 consistent with the model for a slab break-off event below the SaSZ proposed by Agard et al.
686 (2011) as an explanation for Paleocene–Eocene magmatism in Kermanshah.

687 ## 7. Conclusions

688 We have identified two distinct phases of mafic plutonism in the Malayer-Boroujerd Plutonic
689 Complex. The first occurred in the Middle Jurassic (ca. 168 Ma) with low-Ti calc-alkaline to
690 transitional tholeiitic affinity, the second in the Late Eocene (ca. 40 Ma) with high-Ti alkaline
691 affinity.
692 Data suggest that mafic magma generation beneath the MBPC may have occurred in at least two
693 stages depending on the rate and style of Neo-Tethys subduction beneath CIMC:
694 1) Subduction stage:
695 The parental magmas for the high-Ti gabbros were generated during active subduction of Neo-
696 Tethys beneath Ghorveh-Aliqudarz arc in the Middle Jurassic, by (modelled) ~15% partial melt-
697 ing of a metasomatised lherzolitic mantle source within the garnet-spinel transition zone. High-
698 Ti gabbros comprise both cumulate and non-cumulate samples with shared geochemical and
699 isotopic affinities indicating derivation from a common basaltic parental magma. REE and trace

element modeling indicate the non-cumulate and cumulate gabbros are respectively produced by fractional crystallization and crystal accumulation of olivine, clinopyroxene, plagioclase, amphibole ± apatite and ilmenite from the parent. The fractional crystallization of mantle-derived magmas was concurrent with assimilation of crustal material affecting only a few of our analysed samples. However, more widely in the SaSZ, the addition of mafic magma to the crust was a likely trigger for more extensive contemporaneous felsic magmatism.

2) Pre- to syn-collision stage:

The Cretaceous–Paleocene was a period of relative quiescence in the N-SaSZ (except for the far NW-SaSZ) and the flux of slab-derived components to the mantle was probably reduced due to flat-slab subduction. Late Eocene slab-rollback following this period of atypical subduction could have led to slab lateral tearing and melting of uprising asthenosphere. The MBPC high-Ti gabbros were largely derived from asthenospheric magma through low degree melting of lherzolite within the garnet-spinel transition zone, followed by higher degrees of melting at a shallower depth. The magmas ascended, underwent fractional crystallization again experienced only limited crustal interaction. This model represents an addition to the model of Verdel et al. (2011), in pointing out the presence of Eocene asthenospheric melting far to the west of presently-acknowledged loci of magmatic activity at that time. This finding necessitates revision to Verdel et al.'s model, perhaps by addition of a component of slab tearing beneath the sites of Eocene mafic magmatism within the SaSZ.

Acknowledgements

The current research was funded by a Tarbiat Modares University research grant and also through financial support from the Ministry of Science, Research and Technology of Iran during sabbatical leave of the senior author at the University of the Ryukyus, Japan. Major parts of the elemental and all isotopic analyses were carried out at the University of the Ryukyus. The University of Naruto is thanked for facilitating microprobe access and performing XRF analyses.

725 Zircon U-Pb dating was undertaken at Institute of Earth Sciences (IES), Academia Sinica, Taipei
726 funded by a Grant-in-Aid for Scientific Research (C) 25400519 to RS. Thanks are due in par-
727 ticular to Mr Chinen and Mr Hamada for technical assistance.

References

Ahadnejad, V., Valizadeh, M. V., Deevsalar, R., Rezaei-Kahkhaei, M., 2010. Age and geotectonic position of the Malayer granitoids: Implication for plutonism in the Sanandaj-Sirjan Zone, W Iran. Neues Jahrbuch Fur Geologie Und Palaontologie-Abhandlungen 261, 61–75.

Ahadnejad, V., Valizadeh M. V., Deevsalar, R., Rasouli, J. 2012. The field and microstructural study of Malayer Plutonic Rocks (MPR), West Iran. Geopersia 1, 1, 59-71.

Ahmadi-Khalaji, A., Esmaeily, D., Valizadeh, M. V., Rahimpour-Bonab, H., 2007. Petrology and geochemistry of the granitoid complex of Boroujerd, Sanandaj-Sirjan Zone, western Iran. Journal of Asian Earth Sciences 29, 859–877.

Agard, P., Omrani, J., Jolivet, L., Mouthereau, F., 2005. Convergence history across Zagros (Iran): constraints from collisional and earlier deformation. International Journal of Earth Sciences 94, 401–419.

Agard, P., Omrani, J., Jolviet, L., Whitechurch, H., Vrielynck, B., Spakman, W., Monie, P., Meyer, B., Wortel, R., 2011. Zagros orogeny: a subduction-dominated process. Geological Magazine 148 (5-6), 692–725.

Aldanmaz, E., Pearce, J.A., Thirlwall, M.F., Mitchell, J.G., 2000. Petrogenetic evolution of Late Cenozoic, post-collision volcanism in western Anatolia, Turkey. Journal of Volcanology and Geothermal Research 102, 67–95.

Aldanmaz, E., Köprübas¸ N., Gürer, ö.F., Kaymakc, N., Gourgaud, A., 2006. Geochemical constraints on the Cenozoic, OIB-type alkaline volcanic rocks of NW Turkey: Implications for mantle sources and melting processes. Lithos 86, 50–76.

Altunkaynak, S., Dilek, Y., 2013. Eocene mafic volcanism in northern Anatolia: its causes and mantle sources in the absence of active subduction. International Geology Review, http://dx.doi.org/10.1080/00206814.2013.792497.

752 Allen, M. B., Armstrong, H. A., 2008. Arabia-Eurasia collision and the forcing of mid-Cenozoic
753 global cooling. Palaegeography, Palaeoclimatology, Palaeoecology 265, 52-58.
754 Allen, M. B., Kheirkhah, M., Neill, I., Emami, M., McLeod, C. L., 2013. Generation of arc and
755 within-plate chemical signatures in collision zone magmatism: Quaternary lavas from Kurdistan
756 province, Iran. Journal of Petrology 54, 887–911.
757 Annen, C., Blundy, J. D., Sparks, R. S. J., 2006. The genesis of intermediate and silicic magmas
758 in deep crustal hot zones. Journal of Petrology 47, 505–539.
759 Azizi, H., Jahangiri, A., 2008. Cretaceous subduction-related volcanism in the northern Sanandaj-
760 Sirjan Zone, Iran. Journal of Geodynamics 45, 178–190.
761 Azizi, H., Asahara, Y., 2013. Juvenile granite in the Sanandaj–Sirjan Zone, NW Iran: Late Juras-
762 sic–Early Cretaceous arc–continent collision. International Geology Review 55, 12, 1523–1540.
763 Azizi, H., Zanjefili Beiranvand, M., Asahara, Y., 2014. Zircon U–Pb ages and petrogenesis of a
764 tonalite–trondhjemite–granodiorite (TTG) complex in the northern Sanandaj–Sirjan Zone, northwest
765 Iran: Evidence for Late Jurassic arc–continent collision. Lithos, doi: 10.1016/j. lithos.2014.11.012.
766 Azizi, H., Najari, M., Asahara, Y., Catlos, E.J., Shimizu, M., Yamamoto, K., 2015. U-Pb zircon
767 ages and geochemistry of Kangareh and Taghiabad mafic bodies in northern Sanandaj–Sirjan Zone,
768 Iran: Evidence for intra-oceanic arc and back-arc tectonic regime in Late Jurassic. Tectonophysics,
769 doi:10.1016/j.tecto.2015.08.008.
770 Bai, Q., Kohlstedt, D. L., 1992. High-temperature creep of olivine single crystals. 2. Dislocation
771 structures. Tectonophysics 206, 1-29.
772 Ballato, P., Uba, C. E., Landgraf, A.,Strecker, M. R., Sudo, M., Stockli, D., Friedrich, A., Tabat-
773 abaei, S. H., 2011. Arabia–Eurasia continental collision: insights from late Tertiary foreland basin
774 evolution in the Alborz Mountains, northern Iran. Geological Society of America Bulletin 123 (1/2),
775 106–131.

776 Bartels, K. S., Kinzler, R.J., Grove, T.L., 1991. High pressure phase relations of primitive high-
777 alumina basalts from Medicine Lake volcano, northern California. Contributions to Mineralogy and
778 Petrology 108, 253–270.
779 Braun, C., Hardy, D. R., Bradley, R. S., 2000. Hydrological and Meteorological Observations at
780 Lake Tuborg, Ellesmere Island, Nunavut, Canada. Polar Geography 24, 2, 83-97.
781 Cheadle, M. J., Petford, M., 1993. The origin of southern Patagonian plateau basalts (abstract).
782 EOS Transactions, American Geophysical Union 74-43, 663.
783 Chiu, H. Y., Chung, S. L., Zarrinkoub, M. H., Mohammadi, S., Khatib, M. M., Iizuka Y., 2013.
784 Zircon U–Pb age constraints from Iran on the magmatic evolution related to Neotethyan subduction
785 and Zagros orogeny. Lithos 162–163, 70–87.
786 Claeson, D. T., Meurer, W. P., 2004. Fractional crystallization of hydrous basaltic ‘‘arc-type’’
787 magmas and the formation of amphibole-bearing gabbroic cumulates. Contribution Mineralogy and
788 Petrology 147: 288–304.
789 Cousens, B. L., Allan, J. F., 1992. Pb, Sr, and isotopic study of basaltic rocks from Sea of Japan,
790 legs 127/1281. Proceedings of the Ocean Drilling Program, Scientific Results 127-128, Pt. 2.
791 Davidson, J. P., 1987. Crustal contamination versus subduction zone enrichment: examples from
792 the Lesser Antilles and implications for mantle source compositions of island arc volcanic rocks.
793 Geochimica et Cosmochimica Acta 51, 2185–2198.
794 Davidson, J.P., 1996. Deciphering mantle and crustal signature in subduction zone magmatism.
795 In: Bebout, G. E., Scholl, D. W., Kirby, S. H., Platt, J.P. (Eds.), Subduction: Top to Bottom. Ameri-
796 can Geophysical Union, Washington DC, pp. 251–262.
797 Deevsalar, R., 2009. Petrology and geochemistry of the granitoids from Malayer plutonic com-
798 plex and their magmatic enclaves and meta-pelittic xenoliths (Western Iran). Unpublished MSc the-
799 sis, Tehran University, Iran.

800 Deevsalar, R., Valizadeh, M.V., 2010. The using of field and microstructural evidences in deter-
801 mination of the origin of magmatic enclaves and metapelitic Xenoliths in Malayer plutonic complex
802 (West IRAN). Scientific Quarterly Journal Geosciences 19, 76, 9- 16.
803 Deevsalar, R., Valizadeh, M.V., Ahadnejad, V., 2012. The determining of the nature of magmatic
804 encalves in granites of Malayer plutonic complex based on geochemical and statistical methods.
805 Scientific Quarterly Journal Geosciences 21, 83, 129-140.
806 Deevsalar, R., Ghorbani, M. R., Ghaderi, M., Ahmadian, J., Murata, M., Ozawa, H., Shinjo, R.,
807 2014. Geochemistry and petrogenesis of arc-related to intraplate mafic magmatism from the Malay-
808 er-Boroujerd plutonic complex, northern Sanandaj-Sirjan magmatic zone, Iran. Neues Jahrbuch für
809 Geology and Paläontology Abh. 274/1, 81–120.
810 Deevsalar, R., 2015. Petrology, geochemistry and tectonomagmatic evolution of mafic-
811 intermediate rocks from the Malayer-Boroujerd plutonic complex, northern Sanandaj-Sirjan mag-
812 matic zone, Iran. PhD Thesis, Tarbiat Modares University (TMU), Iran.
813 DePaolo, D. J., 1981. Neodymium isotopes in the Colorado Front range and crust–mantle evolu-
814 tion in the Proterozoic. Nature 291, 193–196.
815 DePaolo, D. J., Daley, E. E., 2000. Neodymium isotopes in basalts of the Southwest Basin and
816 Range and lithospheric thinning during continental extension. Chemical Geology, 169, 157–185.
817 Dilek, Y., Sandvol, E., 2009. Seismic structure, crustal architecture and tectonic evolution of the
818 Anatolian–African Plate Boundary and the Cenozoic Orogenic Belts in the Eastern Mediterranean
819 Region. In: Murphy, J.B., Keppie, J.D., Hynes, A.J. (Eds.), Ancient Orogens and Modern Ana-
820 logues. Geological Society, London: Special Publications, vol. 327, pp. 127–160.
821 Draper, D. S., Johnston, A. D., 1992. Anhydrous PT phase relations of an Aleutian high-MgO
822 basalt: an investigation of the role of olivine-liquid reaction in the generation of arc high-alumina
823 basalts. Contributions to Mineralogy and Petrology 112, 501–519.

824 Ekici, T., Macpherson, C.G., Otlu, N., Fontignie, D., 2014. Foreland magmatism during the Ara-
825 bia–Eurasia collision: Pliocene–Quaternary activity of the Karacadag Volcanic Complex, SW Tur-
826 key. Journal of Petrology 55, 1753–1777.
827 Elliott, T., Plank, T., Zindler, A., White, W., Bourdon, B., 1997. Element transport from slab to
828 volcanic front at the Mariana arc. Journal of Geophysical Research 102, 14991-15019.
829 Eiler, J.M., Schiano, P., Valley, J.W., Kita, N.T., Stolper, E.M., 2007. Oxygen-isotope and trace
830 element constraints on the origins of silica-rich melts in the subarc mantle. Geochemistry, Geophys-
831 ics, Geosystems 8, Q09012.
832 Esna-Ashari, A., Tiepolo, M., Valizadeh, M. V., Hassanzadeh, J., Sepahi, A. A., 2012. Geochem-
833 istry and zircon U-Pb geochronology of Aligoodarz granitoid complex, Sanandaj-Sirjan zone, Iran.
834 Journal of Asian Earth Sciences 43, 11–22.
835 Feig, S. T., Koepke, J., Snow, J. E., 2010. Effect of oxygen fugacity and water on phase equilib-
836 ria of a hydrous tholeiitic basalt. Contributions to Mineralogy and Petorlogy 160, 551-568.
837 Foley, S.F., Tiepolo, M., Vannucci, R., 2002. Growth of early continental crust controlled by
838 melting of amphibolite in subduction zones. Nature 417, 837–840.
839 Fowler, M. B., Kocks, H., Darbyshire, D. P. F., Greenwood, P. B., 2008. Petrogenesis of high Ba-
840 Sr plutons from the Northern Highland Terrane of the British Caledonian Province. Lithos 105, 129-
841 148.
842 Frost., B. R., Lindsley., D. H., Andersen, D. J., 1988. Fe-Ti oxide-silicate equilibria: assemblag-
843 es with fayalitic olivine. American Mineralogist 73, 727–740.
844 Ghaffari, M., Rashidnejad-Omran, N., Dabiri, R., Chen, B., Santos, J. F., 2013. Mafic–
845 intermediate plutonic rocks of the Salmas area, northwestern Iran: their source and petrogenesis sig-
846 nificance, International Geology Review 55 (16), 2016–2029.

Ghalamghash, J., Vousoughi-Abedini, M., Bellon, H., Emami, M. H., Pourmoafi, M., Rashid, H., 2003. K/Ar age dating of Oshnavieh plutonic complex. Iranian Quarterly Journal of Geosciences 11(47-48), 16–27.

Ghalamghash, J., Nedelec, A., Bellon, H., Vousoughi-Abedini, M., Bouchez, J. L., 2009a. The Urumieh plutonic complex (NW Iran): a record of the geodynamic evolution of the Sanandaj–Sirjan zone during Cretaceous times- part I: petrogenesis and K/Ar dating. Journal of Asian Earth Sciences 35, 401–415.

Ghalamghash, J., Mirnejad, H., Rashid, H., 2009b. Mixing and mingling of mafic and felsic magmas along the Neo-Tethys continental margin, Sanandaj-Sirjan zone, NW Iran: A case study from the Alvand pluton. Neues Jahrbuch für Mineralogie, Abhandlungen 186, 79–93.

Gómez-Tuena, A., LaGatta, A., Langmuir, C. H., Goldstein, S. L, Ortega-Gutierrez, F., Carrasco-Nunez, G., 2003. Temporal control of subduction magmatism in the eastern Trans-Mexican Volcanic Belt: Mantle sources, slab contributions, and crustal contamination. G3, Published by AGU and the Geochemical Society, 8912, doi: 10.1029/2003GC000524.

Govers, R., Wortel, M. J. R., 2005. Lithosphere tearing at STEP faults: Response to edges of subduction zones. Earth and Planetary Science Letters 236, 505–523, doi:10.1016/j.epsl.2005.03.022.

Green, D. H., Ringwood, A. E., 1967. The genesis of basaltic magmas. Contributions to Mineralogy and Petrology 15, 103–190.

Gorring, M. L., Kay, S. M., Zeitler, P. K., Ramos, V. A., Rubiolo, D., Fernández, M. I. and Panza, J. L., 1997, Neogene Patagonian plateau lavas: continental magmas associated with ridge collision at the Chile Triple Junction. Tectonics 16, 1-17.

Guest, B., Stockli, D. F., Grove, M., Axen, G. J., Lam, P. S., Hassanzadeh, J., 2006b. Thermal histories from the central Alborz Mountains, northern Iran: implications for the spatial and temporal

distribution of deformation in northern Iran. Geological Society of America Bulletin 118, 1507-1521.

Hamada, M., Fujii, T., 2007. H_2O-rich island arc low-K tholeiite magma inferred from Ca-rich plagioclase-melt inclusion equilibria. Geochemical Journal 41, 437–461.

Hassanzadeh, J., Stockli, D. F., Horton, B. K., Axen, G. J., Stockli, L. D., Grove, M., Schmitt, A. K., 2008. U–Pb zircon geochronology of late Neoproterozoic–Early Cambrian granitoids in Iran: implications for paleogeography, magmatism, and exhumation history of Iranian basement. Tecto-nophysics 451, 71–96.

Hart, S. R., 1984. A large scale isotope anomaly in the southern hemisphere mantle. Nature 309, 753–757.

Hirose, K., Kushiro, I., 1993. Partial melting of dry peridotites at high pressures: determination of compositions of melts segregated from peridotite using aggregates of diamond. Earth and Planetary Science Letters 114, 477–489.

Hofmann, A.W., 1988. Chemical differentiation of the Earth: the relationship between mantle continental crust and oceanic crust. Earth and Planetary Science Letters 90, 297–314.

Hofmann, A.W., 2005. Sampling mantle heterogeneity through oceanic basalts: isotopes and trace Elements, in Carlson, R.W., eds., The mantle and core, Elsevier, Amsterdam, 61–101.

Hofmann, J.E., Münker, C., Naeraa, T., Rosing, M.T., Herwartz, D., Garbe-Schöenberg, D., Svahnberg, H., 2011, Mechanisms of Archean crust formation inferred from high-precision HFSE systematics in TTGs: Geochimica et Cosmochimica Acta, v. 75, p. 4157–4178.

Hoskin, P.W.O., Schaltegger, U., 2003. The compositions of zircon and igneous and metamor-phic petrogenesis. Reviews in Mineralogy and Geochemistry 53, 27–55.

Irvine, T. N., Baragar, W.R.A., 1971. A guide to the chemical classification of common volcanic rocks. Canadian Journal of Earth Sciences 8, 523–547.

Jahn, B. M., Wu, F. Y., Lo, C. H., 1999. Crust–mantle interaction induced by deep subduction of the continental crust: geochemical and Sr– Nd isotopic evidence from post-collisional mafic-ultramafic intrusions of the northern Dabie Complex, Central China. Chemical Geology 157, 119–146.

Jaques, A. L., Green, D. H., 1980. Anhydrous melting of peridotite at 0-15 kbar pressure and the genesis of tholeiitic basalts. Contributions to Mineralogy and Petrology 73, 287–310.

Jicha, B. R, Singer, B. S., Beard, B. L., Johnson, C. M., Moreno-Roa, H., Naranjo, J. A., 2007. Rapid magma ascent and generation of ^{230}Th excesses in the lower crust at Puyehue–Cordón Caulle, Southern Volcanic Zone, Chile, Earth and Planetary Science Letters 255, 229–242.

Hastie, A.R., Mitchell, S.F., Kerr, A.C., Minifie, M.J., Millar, I.L., 2011. Geochemistry of rare high-Nb basalt lavas: are they derived from a mantle wedge metasomatised by slab melts? Geochim. Cosmochim. Acta 75, 5049–5072

Kepezhinskas, P., McDermott, F., Defant, M. J., Hochstaedter, A., Drummond, M. S., Hawkes-worth, C. J., Koloskov, A., Maury, R. C., Bellon, H., 1997. Trace element and Sr–Nd–Pb isotopic constraints on a three-component model of Kamchatka arc petrogenesis. Geochimica et Cosmo-chimica Acta 61, 577–600.

Khalaf, E.A., Khalaf, M., F., 2010. Polybaric evolution of the volcanic rocks at Gabal Nuqara, north eastern desert, Egypt. In: Biswajit Gh., Gautam S., Jyotisnkr R., (eds). Topics in Igneous Pe-trology, Springer-Verlag, 277-317.

Kheirkhah, M., Neill, I., Allen, M. B., Ajdari. K., 2013. Small-volume melts of lithospheric man-tle during continental collision: Late Cenozoic lavas of Mahabad, NW Iran, Journal of Asian Earth Sciences 74, 37–49.

Kheirkhah, M., Neill, I., Allen, M. B., 2015. Petrogenesis of OIB-like basaltic volcanic rocks in a continental collision zone: Late Cenozoic magmatism of Eastern Iran. J. Asian Earth Sci.http://dx.doi.org/10.1016/j.jseaes.2015.02.027.

Kelemen, P.B., Yogodzinski, G.M., Scholl, D.W., 2003.Along-strike variation in the Aleutian Island Arc: genesis of high Mg# andesite and implications for continental crust. Inside the Subduction Factory.AGU, Washington, DC 223–276.

Koop, W.J., Stoneley, R., Ridd, M.F., Murphy, R.W., Osmaston, M.F., Kholief, M.M., 1982. Subsidence history of the Middle East Zagros Basin, Permian to Recent (and discussion). Philosophical Transactions of the Royal Society A, 305, 149-167.

Lan, C. Y., Lee, T., Wang Lee, C., 1990. The Rb-Sr isotopic record in Taiwan gneisses and its tectonic implication. Tectonophysics 183, 129–143.

Langmuir, C. H, Vocke, R. D. Jr., Gilbert, N. H., Stanley, R. H., 1978. A general mixing equation with applications to Icelandic basalts. Earth and Planetary Science Letters 37, 380–392.

Lassiter, J. C., Hauri, E. H., Reiners, P. W., M. Garcia, O., 2000. Generation of Hawaiian post-erosional lavas by melting of a mixed lherzolite/pyroxenite source, Earth and Planetary Science Letters 178, 269–284.

Lundstrom, C.C., Hoernle, K., Gill, J., 2003. U-series disequilibria in volcanic rocks from the Canary Islands: Plume versus lithospheric melting. Geochimca Cosmochimca Acta 67, 4153-4177.

McDermott, F., Delfin, F.G., Defant, M.J., Turner, S., Maury, R., 2005. The petrogenesis of magmas from Mt. Bulusan and Mayon in the Bicol arc, the Philippines. Contributions to Mineralogy and Petrology 150, 652–670.

Macdonald, R., Hawkesworth, C.J., Heath, E., 2000. The Lesser Antilles volcanic chain: a study in arc magmatism. Earth-Science Reviews 49, 1–76.

Macpherson, C. G., Dreher, S. T., Thirlwall, M. F., 2006. Adakites without slab melting: high pressure processing of basaltic island arc magma, Mindanao, the Philippines. Earth Planet. Sci. Lett. 243, 581–593.

Mahmoudi, S., Corfu, F., Masoudi, F., Mehrabi, B., Mohajjel, M., 2011. U–Pb dating and emplacement history of granitoid plutons in the northern Sanandaj–Sirjan Zone, Iran. Journal of Asian Earth Sciences 41, 238–249.

Marquez, A., Oyarzun, R., Doblas, M., and Verma, S. P., 1999, Alkalic (OIB type) and calc-alkalic volcanism in the Mexican volcanic belt: A case for plume-related magmatism and propagating rifting at an active margin? Geology 27, 51–54.

Mazhari, S.A., Bea, F., Amini, S., Ghalamghash, J., Molina, J.F., Montero, P., Scarrow, J.H., Williams, I.S., 2009. The Eocene bimodal Piranshahr massif of the Sanandaj–Sirjan Zone, NW Iran: a marker of the end of the collision in the Zagros orogeny. Journal of the Geological Society of London 166, 53–69.

McBride N, Glimour L, An introduction to the solar system. Cambridge University Press, 46 p.

McDonough, W. F., 1990. Constraints on the composition of the continental lithospheric mantle. Earth and Planetary Science Letters, 101, 1-18, Elsevier Science Publishers B.V., Amsterdam.

McQuarrie, N., Van Hinsbergen, D. J. J., 2013. Retrodeforming the Arabia-Eurasia collision zone: age of collision versus magnitude of continental deformation. Geology 41, 315-318.

Mederer, J., Moritz, R., Ulianov, A., Chiaradia, M., 2013. Middle Jurassic to Cenozoic evolution of arc magmatism during Neotethys subduction and arc-continent collision in the Kapan Zone, southern Armenia. Lithos 177, 61–78.

Meurer, W. P., Claeson, D. T., 2002. Evolution of crystallizing interstitial liquid in an arc-related cumulate determined by LA ICPMS mapping of a large amphibole oikocryst. Journal of Petrology 43, 607–629.

964 Miyashiro, a., 1974. Volcanic rock series in island arc and active continental margin. Am. J. Sci.,
965 274, 321-55.
966 Mohajjel, M., Fergusson, C.L., 2000. Dextral transpression in Late Cretaceous continental colli-
967 sion, Sanandaj–Sirjan zone, Western Iran. J. Struct. Geol. 22, 1125–1139.
968 Mohajjel, M., Fergusson, C. L., 2014. Jurassic to Cenozoic tectonics of the Zagros Orogen in
969 northwestern Iran. International Geology Review 56, 263–287.
970 Morley, C.K., Kongwung, B., Julapour, A.A., Abdolghafourian, M., Hajian, M., Waples, D.,
971 Warren, J., Otterdoom, H., Srisuriyon, K., Kazemi, H., 2009. Structural development of a major late
972 Cenozoic basin and transpressional belt in central Iran: the Central Basin in the Qom–Saveh area.
973 Geosphere 5 (4), 325–362.
974 Moyen, J.F., Martin, H., Jayananda, M., 2001. Multi-element geochemical modelling of crust-
975 mantle interactions during late-Archaean crustal growth: the Closepet granite (South India). Prec.
976 Res. 112, 87–105.
977 Mouthereau, F., Lacombe, O., Vergés, J., 2012. Building the Zagros collisional orogeny: Timing,
978 strain distribution and the dynamics of Arabia/Eurasia convergence, Tectonophysics 532, 27–60.
979 Namur, O., Charlier, B., Toplis, M.J., Higgins, M.D., Liégeois, J.P., Vander Auwera, J., 2010.
980 Crystallization Sequence and Magma Chamber Processes in the Ferrobasaltic Sept Iles Layered In-
981 trusion, Canada. Journal of Petrology 51 (6), 1203-1236.
982 Neill, I., Gibbs, J.A., Hastie, A.R., Kerr, A.C., 2010. Origin of the volcanic complexes of La Dé-
983 sirade, Lesser Antilles: Implications for tectonic reconstruction of the Late Jurassic to Cretaceous
984 Pacific-proto Caribbean margin. Lithos 120, 407–420.
985 Neill, I., Meliksetian, Kh., Allen, M.B., Navarsardyan, G., Karapetyan, S., 2013. Pliocene– Quater-
986 nary volcanic rocks of NW Armenia: magmatism and lithospheric dynamics within an active oro-
987 genic plateau. Lithos 180–181, 200–215.

988 Neill, I., Meliksetian, K., Allen, M. B., Navasardyan, G., Kuiper, K., 2015. Petrogenesis of mafic
989 collision zone magmatism: The Armenian sector of the Turkish–Iranian Plateau. Chemical Geology
990 403, 24–41.
991 Nogole Sadat, M. A. A., Houshmandzadeh, A., 1993. Geology map of Marivan-Baneh, Scale
992 1:250000. Geology Survey of Iran.
993 Omrani, J., 2008. Arc-magmatism and subduction history beneath the Zagros Mountains, Iran: a
994 new report of adakites and geodynamic consequences. Lithos 106, 380–398.
995 Palme, H., O'Neill, H.St.C., 2003. Cosmochemical constraints of mantle composition. Treatise
996 Geochem. 2, 1–38.
997 Pearce, J. A., Norry, M. J., 1979, Petrogenetic implications of Ti, Zr, Y and Nb variations in vol-
998 canic rocks: Contributions to Mineralogy and Petrology 69, 33–47.
999 Pearce, J. A., Bender, J. F., De Long, S. E., Kidd, W. S. F., Low, P. J., GÜner, Y., Saroglu, F.,
1000 Yilmaz, Y., Moorbath, S., Mitchell, J. G., 1990. Genesis of collision volcanism in Eastern Anatolia,
1001 Turkey. Journal of Volcanology and Geothermal Research 44, 189–229.
1002 Pearce, J. A., Peate, D. W., 1995. Tectonic implications of the composition of volcanic arc mag-
1003 mas. Annual Reviews in Earth and Planetary Sciences 23, 251–285.
1004 Perfit, M. R., Gust, D. A., Bence, A. E., Arculus, R. J., Taylor, S. R., 1980. Chemical character-
1005 istics of island-arc basalts: implications for mantle sources. Chemical Geology 30, 227–256.
1006 Petford, N., Gallagher, K., 2001. Partial melting of mafic (Amphibolitic) lower crust by periodic
1007 influx of basaltic magma. Earth Planet. Sci. Lett.193, 483–499.
1008 Petrone, C. M., 2010. Relationship between monogenetic magmatism and stratovolcanoes in
1009 western Mexico: The role of low-pressure magmatic processes. Lithos 19, 585-606.
1010 Ramos, V. A., Kay, S. M., l992. Southern Patagonian plateau basalts and deformation: backarc
1011 testimony of ridge collision. Tectonophysics 205, 261–282.

René, M., Titanite-ilmenite assemblage in microgranitoids from the northeastern margin of the Klenov granite body (Bohemian Massif, Czech Republic). Acta Geodynamica et Geomaterialia Journal 8, 164, 479–487.

Richard, J. P., Uilrich, T., Kerrich, R., 2006. The Late Miocene-Quaternary Antofulla volcanic complex, southern Puna, NW Argentina: protracted history, diverse petrology, and economic potential. Journal of Volcanology and Geothermal Resource 152, 197–239

Robinson, J. A. C., Wood, B. J., 1998. The depth of the spinel to garnet transition at the peridotite solidus. Earth and Planetary Science Letters 164, 277–284.

Rosenbaum, G., Gasparon, M., Lucente, F. P., Peccerillo, A., Miller, M. S., 2008. Kinematics of slab tear faults during subduction segmentation and implications for Italian magmatism. Tectonics 27, TC2008, doi: 10.1029/2007TC002143.

Sacks, P. E., Secor, D. T., 1990. Delamination in collisional orogens. Geology 18, 999–1002, doi: 10.1130/0091-7613(1990)018<0999:DICO>2.3.CO;2.

Saki, A., 2010. Proto-Tethyan remnants in northwest Iran: geochemistry of the gneisses and metapelitic rocks. Gondwana Research 17, 704–714.

Salavati, M., 2008. Petrology, Geochemistry and Mineral Chemistry of Extrusive Alkalic Rocks of the Southern Caspian Sea Ophiolite, Northern Alborz, Iran: Evidence of Alkaline Magmatism in Southern Eurasia. Journal of Applied Sciences 8, 12, doi: 10.3923/jas.2008.2202.2216.

Sandeman, H. A., Cousens, B.L., Hemmingway, C.J., 2003. Continental tholeiitic mafic rocks of the Paleoproterozoic Hurwitz Group, Central Hearne sub-domain, Nunavut: insight into the evolution of the Hearne sub-continental lithosphere. Canadian Journal of Earth Sciences 40, 1219–1237.

Saleeby, J., 2003. Segmentation of the Laramide Slab–Evidence from the southern Sierra Nevada region. Geological Society of America Bulletin 115, 655–668.

Sepahi, A. A., 2008. Typology and petrogenesis of granitic rocks in the Sanandaj-Sirjan metamorphic belt, Iran: with emphasis on the Alvand plutonic complex. Neues Jahrbuch für Geologie und Paleontologie Abhandlungen 247, 3, 295–312.

Sepahi, A. A, Shahbazi, H., Siebel, W., Ranin, A., 2014. Geochronology of plutonic rocks from the Sanandaj-Sirjan Zone, Iran and new zircon and titanite U-Th-Pb ages for granitoids from the marivan pluton. Geochronometria 41, 3, 207–215.

Shahbazi, H., Siebel, W., Pourmoafee, M., Ghorbani, M., Sepahi, A. A., Shang, C. K., ousoughi-Abedini, M., 2010. Geochemistry and U–Pb zircon geochronology of the Alvand plutonic complex in Sanandaj–Sirjan Zone Iran: New evidence for Jurassic magmatism. Journal of Asian Earth Sciences 39, 668–683.

Shinjo, R., Woodhead, J. D., Hergt, J. M., 2000. Geochemical variation within the northern Ryukyu arc: Magma source compositions and geodynamic implications. Contributions to Mineralogy and Petrology 140, 263–282.

Stern, C. R., 1989. Pliocene to present migration of the volcanic front, Andean southern volcanic zone. Revista Geológica de Chile 16, 145-162.

Streckeisen, A. L., 1967. Classification and nomenclature of igneous rocks. Final report of an inquiry. Neues Jahrbuch für Mineralogie, Abhandlungen 107, 144–200.

Sun, S. S., McDonough, W. F., 1989. Chemical and isotopic systematics of oceanic basalts: implications for mantle composition and processes. In: Saunders A. D, Norry M, eds, Magmatism in Ocean Basins. Geological Society of London Special Publication 42, 313–345.

Snyder, D., Carmichael, ISE., Wiebe, R. A.,1993. Experimental study of liquid evolution in an Fe-rich, layered mafic intrusion: constraints of Fe-Ti oxide precipitation on the T-fO_2 and T-r paths of tholeiitic magmas. Contributions to Mineralogy and Petrology 113, 73–86.

Takagi, D., Sato, H., Nakagawa, M., 2005. Experimental study of a low-alkali tholeiite at 1–5 kbar: optimal condition for the crystallization of high-An plagioclase in hydrous arc tholeiite. Contributions to Mineralogy and Petrology 149, 527–540.

Tatsumi, Y., Eggind, S.M., 1995. Subduction zone magmatism. Blackwell, Oxford.

Tatsumi, Y., Suzuki, T., 2009. Tholeiitic vs. calc-alkalic differentiation and evolution of arc crust: constraints from melting experiments on a basalt from the Izu-BoninMariana arc. Journal of Petrology 50, 1575-1603.

Verdel, C., Wernicke, B.P., Hassanzadeh, J., Guest, B., 2011. A Paleogene extensional arc flare-up in Iran. Tectonics 30, Tc3008.

Verdel, C., Wernicke, B. P., Hassanzadeh, J., Guest, B., 2011. A Paleogene extensional arc flare-up in Iran. Tectonics 30, TC3008, doi:10.1029/2010TC002809.

Vincent, S. J., Allen, M. B., Ismail-Zadeh, A. D., Flecker, R., Foland, K. A., Simmons, M. D., 2005. Insights from the Talysh of Azerbaijan into the Paleogene evolution of the South Caspian region. Geological Society of America Bulletin 117, 1513–1533.

Vogel, D. C., Keays, R. R., James, R. S., Reeves, S. J, 1999. The geochemistry and petrogenesis of the Agnew intrusion, Canada: a product of S-undersaturated, high-Al and low-Ti tholeiitic magmas. Journal of Petrology 40, 423–450.

Weaver, B. L., 1991. The origin of ocean island basalt end-member compositions: trace element and isotopic constraints, Earth and Planetary Science Letters104, 381–397.

Winter, J. D., 2001. An Introduction to Igneous and Metamorphic Petrology. Upper Saddle River, NJ: Prentice-Hall Inc. ISBN 0321592573.

Whitney, D.L., Evans, B.W., 2010. Abbreviations for name of rock-forming minerals. American Mineralogist 95, 185–187.

Wittke, J. H., Mack, L. E., 1993. OIB-like mantle source for continental alkaline rocks of the Balcones province, Texas: trace elements and isotopic evidence. Journal of Petrology 101, 333–344.

Wolff, J. A., Rowe, M. C., Teasdale, R., Gardner, J. N., Ramos, F. C., Heikoop, C. E. 2005. Petrogenesis of Pre-caldera Mafic Lavas, Jemez Mountains Volcanic Field (New Mexico, USA), Journal of Petrology 46, 407–439.

Workman, R. K., Hart, S. R., 2005. Major and trace element composition of the depleted MORB mantle (DMM), Earth and Planetary Science Letters 231, 53–72.

Xu, Y., Huang, X. L., Ma, J. L., Wang, Y. B., Lizuka, Y., Xu, J. F., Wang, Q., Wu, X. Y., 2004b. Crust-mantle interaction during the tectonothermal reactivation of the North China Craton, constraints from SHRIMP zircon U–Pb chronology and geochemistry of Mesozoic plutons from western Shandong. Contributions to Mineralogy and Petrology 147, 750–767.

Zellmer, G.F., Annen, C., Charlier, B.L.A., George, R.M.M., Turner, S.P., Hawkesworth, C.J., 2005. Magma evolution and ascent at volcanic arcs: constraining petrogenetic processes through rates and chronologies. Journal of Volcanology and Geothermal Research 140, 171–191.

Zhang, H. F., Sun, M., Zhou, X. H., Fan, W. M., Zai, M.G., Ying, J. F., 2002. Mesozoic lithosphere destruction beneath the North China Craton: evidence from major-, trace -element and Sr–Nd–Pb isotope studies of Fangcheng basalts. Contributions to Mineralogy and Petrology 144, 241–253.

Zhang, H.F., Sun, M., Zhou, X.H., Ying, J.F., 2005a. Geochemical constraints on the origin of Mesozoic alkaline intrusive complexes from the North China Craton and tectonic implications. Lithos 81, 297–317.

Zindler, A., Hart, S., 1986. Chemical dynamics. Annual Reviews of Earth and Planetary Science 14, 493–571.

Figure

Fig. 1

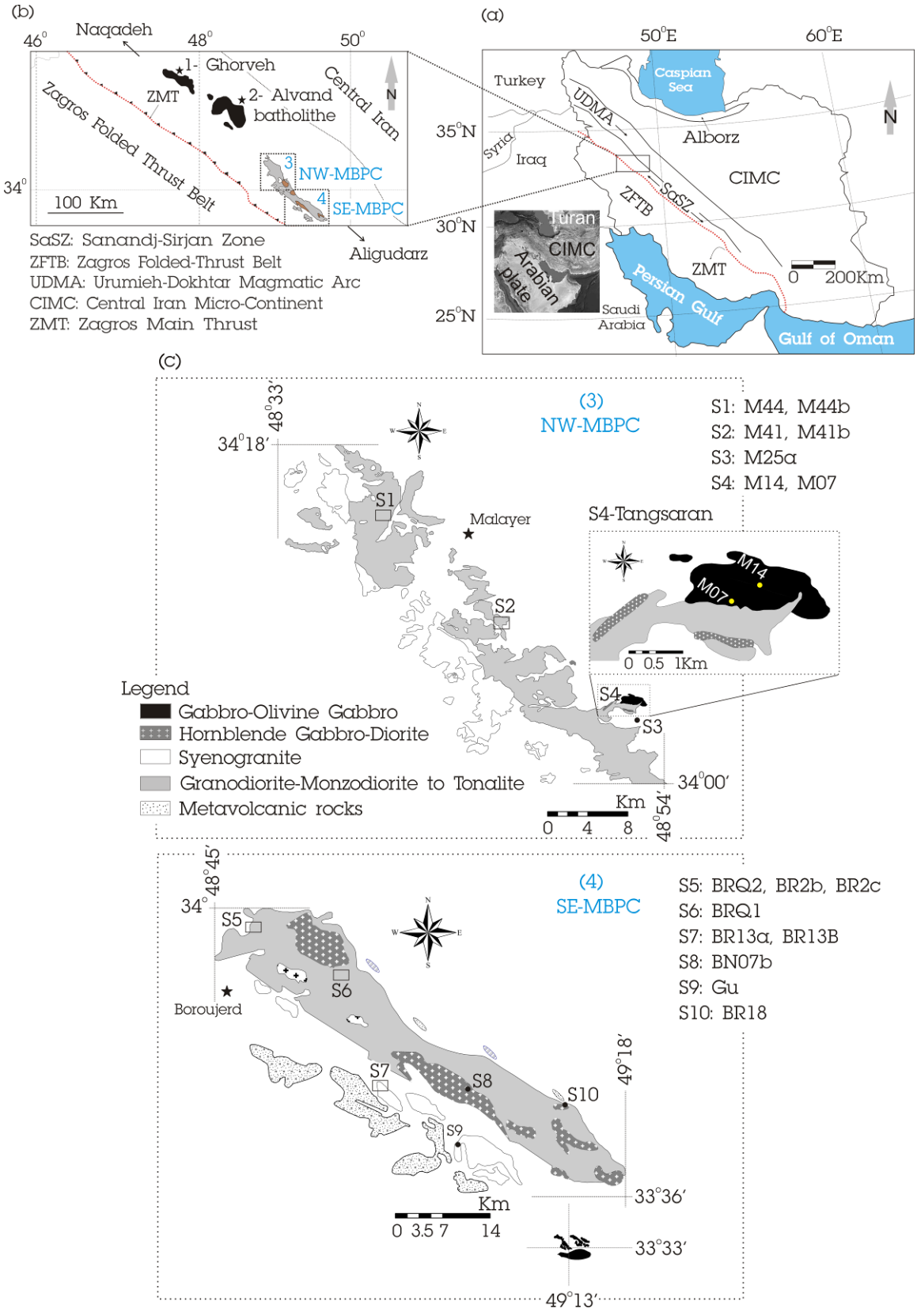
(b)
Naqadeh
46°
48°
50°
1- Ghorveh
2- Alvand batholithe
ZMT
Zagros Folded Thrust Belt
Central Iran
N
3 NW-MBPC
4 SE-MBPC
34°
100 Km
Aligudarz
SaSZ: Sanandj-Sirjan Zone
ZFTB: Zagros Folded-Thrust Belt
UDMA: Urumieh-Dokhtar Magmatic Arc
CIMC: Central Iran Micro-Continent
ZMT: Zagros Main Thrust
(a)
50°E
60°E
Turkey
Caspian Sea
UDMA
Alborz
N
35°N
Syria
Iraq
CIMC
ZFTB
SaSZ
Turan
Arabian plate
30°N
ZMT
0 200Km
Persian Gulf
Saudi Arabia
25°N
Gulf of Oman
(c)
48°33′
34°18′
(3) NW-MBPC
S1: M44, M44b
S2: M41, M41b
S3: M25a
S4: M14, M07
S1
Malayer
S4-Tangsaran
M14
M07
S2
0 0.5 1Km
S4
S3
Legend
Gabbro-Olivine Gabbro
Hornblende Gabbro-Diorite
Syenogranite
Granodiorite-Monzodiorite to Tonalite
Metavolcanic rocks
34°00′
Km
0 4 8
48°54′
48°45′
34°
(4) SE-MBPC
S5: BRQ2, BR2b, BR2c
S6: BRQ1
S7: BR13a, BR13B
S8: BN07b
S9: Gu
S10: BR18
S5
S6
Boroujerd
49°18′
S7
S8
S10
S9
Km
0 3.5 7 14
33°36′
33°33′
49°13′

Fig. 2

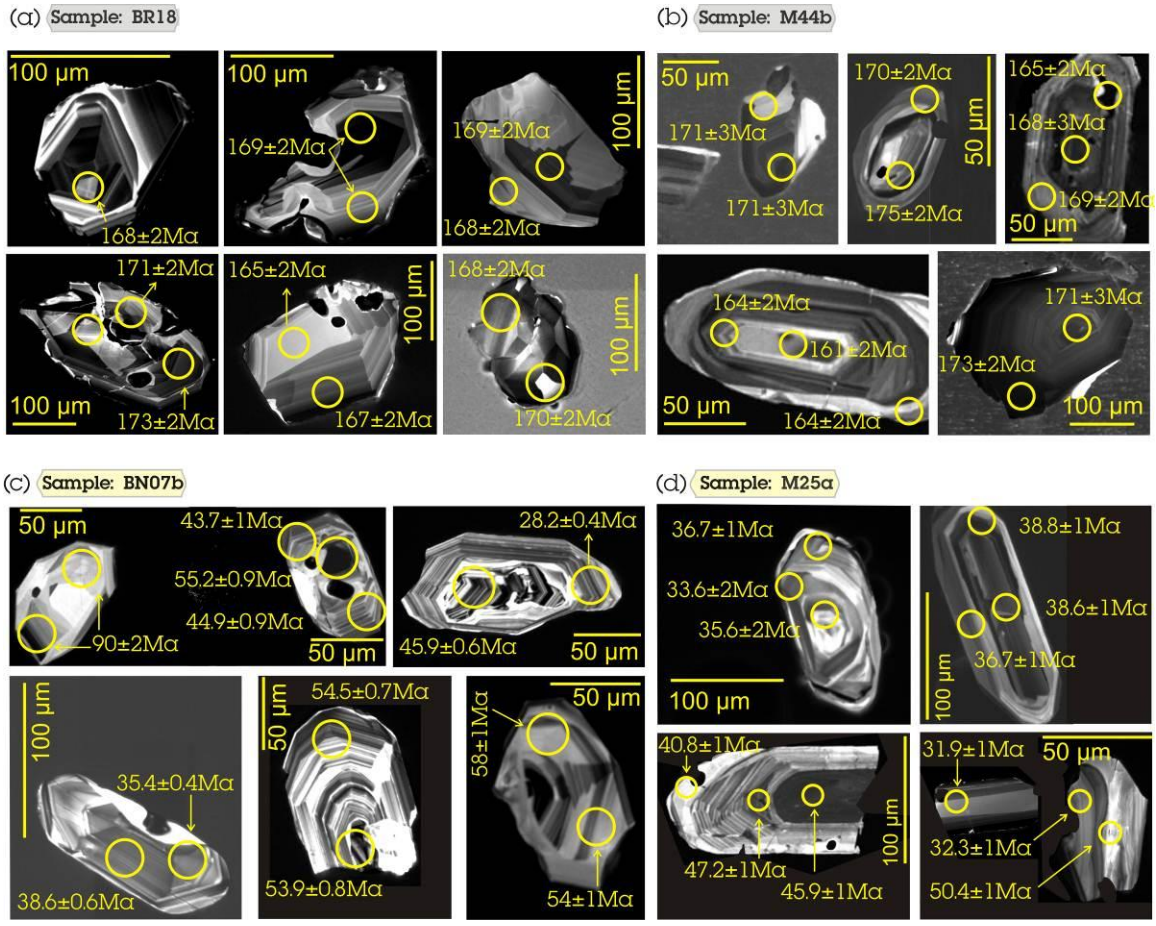
(a) Sample: BR18
100 μm
168±2Mα
169±2Mα
171±2Mα
173±2Mα
165±2Mα
167±2Mα
168±2Mα
170±2Mα
(b) Sample: M44b
50 μm
171±3Mα
175±2Mα
170±2Mα
165±2Mα
168±3Mα
169±2Mα
164±2Mα
161±2Mα
173±2Mα
(c) Sample: BN07b
43.7±1Mα
55.2±0.9Mα
44.9±0.9Mα
90±2Mα
28.2±0.4Mα
45.9±0.6Mα
35.4±0.4Mα
38.6±0.6Mα
54.5±0.7Mα
53.9±0.8Mα
58±1Mα
54±1Mα
(d) Sample: M25α
36.7±1Mα
33.6±2Mα
35.6±2Mα
38.8±1Mα
38.6±1Mα
36.7±1Mα
40.8±1Mα
47.2±1Mα
45.9±1Mα
31.9±1Mα
32.3±1Mα
50.4±1Mα

Fig. 3

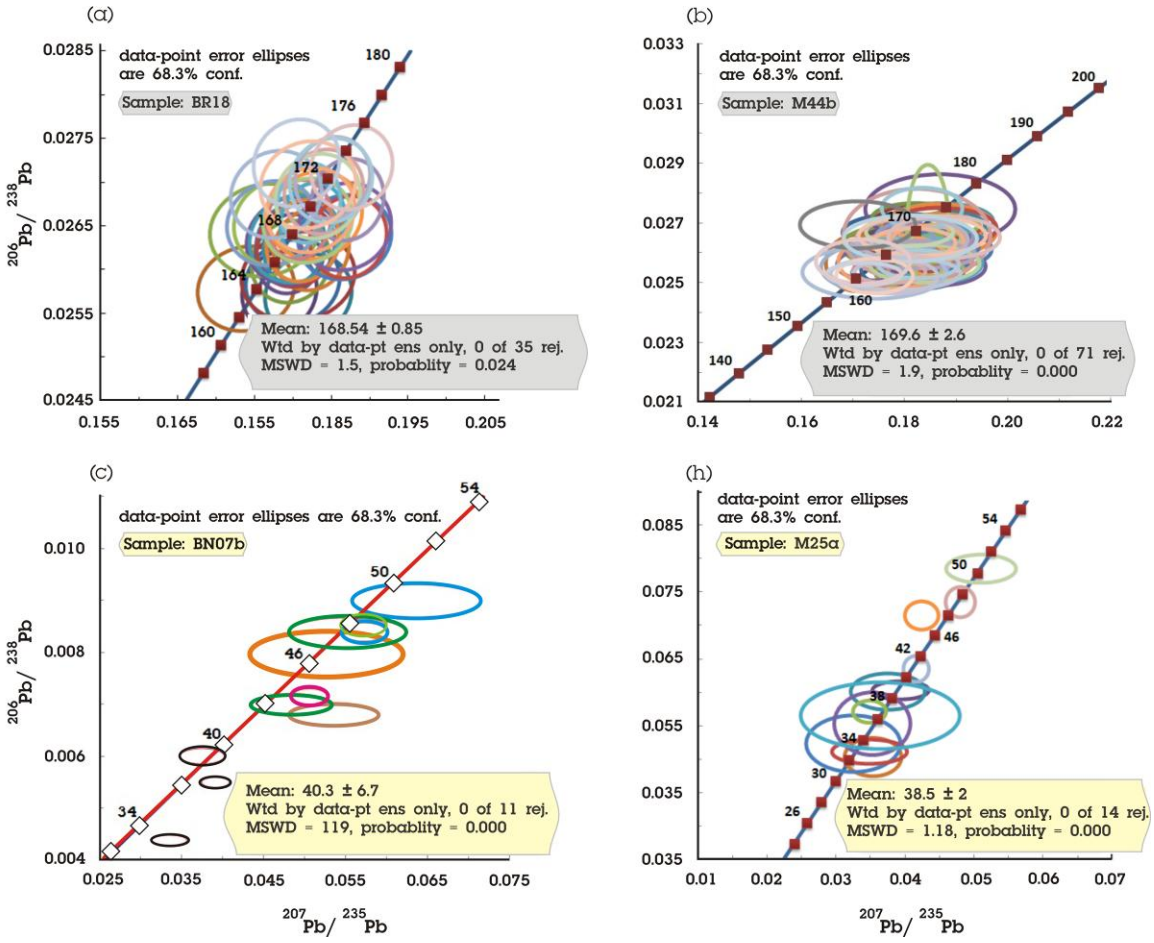
(a)
data-point error ellipses are 68.3% conf.
Sample: BR18
Mean: 168.54 ± 0.85
Wtd by data-pt ens only, 0 of 35 rej.
MSWD = 1.5, probablity = 0.024
(b)
data-point error ellipses are 68.3% conf.
Sample: M44b
Mean: 169.6 ± 2.6
Wtd by data-pt ens only, 0 of 71 rej.
MSWD = 1.9, probablity = 0.000
(c)
data-point error ellipses are 68.3% conf.
Sample: BN07b
Mean: 40.3 ± 6.7
Wtd by data-pt ens only, 0 of 11 rej.
MSWD = 119, probablity = 0.000
(h)
data-point error ellipses are 68.3% conf.
Sample: M25a
Mean: 38.5 ± 2
Wtd by data-pt ens only, 0 of 14 rej.
MSWD = 1.18, probablity = 0.000
206Pb/238Pb
207Pb/235Pb

Fig. 4

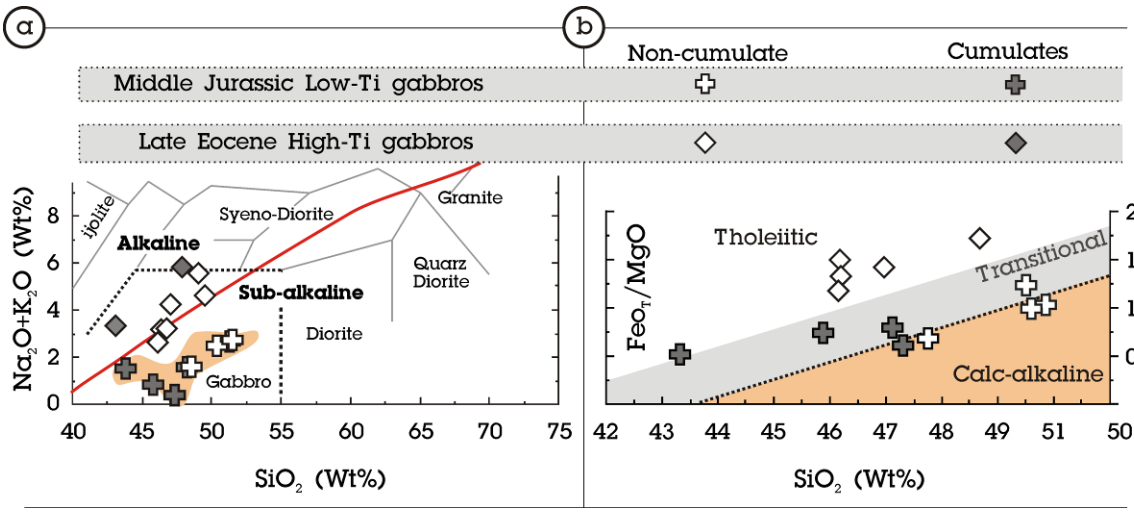
a
b
Non-cumulate
Cumulates
Middle Jurassic Low-Ti gabbros
Late Eocene High-Ti gabbros
Na2O+K2O (Wt%)
SiO2 (Wt%)
Ijolite
Alkaline
Syeno-Diorite
Granite
Quarz Diorite
Sub-alkaline
Diorite
Gabbro
FeoT/MgO
Tholeiitic
Transitional
Calc-alkaline

Fig. 5

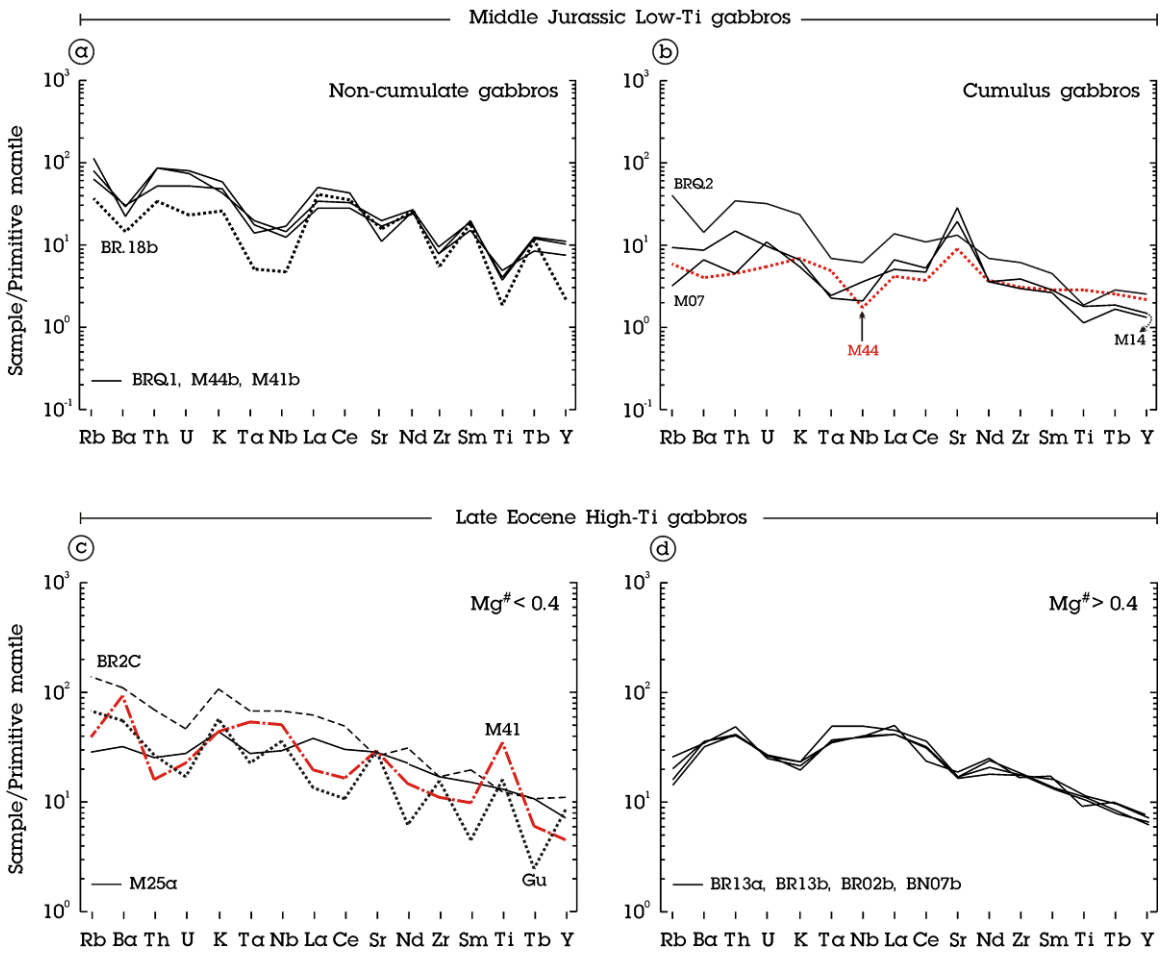
Middle Jurassic Low-Ti gabbros
a
Non-cumulate gabbros
BR.18b
BRQ1, M44b, M41b
b
Cumulus gabbros
BRQ2
M07
M44
M14
Late Eocene High-Ti gabbros
c
Mg# < 0.4
BR2C
M41
Gu
M25a
d
Mg# > 0.4
BR13a, BR13b, BR02b, BN07b
Sample/Primitive mantle
Rb Ba Th U K Ta Nb La Ce Sr Nd Zr Sm Ti Tb Y

Fig. 6

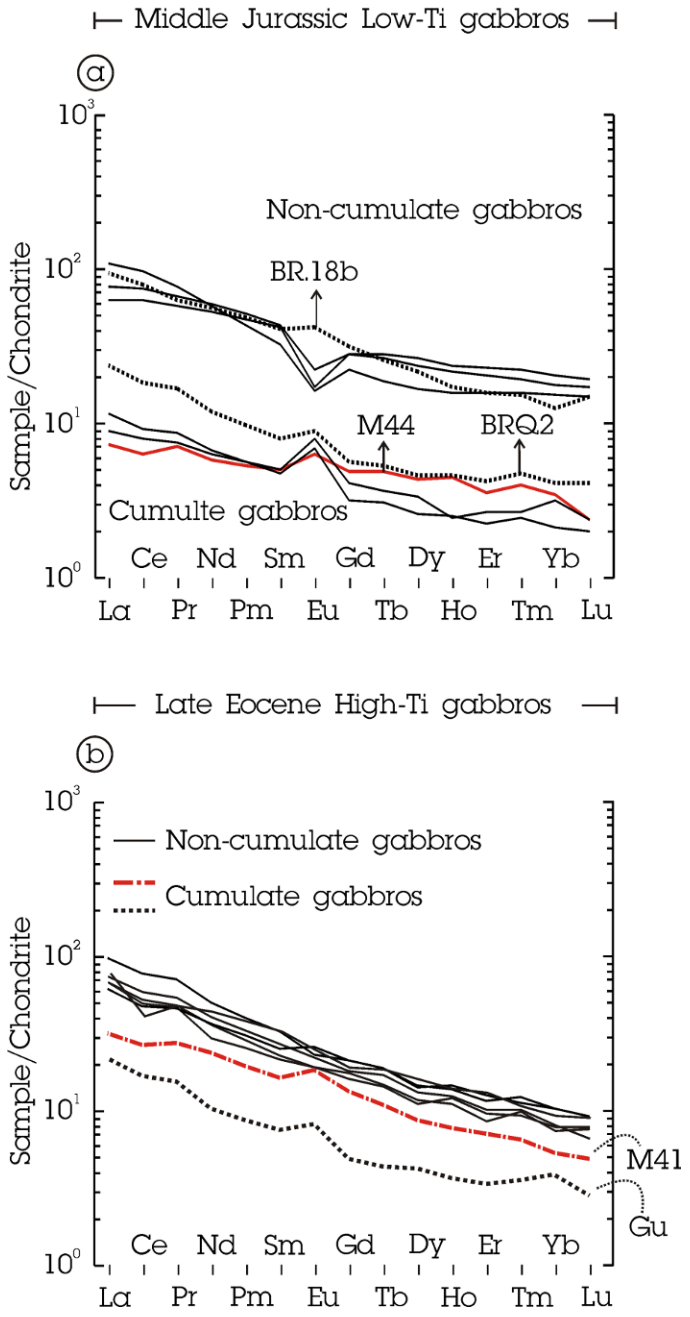
Middle Jurassic Low-Ti gabbros
a
Non-cumulate gabbros
BR.18b
M44
BRQ2
Cumulte gabbros
Sample/Chondrite
Ce Nd Sm Gd Dy Er Yb
La Pr Pm Eu Tb Ho Tm Lu
Late Eocene High-Ti gabbros
b
Non-cumulate gabbros
Cumulate gabbros
M41
Gu

Fig. 7

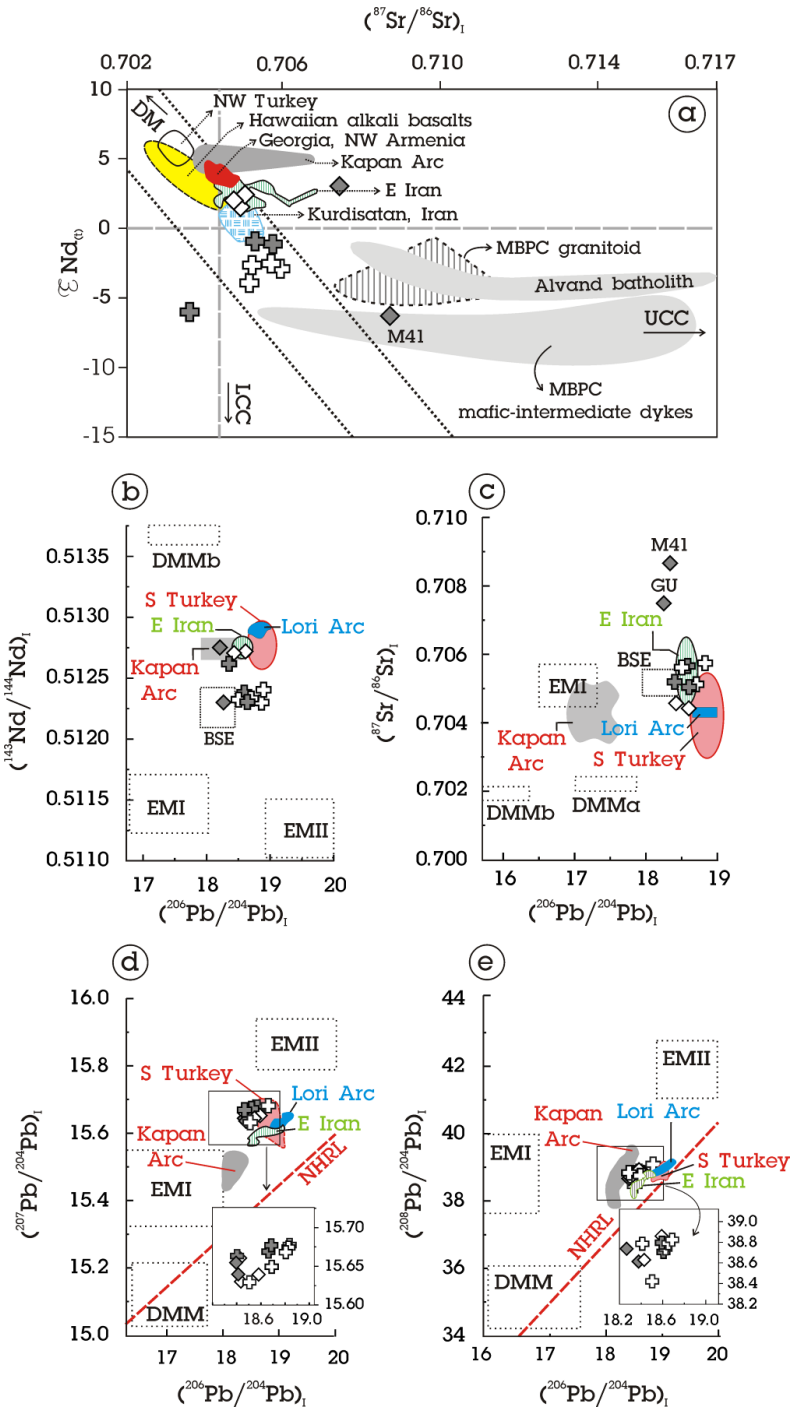
(87Sr/86Sr)i
0.702
0.706
0.710
0.714
0.717
10
5
0
-5
-10
-15
εNdω
DM
NW Turkey
Hawaiian alkali basalts
Georgia, NW Armenia
Kapan Arc
E Iran
Kurdisatan, Iran
MBPC granitoid
Alvand batholith
UCC
M41
MBPC
mafic-intermediate dykes
LCC
a
b
0.5135
0.5130
0.5125
0.5120
0.5115
0.5110
(143Nd/144Nd)i
DMMb
S Turkey
E Iran
Lori Arc
Kapan
Arc
BSE
EMI
EMII
17
18
19
20
(206Pb/204Pb)i
c
0.710
0.708
0.706
0.704
0.702
0.700
(87Sr/86Sr)i
M41
GU
E Iran
BSE
EMI
Kapan
Arc
Lori Arc
S Turkey
DMMb
DMMa
16
17
18
19
(206Pb/204Pb)i
d
16.0
15.8
15.6
15.4
15.2
15.0
(207Pb/204Pb)i
EMII
S Turkey
Lori Arc
E Iran
Kapan
Arc
EMI
NHRL
DMM
15.70
15.65
15.60
18.6
19.0
17
18
19
20
(206Pb/204Pb)i
e
44
42
40
38
36
34
(208Pb/204Pb)i
EMII
Kapan
Arc
Lori Arc
EMI
S Turkey
E Iran
NHRL
DMM
39.0
38.8
38.6
38.4
38.2
18.2
18.6
19.0
16
17
18
19
20
(206Pb/204Pb)i

Fig. 8

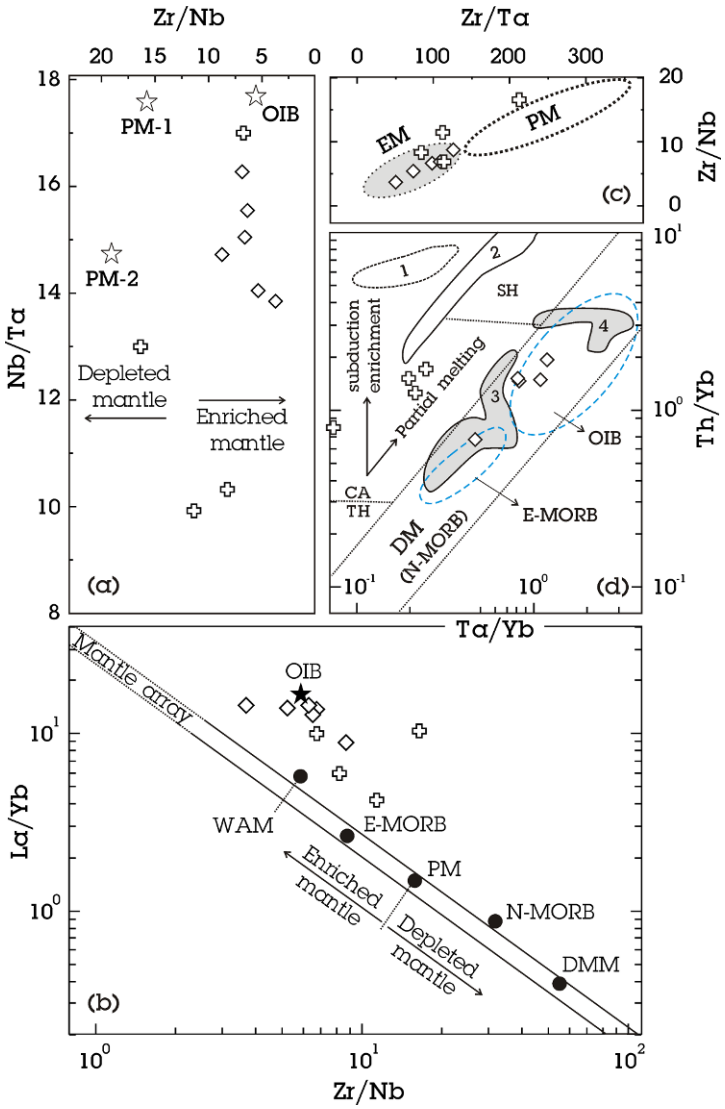
Zr/Nb
Zr/Tα
Nb/Tα
Th/Yb
Zr/Nb
Tα/Yb
La/Yb
Zr/Nb
PM-1
OIB
PM-2
Depleted mantle
Enriched mantle
(a)
EM
PM
(c)
1
2
SH
4
3
subduction enrichment
Partial melting
OIB
CA
TH
E-MORB
DM (N-MORB)
(d)
Mantle array
OIB
WAM
E-MORB
PM
N-MORB
DMM
Enriched mantle
Depleted mantle
(b)

Fig. 9

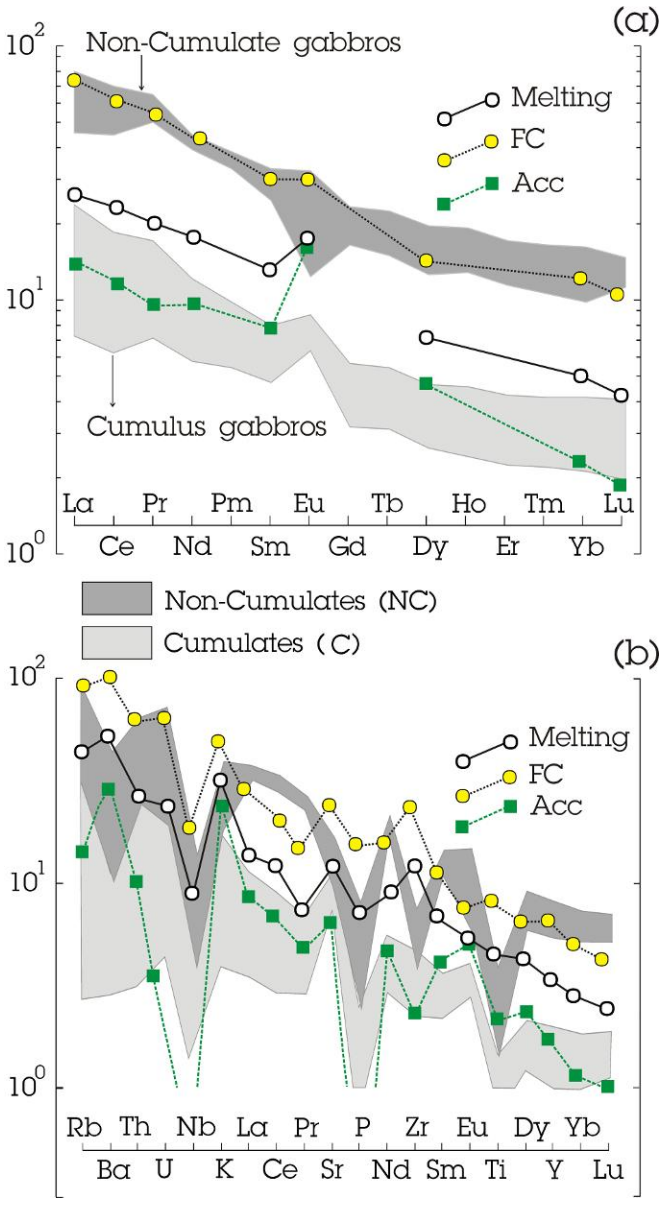
(a)
Non-Cumulate gabbros
Melting
FC
Acc
Cumulus gabbros
La Pr Pm Eu Tb Ho Tm Lu
Ce Nd Sm Gd Dy Er Yb
Non-Cumulates (NC)
Cumulates (C)
(b)
Melting
FC
Acc
Rb Th Nb La Pr P Zr Eu Dy Yb
Ba U K Ce Sr Nd Sm Ti Y Lu

Fig. 10

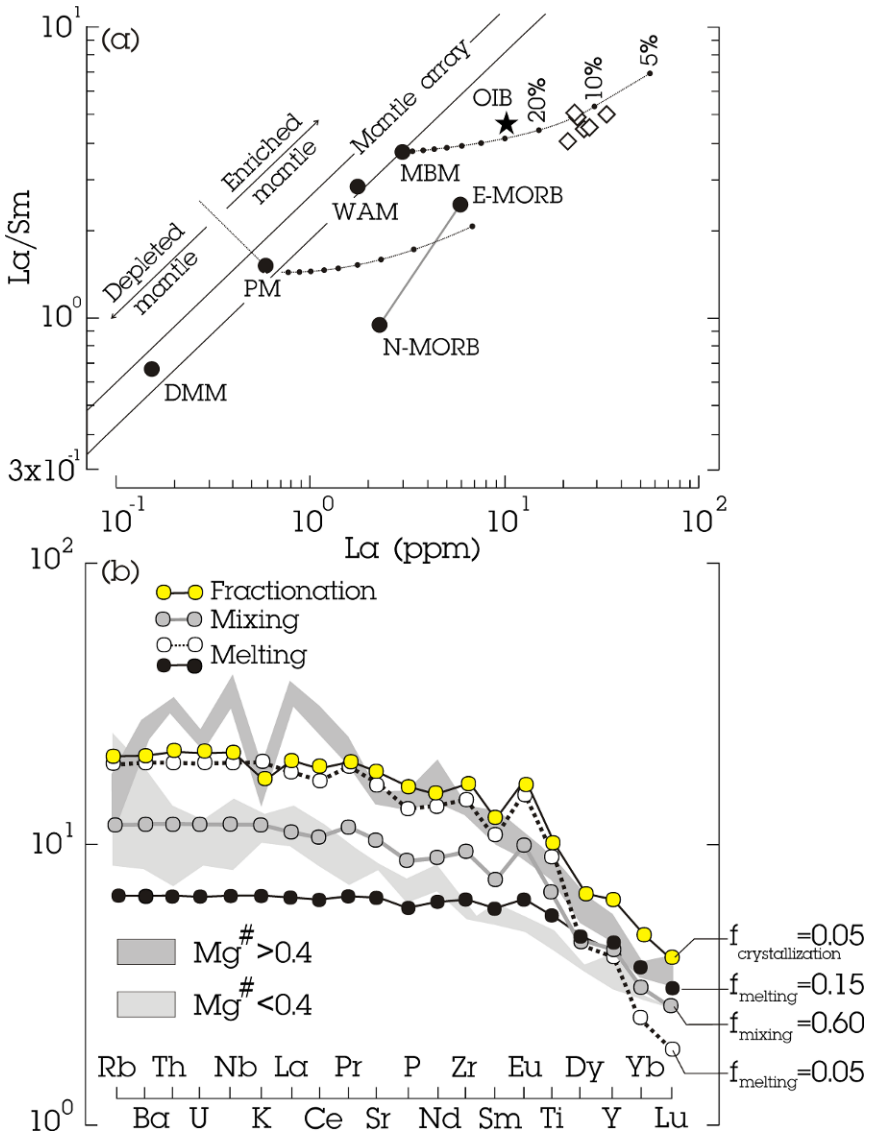
(a)
La/Sm
La (ppm)
Mantle array
Enriched mantle
Depleted mantle
OIB
20%
10%
5%
MBM
WAM
E-MORB
PM
N-MORB
DMM
(b)
Fractionation
Mixing
Melting
Mg# >0.4
Mg# <0.4
Rb Th Nb La Pr P Zr Eu Dy Yb
Ba U K Ce Sr Nd Sm Ti Y Lu
f crystallization =0.05
f melting =0.15
f mixing =0.60
f melting =0.05

FIGURE CAPTIONS

Fig. 1 a) The geological subdivision of Iran and the NW-SE trending SaSZ; b) The location of the MBPC in the N-SaSZ; c) Simplified geological maps of the northwestern (3) and southeastern (4) parts of the MBPC (modified map from Ahmadi Khalaji et al., 2007; Deevsalar et al., 2014). Sampling locations are shown by the letter S. Those locations which are enclosed by a rectangle contain more than one sample. The area enlarged in (c) shows outcrops of intrusive rocks in Tangsaran Hill.

Fig. 2 Representative cathodoluminescence (CL) images of zircon grains for four gabbroic intrusions from the MBPC and U-Pb zircon ages for analyzed spots. The crystals did not contain xenocrystic cores and exhibit well-developed concentric compositional zoning.

Fig. 3 U–Pb concordia plots and weighted averages of zircon ages for the selected gabbros. (a) BR_{18} and (b) M_{44}b: Middle Jurassic gabbro, (c) BN_{07b} and M_{25a}: Late Eocene gabbro.

Fig. 4 The MBPC gabbros on (a) a TAS diagram (Irvine and Baragar, 1971) and (b) a FeO_T/MgO vs. SiO_2 plot (Miyashiro, 1974).

Fig. 5 Primitive mantle-normalized spider diagrams for the MBPC mafic intrusive rocks. (a, b) Middle Jurassic low-Ti gabbros, (c, d) Late Eocene high-Ti gabbros. Trace element abundances for primitive mantle are from Sun and McDonough (1989).

Fig. 6 Chondrite-normalized rare earth element patterns for the MBPC mafic intrusive rocks. (a) Middle Jurassic low-Ti gabbros. (b) Late Eocene high-Ti gabbros. REE abundances for chondrite are from Sun and McDonough (1989).

Fig. 7 a) $(^{87}Sr/^{86}Sr)_i$ vs. $\varepsilon Nd_{(t)}$ plot for the MBPC mafic intrusive rocks. The white band enclosed by the thin dotted line shows the mantle array. Sr-Nd isotope composition of MBPC granitoids (Ahadnejad et al., 2010); MBPC tholeiitic dykes (Deevsalar, 2015), Hawaiian alkali basalt (Zindler and Hart, 1986); Upper Jurassic-Lower Cretaceous mafic rocks from Kapan arc (Mederer et al., 2013); Georgia and Pleistocene mafic alkaline rocks from NW Armenia (Mereder et al., 2013; Neill et al., 2015); Kurdistan (Allen et al., 2013); Alvand Batholith (Shahbazi et al., 2010); b, c) Initial Sr and Nd isotopic values plotted against $^{206}Pb/^{204}Pb$. d, e) Correlation plot of $^{206}Pb/^{204}Pb$ vs. $^{207}Pb/^{204}Pb$ and $^{208}Pb/^{204}Pb$ for the MBPC mafic intrusive rocks. EMI, EMII, HIMU and DMM are from Shimuda (2009); Karacadag, S. Turkey (Ekici et al., 2014); E Iran (Kheirkhah et al., 2015); Upper Jurassic-Lower Cretacous mafic rocks from Kapan Arc (Mederer et al. 2013); Pleistocene mafic alkaline rocks from Lori Province, NE Armenia (Neill et al., 2015). Dotted parallel lines represent the mantle array (position from Zhang et al., 2005a). Modern TIP analyses are all Pliocene-Quaternary and so have not been corrected to initial values

Fig. 8 HFSE ratios used to constrain the source characteristics of the MBPC non-cumulate gabbros. (a) Nb/Ta vs. Zr/Nb plot. PM-1 and OIB (Sun and McDonough (1989), PM-2 (Palme and O'Neill, 2004); (b) La/Yb vs. Zr/Nb plot (Aldanmaz et al., 2006); (c) Zr/Nb vs. Zr/Ta plot, and (d) Th/Yb vs. Ta/Yb plot (after Pearce, 1983). Enclosed area in Fig.7d, are: 1- Upper Jurassic- Late Cretaceous arc rocks from Kapan, Armenia (Mederer et al., 2013), 2- Middle Jurassic tholeiitic dykes from the MBPC, 3- Late Eocene tholeiitic dykes from the MBPC and 4- alkaline rocks from East Iran

(Kheirkhah et al., 2015). PM, N-, E-MORB and OIB after Sun and McDonough (1989). WAM is from Aldanmaz et al., 2000.

Fig. 9 (a) REE and (b) Trace element modeling of mixing, melting and fractionation processes for the low-Ti gabbros. Melting of metasomatised mantle peridotite (mixing between PM and subduction components) is shown, with amphibole-bearing garnet-spinel lherzolite composition and subsequent fractional crystallization-accumulation (Modelling in Supplementary Item 3, Table 4).

Fig. 10 (a) La/Sm vs. La (ppm) plot for high-Ti gabbros. Non-modal batch melting vectors are plotted in this figure. MBM: Malayer-Boroujerd Mantle source, (b) Trace element modeling of melting and fractional crystallization events (Supplementary Item 3, Table 5). The parameters for non-modal batch melting models and Rayleigh fractional crystallization (FC) are given in Supplementary Item 3, Tables 1 and 2. Normalizing values are from Sun and McDonough (1989). The mixing equation is from Langmuir et al. (1978).

Table

Table 1
The mineralogy and texture of the MBPC mafic intrusive rocks.

Rock type			Groups/Samples		Major Mineral phases	Main texture		Accessory minerals		Secondary minerals	
			Middle Jurassic	Late Eocene		Middle Jurassic	Late Eocene	Middle Jurassic	Late Eocene	Middle Jurassic	Late Eocene
Olivine gabbro	(1)*	C	BRQ2*[1]	—	olivine, clinopyroxene, plagioclase, hornblende	Cumulative, Medium grained, Poikilitic, subhederal to anhedral grains		spinel, pyrite, Ilmenite	—	sericite, chlorite	—
		NC	BR18b	M25a		Granular, Fine grained, subhederal	porphyritic ± poikilitic	quartz, zircon, Ilmenite	zircon, hematite	—	sericite, chlorite
	(2)*	C	M44*[1]	M41*[1]		Cumulative, Fine grained, subhederal to euhedral Poikilitic	Cumulative, Medium grained, Poikilitic, Intergranular	Ilmenite, spinel, pyrite	magnesio-chromite, ilmenite, chlorite	—	—
		NC	—	—		—		—		—	
Hornblende gabbro		C	M14*[2], M07*[2]	—	Plagioclase, hornblende ± clinopyroxene	Poikilitic, Cumulative, medium grained, euhedral to subhederal grains		zircon, ilmenite, apatite	—	biotite, sericite, chlorite	—
		NC	BRQ1, M44b, BR13a	BN07b,BR02b, BR02c		Intergranular, fine to medium grained, subhederal to anhedral	Granular, fine grained, subhederal to anhedral ± poikilitic	apatite, zircon, hematite	apatite, zircon, hematite	sericite, chlorite	—
Hornblende clinopyroxene gabbro		C	—	Gu*[2]	Plagioclase, hornblende, clinopyroxene ± orthopyroxene	Cumulative, Poikilitic, subhederal to anhedral grains		—	ilmenite, apatite	—	biotite, sericite
		NC	M41b	BR13b		Granular, Medium grained, subhederal to anhedral	Intergranular, fine grained, anhedral ± poikilitic	apatite, ilmenite, hematite	zircon, ilmenite, hematite	chlorite	—

(1)* Cpx: 10-15 Vol%, Ol ~ 10 Vol%

(2)* Cpx ~ 20 Vol%, Ol ~ 30 Vol%

Cumulate: C; Non-Cumulate: NC ; *[1] Olivine-rich cumulates *[2] Plagioclase-rich cumulates

Table 2
Whole-rock major and trace element composition of the MBPC mafic intrusive rocks.

Middle Jurassic low-Ti gabbros								
Sampling location	S10	S6	S1	S2	S5	S4		S1
	Non-Cumulate (NC)				Cumulate (C)			
Sample name	BR18*	BRQ1	M44b	M41b	BRQ2	M14	M07*	M44*
	(Wt %)							
SiO_2	47.75	49.52	49.61	49.87	47.12	45.89	47.31	43.34
TiO_2	0.29	0.77	0.6	0.64	0.31	0.19	0.3	0.47
Al_2O_3	15.76	15.67	14.26	13.06	14.69	18.09	19.99	12.7
FeO_T	9.35	9.79	9.04	9.69	10.32	8.39	5.54	11.23
MnO	0.15	0.18	0.16	0.18	0.16	0.13	0.11	0.15
MgO	13.79	7.92	9.13	9.47	13.17	11.41	9.22	21.93
CaO	10.26	10.18	11.3	11.09	9.97	14.04	16.15	7.4
Na_2O	1.02	1.54	1.64	1.39	0.98	0.7	0.61	1.33
K_2O	0.54	0.99	0.89	1.21	0.52	0.15	0.12	0.15
P_2O_5	0.05	0.12	0.07	0.16	0.05	0.02	0.02	0.05
LOI	0.97	2.33	2.22	2.23	2.14	0.94	0.51	0.56
Total	99.93	99.01	98.92	98.99	99.43	99.95	99.88	99.31
Mg#	0.60	0.45	0.50	0.49	0.56	0.58	0.62	0.66
	(ppm)							
Cs	7.5	4.72	3.85	3.57	8.81	1.01	1.3	2.7
Rb	19.8	33.16	41.65	59.02	22.36	5.2	1.8	3.3
Ba	71	149.1	144.8	112	76.13	44.88	35	21
Th	2.1	3.22	5.19	5.3	2.24	0.97	0.3	0.3
U	0.4	0.9	1.29	1.37	0.59	0.18	0.2	0.1
Nb	2.6	9.36	7.85	6.85	3.55	1.21	2.1	1
Pb	4.27	5.34	8	14.04	3.71	2.03	1.31	0.41
Sr	269.6	193.7	344.05	293.8	245.1	353.76	513.3	166.7
Hf	1.2	1.01	1.1	1.06	1.08	0.3	0.5	0.7
Zr	42.5	63	64.3	77.8	53	25	33.4	26.6
Y	7.2	25.01	33.96	37.14	8.94	4.64	5.1	7.5
Cr	7.8	362	1068	818.5	643.8	841	33	25.2
Ni	13.8	77.16	343.9	221.1	130.5	43.86	12.6	615.4
Co	16.6	39.41	80.53	40.16	67.7	46.17	10.4	64
V	63	275.5	281.3	229.4	405.3	254.7	19	9
Ta	0.2	0.55	0.76	0.69	0.29	0.09	0.1	0.2
P	218.2	523.7	305.5	698.3	218.2	87.3	87.3	218.2
Ti	1738.6	4616.2	3597	3836.8	1858.5	1139.1	1798	2817.7
K	4483.1	8219.0	7388.8	10045.4	4317.0	1245.3	996.2	1245.3
La	22.3	26.15	18.35	15	7.78	3.76	2.9	2.4
Ce	48.7	60.02	46.03	38.55	15.89	7.83	6.8	5.4
Pr	6.06	7.24	6.42	5.57	1.9	0.98	0.84	0.8
Nd	26.6	27.14	27.99	24.79	7.57	4.17	4	3.6
Sm	6.25	5.02	6.73	6.44	1.62	0.95	1.03	1.03
Eu	2.48	0.95	1.31	0.99	0.68	0.53	0.61	0.49
Gd	6.44	4.55	5.82	5.72	1.55	0.87	1.14	1.35
Tb	0.97	0.71	1.01	1.06	0.25	0.15	0.17	0.23
Dy	5.56	4.33	6.08	6.69	1.59	0.9	1.14	1.49
Ho	0.99	0.89	1.22	1.35	0.32	0.18	0.17	0.31
Er	2.59	2.62	3.41	3.85	0.94	0.5	0.6	0.8
Tm	0.39	0.4	0.5	0.57	0.14	0.07	0.08	0.12
Yb	2.15	2.59	3.07	3.53	0.91	0.47	0.69	0.76
Lu	0.38	0.39	0.44	0.5	0.14	0.07	0.08	0.08
∑REE	131.86	142.98	128.37	114.6	41.29	21.43	20.25	18.86
Eu*/Eu	1.19	0.60	0.63	0.49	1.30	1.76	1.72	1.28
$(La/Yb)_N$	7.45	7.25	4.29	3.05	6.14	5.74	3.02	2.27
Sr/Y	37.44	7.74	10.13	7.91	27.42	76.24	100.6	22.23
K/Nb	1724.27	878.10	941.25	1466.48	1216.06	1029.17	474.38	1245.30
Rb/Nb	1724	878	941	1466	1216	1029	474	1245
La/Nb	8.58	2.79	2.34	2.19	2.19	3.11	1.38	2.40
Sr/Nd	10.14	7.14	12.29	11.85	32.38	84.83	128.3	46.31
Ba/Rb	3.59	4.50	3.48	1.90	3.40	8.63	19.44	6.36
Nb/Y	0.36	0.37	0.23	0.18	0.40	0.26	0.41	0.13

The highlighted samples (*) are from Deevsalar et al. (2014). The trace element contents of these rocks were calculated in ACME laboratory. Other samples were analyzed in University of the Ryukyus, Japan. The analytical method and procedure are represented in supplementary item 1.

Table 2 continued

Late Eocene high-Ti gabbros								
Sampling location	S9	S2	S3	S5	S7	S5	S7	S8
	(C)		(NC)					
	Mg# < 0.4				Mg# > 0.4			
Sample name	Gu	M41*	M25a*	BR2C	BR13b*	BR02b*	BR13a	BN07b
(Wt %)								
SiO_2	47.75	42.49	48.68	48.85	46.2	46.16	46.18	46.84
TiO_2	2.57	5.47	2.06	1.94	1.82	1.69	1.86	1.49
Al_2O_3	17.38	14.24	17.04	15.57	14.23	13.33	14.23	13.61
FeO_T	11.69	14.02	10	11.9	13.25	13.46	14.83	13.75
MnO	0.21	0.19	0.16	0.18	0.18	0.19	0.18	0.18
MgO	4.34	6.99	5.83	5.4	10.03	11.47	9.88	9.75
CaO	8.87	11.65	10.04	9.37	9.39	9.32	9.46	9.51
Na_2O	3.92	2.33	3.78	2.78	2.56	2.16	2.52	2.98
K_2O	1.23	0.95	0.95	1.3	0.51	0.43	0.52	0.95
P_2O5	0.74	0.1	0.33	0.43	0.34	0.3	0.34	0.4
LOI	0.75	0.65	0.88	1.31	0.72	1.43	-	0.66
Total*[1]	99.45	99.08	99.75	99.03	99.23	99.94	100	99.86
Mg#	0.27	0.33	0.37	0.31	0.43	0.46	0.40	0.41
(ppm)								
Cs	2.5	1.9	2	8	0.3	0.3	0.43	2.01
Rb	36.9	21.1	15.4	74.76	9	8	11.19	14.4
Ba	281	463	160	550.8	188	167	188.6	177.02
Th	1.7	1	1.6	4.37	2.6	2.7	2.69	3.1
U	0.3	0.4	0.5	0.82	0.5	0.5	0.47	0.45
Nb	19.7	28	16.2	37.54	22.8	22.6	28.14	22.1
Pb	2.77	6.47	0.94	63.35	1.96	1.51	5.2	3.7
Sr	512	517.4	498.5	462.15	310.1	301.6	305.5	334.9
Hf	2.9	2.4	3.4	0.91	3.9	3.6	1.9	3.4
Zr	129.3	90.5	140.4	138	154.1	147.5	147.8	139.8
Y	28.4	15.4	24.1	37.22	21.2	22.5	24.72	26.10
Cr	66.8	0.5	5.8	104.9	193.1	260.4	263.8	102.96
Ni	85	14.2	20.5	48.44	109.3	131.7	202.6	264.9
Co	26.2	26.6	21.1	35.99	33.3	32.8	64.27	52.7
V	43	118	65	243.9	54	48	232.9	55
Ta	0.9	2.1	1.1	2.71	1.4	1.5	2	1.42
P	3229.5	436.4	1440.2	1876.6	1483.8	1309.3	1483.8	1745.68
Ti	15407.2	32792.7	12349.7	11630.3	10910.9	10131.6	11150.7	8932.55
K	10211.5	7886.9	7886.9	10792.6	4234.0	3569.9	4317.0	8052.94
La	7.3	10.8	21	33.46	23.5	23.2	25.43	27.25
Ce	15	23.4	42.3	69.09	46.9	45	52.39	54.5
Pr	1.75	3.18	5.29	8.12	5.66	5.39	6.35	5.5
Nd	6.6	15.4	24	32.77	23.4	19.6	26.33	27
Sm	1.57	3.36	5.19	6.71	4.81	4.59	5.69	6.05
Eu	0.65	1.43	2.06	1.82	1.54	1.55	1.78	1.75
Gd	1.4	3.82	5.97	5.95	5.08	4.7	5.27	4.87
Tb	0.21	0.52	0.91	0.92	0.73	0.7	0.85	0.88
Dy	1.48	3.06	4.98	5.15	4.16	4	4.77	5.02
Ho	0.26	0.56	1.05	1	0.8	0.87	0.92	1
Er	0.78	1.62	2.89	2.69	2.03	2.25	2.36	2.65
Tm	0.11	0.2	0.35	0.37	0.31	0.29	0.31	0.33
Yb	0.88	1.2	2.35	2.3	1.72	1.82	1.83	1.88
Lu	0.1	0.17	0.32	0.32	0.27	0.28	0.24	0.31
∑REE	38.09	68.72	118.66	170.66	120.91	114.24	134.52	138.99
Eu*/Eu	1.32	1.22	1.13	0.87	0.95	1.02	0.98	0.96
$(La/Yb)_N$	5.95	6.46	6.41	10.44	9.80	9.14	9.97	10.40
Sr/Y	18.03	33.60	20.68	12.42	14.63	13.40	12.36	12.83
K/Nb	518.35	281.68	486.85	66.35	185.70	157.96	153.41	364.39
Rb/Nb	1.87	0.75	0.95	1.99	0.39	0.35	0.40	0.65
La/Nb	0.37	0.386	1.30	0.89	1.03	1.03	0.90	1.23
Sr/Nd	77.58	33.60	20.77	14.10	13.25	15.39	11.60	12.4
Ba/Rb	7.62	21.94	10.39	7.37	20.89	20.88	16.85	12.29
Nb/Y	0.69	1.82	0.67	1.01	1.08	1.00	1.14	0.84

- The highlighted samples (*) are from Deevsalar et al. (2014). The trace element contents of these rocks were calculated in ACME laboratory.
- Other samples were analyzed in University of the Ryukyus, Japan. The analytical method and procedure are represented in supplementary item 1.

Table 3
Sr-Nd isotopic composition of the MBPC mafic intrusive rocks.

	Group-1: Low-Ti gabbros (Age: ~168 Ma)							Group-2: High-Ti gabbros (Age: ~40 Ma)				
Samples	BRQ1	BR18	BQd*[1]	BRQ2	M44	M07	M14	M41	Gu	BR2C	BR13a	BN07b*[4]
Rb (ppm)	33.20	19.80	37.10	22.40	3.30	1.80	5.20	21.10	36.90	74.80	11.20	14.4
Sr (ppm)	193.70	269.60	281.20	245.10	166.70	513.30	353.80	517.40	512.00	462.20	305.50	334.9
$^{87}Sr/^{86}Sr$	0.70711	0.70634	0.70529	0.70649	0.70364	0.70547	0.70518	0.70878	0.70761	0.70481	0.70448	0.70508
Error×10^{-6} *[2]	7	7	7	6	7	6	6	7	7	7	6	7
$^{87}Rb/^{86}Sr$	0.50	0.21	0.38	0.26	0.06	0.01	0.04	0.12	0.21	0.47	0.11	0.12
$(^{87}Sr/^{86}Sr)i$	0.70593	0.70583	0.70508	0.70586	0.70350	0.70545	0.70508	0.70872	0.70749	0.70454	0.70442	0.70501
	Group-1 (Age: ~168 Ma)							Group-2 (Age: ~40 Ma)				
Sm	5.02	1.57	4.44	1.62	1.03	1.03	0.95	3.36	6.25	6.71	5.69	6.05
Nd	27.14	6.60	21.50	7.57	3.60	4.00	4.17	15.40	26.60	32.77	26.33	27.00
$^{143}Nd/^{144}Nd$	0.51242	0.51246	0.51241	0.51252	0.51230	0.51256*[4]	0.51244	0.51231	0.51279	0.51272	0.51273	0.51275
Error×10^{-6} *[2]	5	7	6	19*[3]	7	8	6	6	5	7	6	7
$(^{143}Nd/^{144}Nd)i$	0.51229	0.51231	0.51227	0.51237	0.51210	0.51239	0.51229	0.51228	0.51276	0.51269	0.51270	0.51272
εNd(t)	-2.48	-2.27	-2.92	-0.96	-6.18	-0.70	-2.62	-6.10	3.20	1.90	2.20	2.50

*[1] Because of incomplete data set, this sample did not show in Table 2.

*[2] Standard error at the 1-sigma level

*[3] Error×10^{-5}

*[4] Estimated at Royal Museum for Central Africa, Earth Sciences**,** Belgium**.**

*[5] εNd(t)= -6.2, by re-estimating of at isotope laboratory of "Royal Museum for Central Africa, Earth Sciences, Belgium"

Table 4
Lead isotope composition of the MBPC mafic intrusive rocks.

Groups	Samples	$^{206}Pb/^{204}Pb$ (measured)	$^{207}Pb/^{204}Pb$ (measured)	$^{208}Pb/^{204}Pb$ (measured)	U	Th	Pb	$^{206}Pb/^{204}Pb(t)$	$^{207}Pb/^{204}Pb(t)$	$^{208}Pb/^{204}Pb(t)$
low-Ti gabbros (~168 Ma)	BRQ1	19.10	15.69	39.34	0.90	5.22	5.34	18.64	15.67	38.78
	BR18	18.73	15.64	38.80	0.40	2.10	2.77	18.49	15.63	38.40
	M44B	18.88	15.68	39.07	1.29	5.19	8.00	18.62	15.67	38.72
	M41B	18.80	15.68	38.98	1.37	5.30	14.04	18.64	15.67	38.78
	BQd	18.71	15.65	38.84	0.01	0.03	0.10	18.67	15.65	38.80
	M7	18.77	15.68	38.85	0.30	0.20	1.31	18.40	15.66	38.77
	M14	18.75	15.68	38.95	0.18	0.97	2.03	18.61	15.67	38.70
	BRQ2	18.84	15.68	39.10	0.59	2.24	3.71	18.58	15.67	38.78
high-Ti gabbros (~40Ma)	Gu	18.48	15.66	38.75	1.70	0.30	4.27	18.33	15.65	38.74
	M41	18.44	15.64	38.61	1.00	0.40	6.47	18.38	15.64	38.60
	BR2C	18.43	15.66	38.63	0.82	4.37	3.65	18.34	15.66	38.48
	M29B	18.44	15.63	38.65	0.36	1.67	10.83	18.43	15.63	38.63
	BR13a	18.60	15.64	38.88	0.47	2.69	5.20	18.57	15.64	38.81
Standard Sample: Mean (n=20)		16.9437	15.5010	36.7236						
2SD		0.0023	0.0028	0.0053						

Table 5
Mafic rocks derived from different mantle source beneath the Turkish–Iranian Plateau.

Location	Origin	References
Quaternary mafic rocks from S-Turkey	mixing between depleted and enriched mantle magma	Ekici et al., 2014
Cenozoic alkaline mafic rocks from E Iran	DMM-EMII-like mantle source	Kheirkhah et al., 2013
Upper Jurassic-Lower Cretaceous mafic rocks from Kapan Arc	subduction-related magmatism metasomatized mantle source	Mederer et al., 2013
Middle Jurassic tholeiitic mafic-intermediate dykes from the MBPC	subduction-related magmatism metasomatized amphibole-bearing peridotite	Deevsalar et al. (in review)
Middle Jurassic calc-alkaline granitoids from MBPC	subduction-related magmatism	Ahmadi-Khalaji et al., 2007; Ahadnejad et al., 2010
Middle Jurassic granitoids, Alvand	subduction-related magmatism	Shahbazi et al., 2010; Mahmoudi et al. 2011
Georgia	subduction modified mantle source	Mederer et al., 2013
Shirak, NW Armenia	<5% non-modal partial melting of heterogeneous metasomatised, amphibole-bearing peridotite	Neill et al., 2015
Late Miocene–Quaternary mafic rocks from Mahabad	melting of amphibole-bearing mantle source	Allen et al., 2013
Pleistocene Lori arc	< 5% partial melting of heterogeneous metasomatised, amphibole-bearing peridotite	Neill et al., 2015

Supplementary Item 1- Figures

Figure 1
Exposures of mafic intrusive rocks and metamorphic rocks in the Malayer-Boroujerd Plutonic Complex.

Figure 2
Selected photomicrographs (crossed polarized light) and backscattered electron images of mafic rocks from the MBPC. Four images (a, b, d, e) are taken from Deevsalar et al. (2014). Mineral abbreviations are from Whitney and Evans (2010).

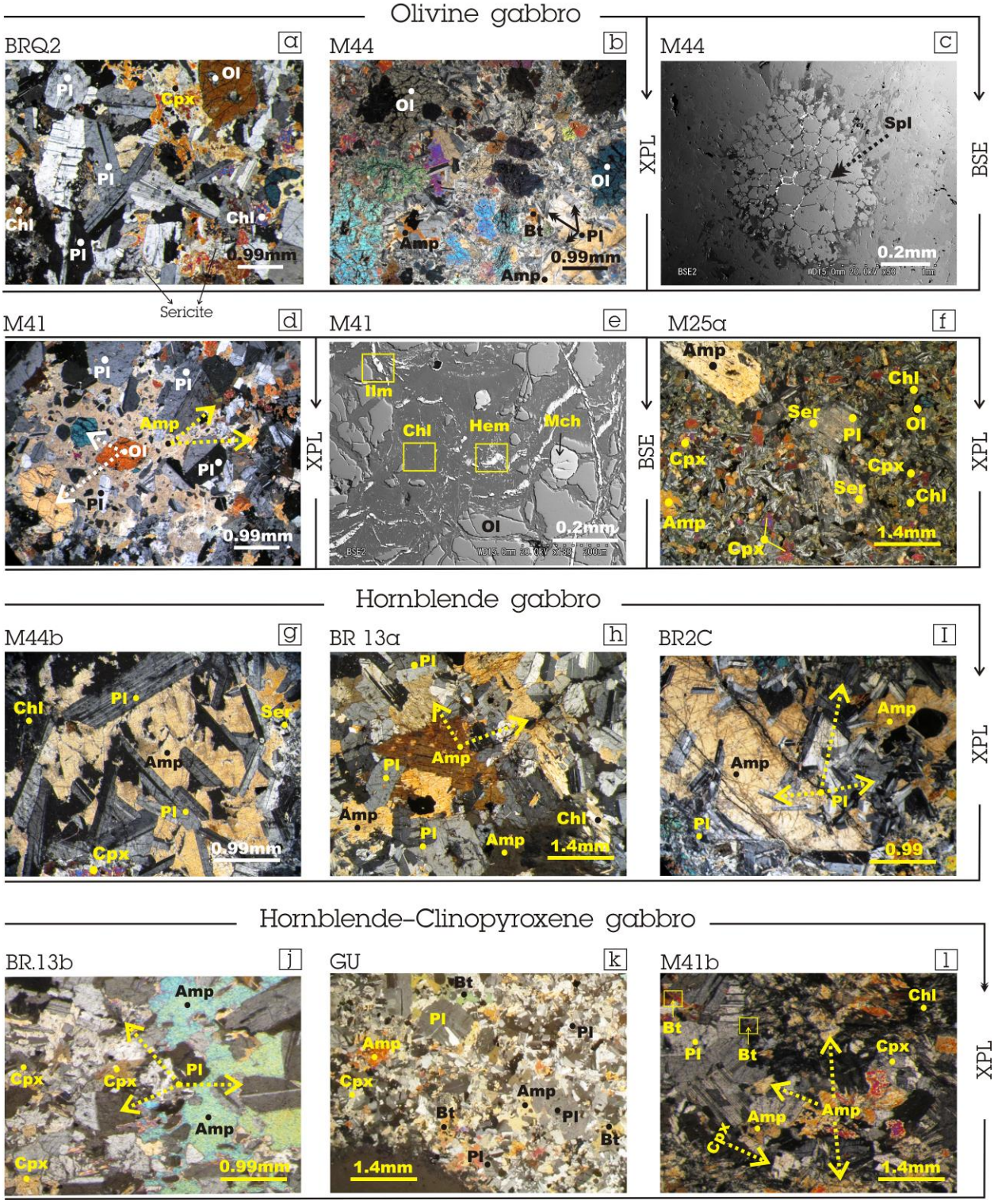

Figure 3
Plots of Nb vs. Ba and Yb vs. Rb for MBPC gabbros.

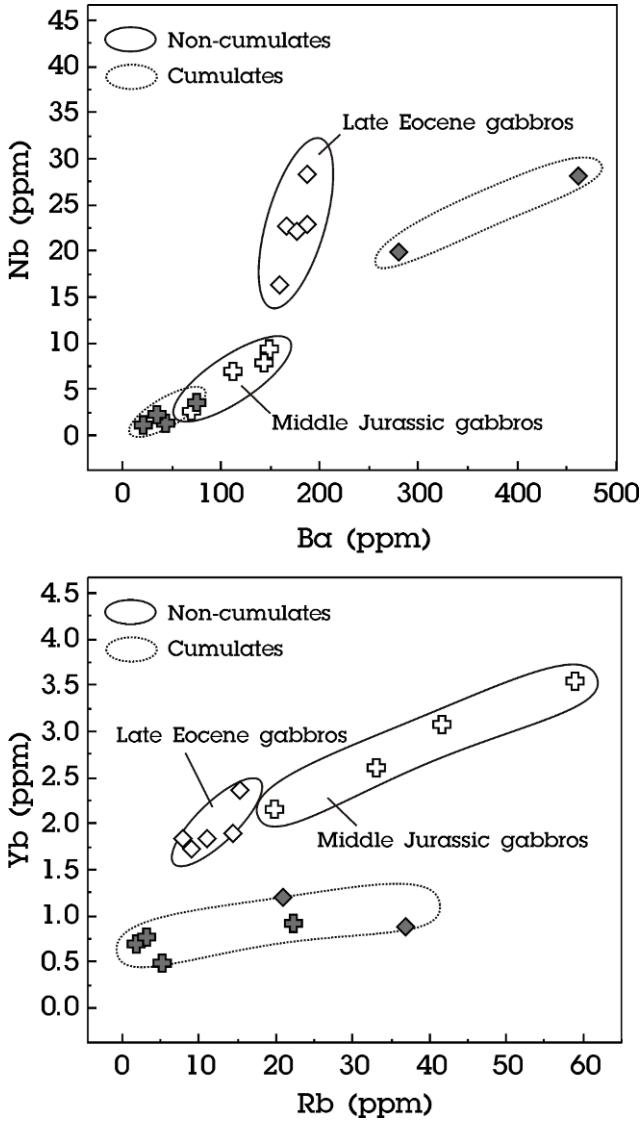

Figure 4
Plots of $^{87}Sr/^{86}Sr$ vs. SiO_2 (a), $^{87}Sr/^{86}Sr$ vs. 1/Sr (b), La/Nb vs. MgO (c) for the MBPC gabbros. The pale gray arrows indicate preferred differentiation trends for each of the ages of MBPC gabbros.

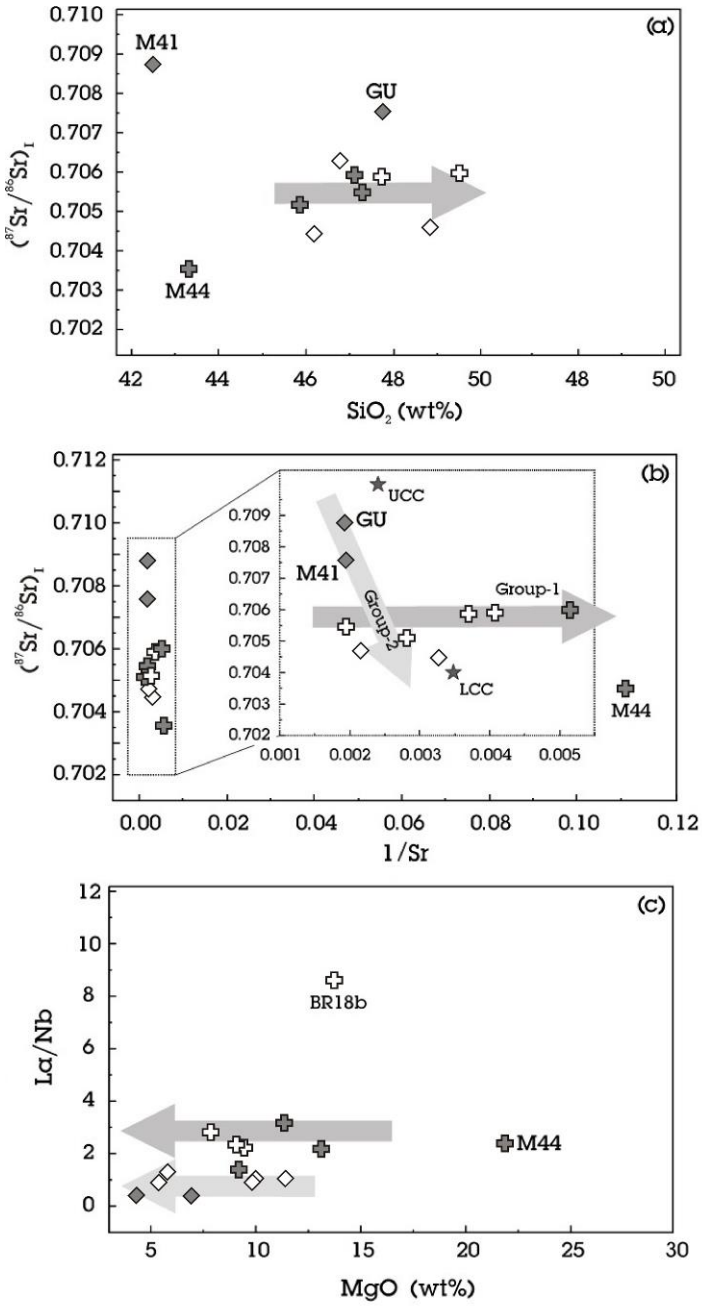

Figure 5
(a) Nb/La vs. Ba/Rb plot (Wang et al., 2004) for the Jurassic low-Ti gabbros. These rocks have Nb/La < 1 suggesting a subduction-metasomatised mantle source. (b) In the Th/Nd vs. Pb/Nd plot the samples lie above the line representing Pb/Th=1 (see text for details).

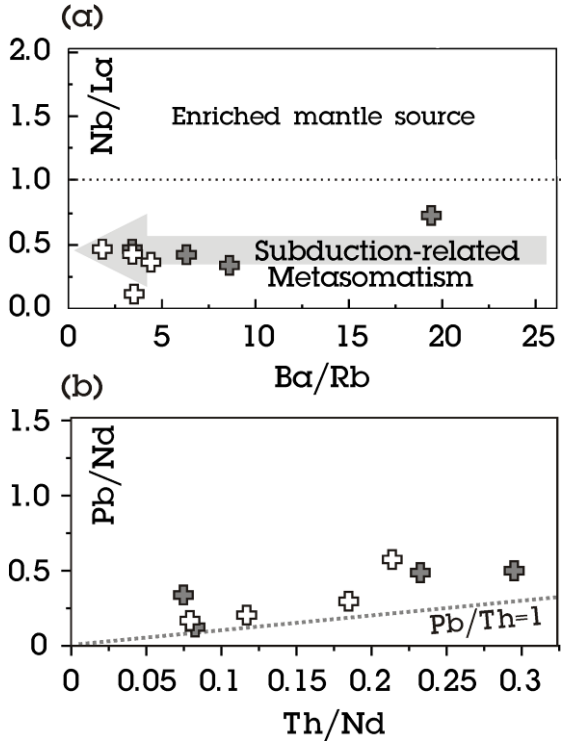

Figure 6
Middle Jurassic non-cumulate gabbros on Harker-style plots.

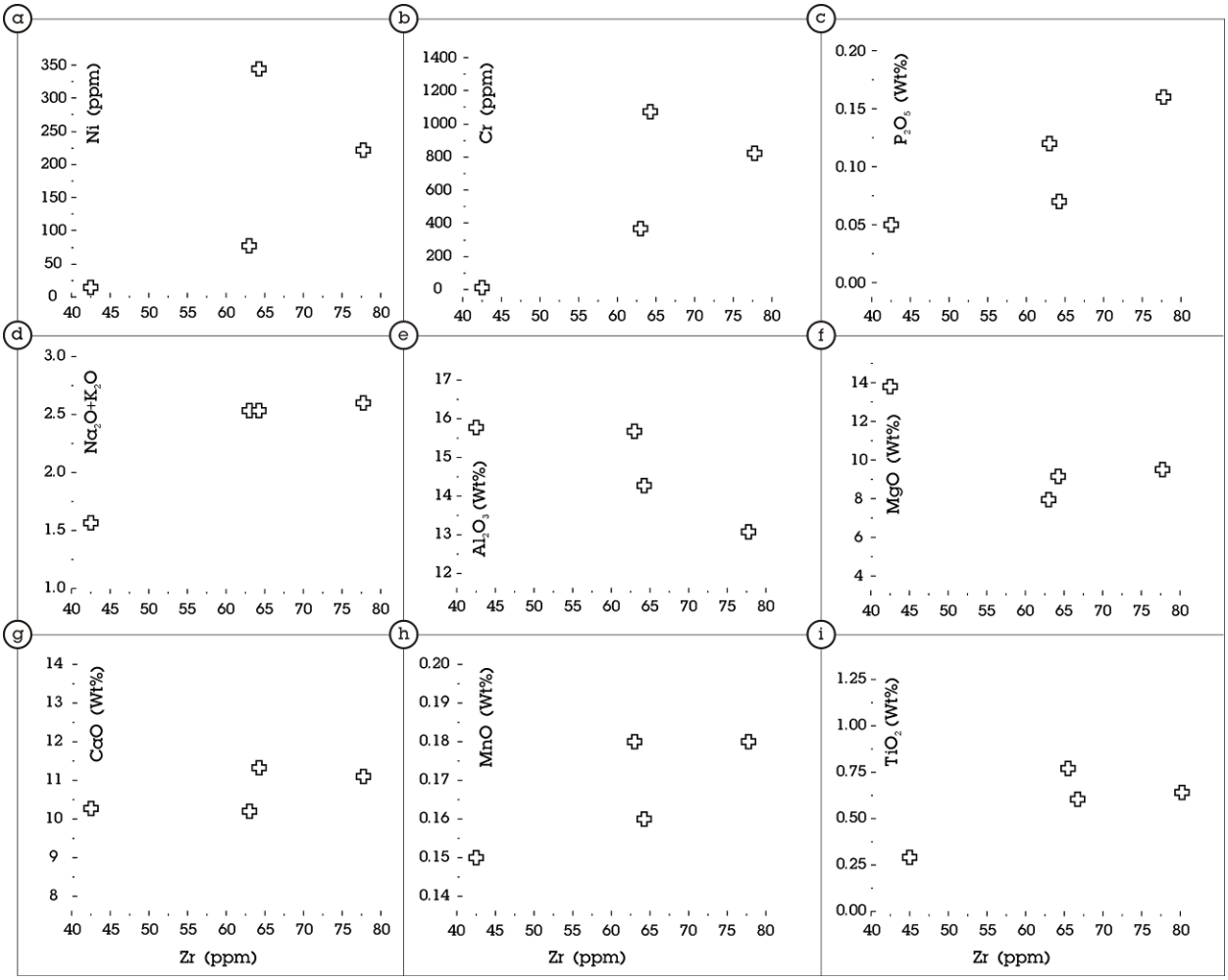

Figure 7
An% and FeO variations in plagioclase traverse profiles for sample BRQ2, as measured by electron microprobe.

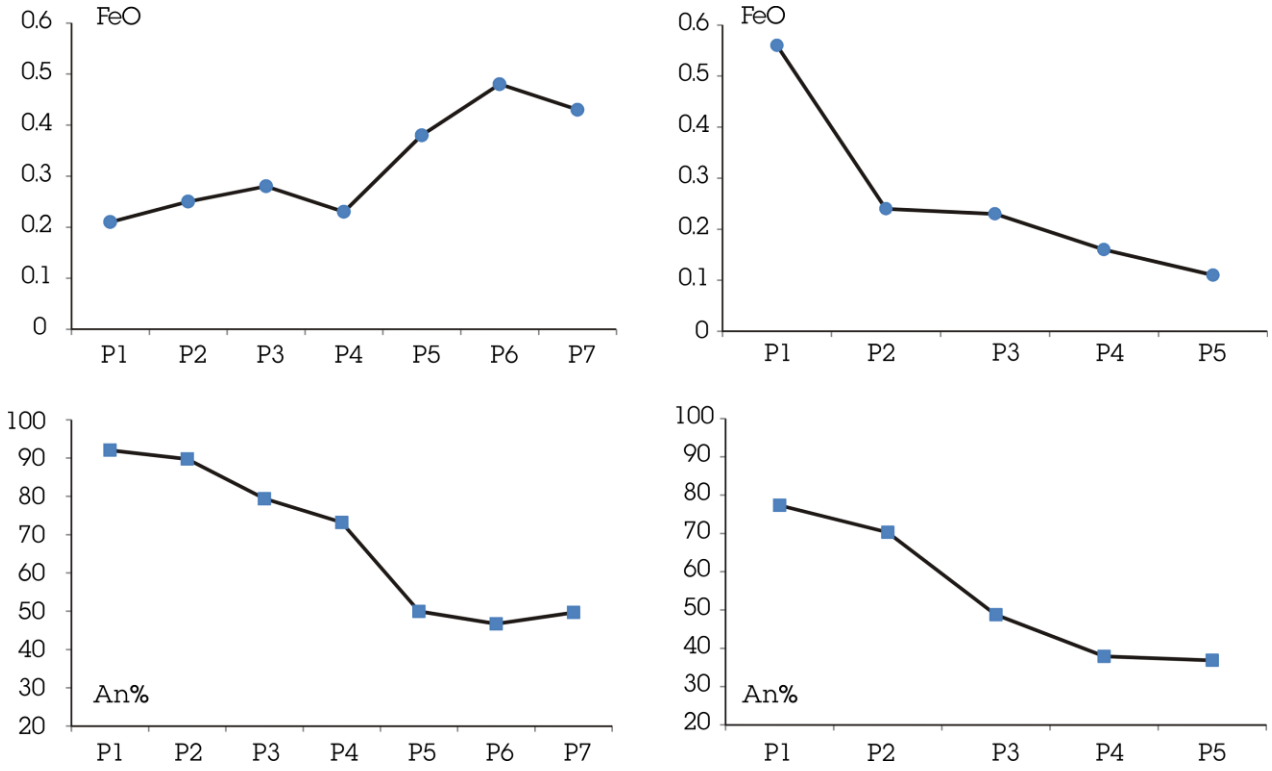

Figure 8
Late Eocene non-cumulate gabbros on Harker-style plots.

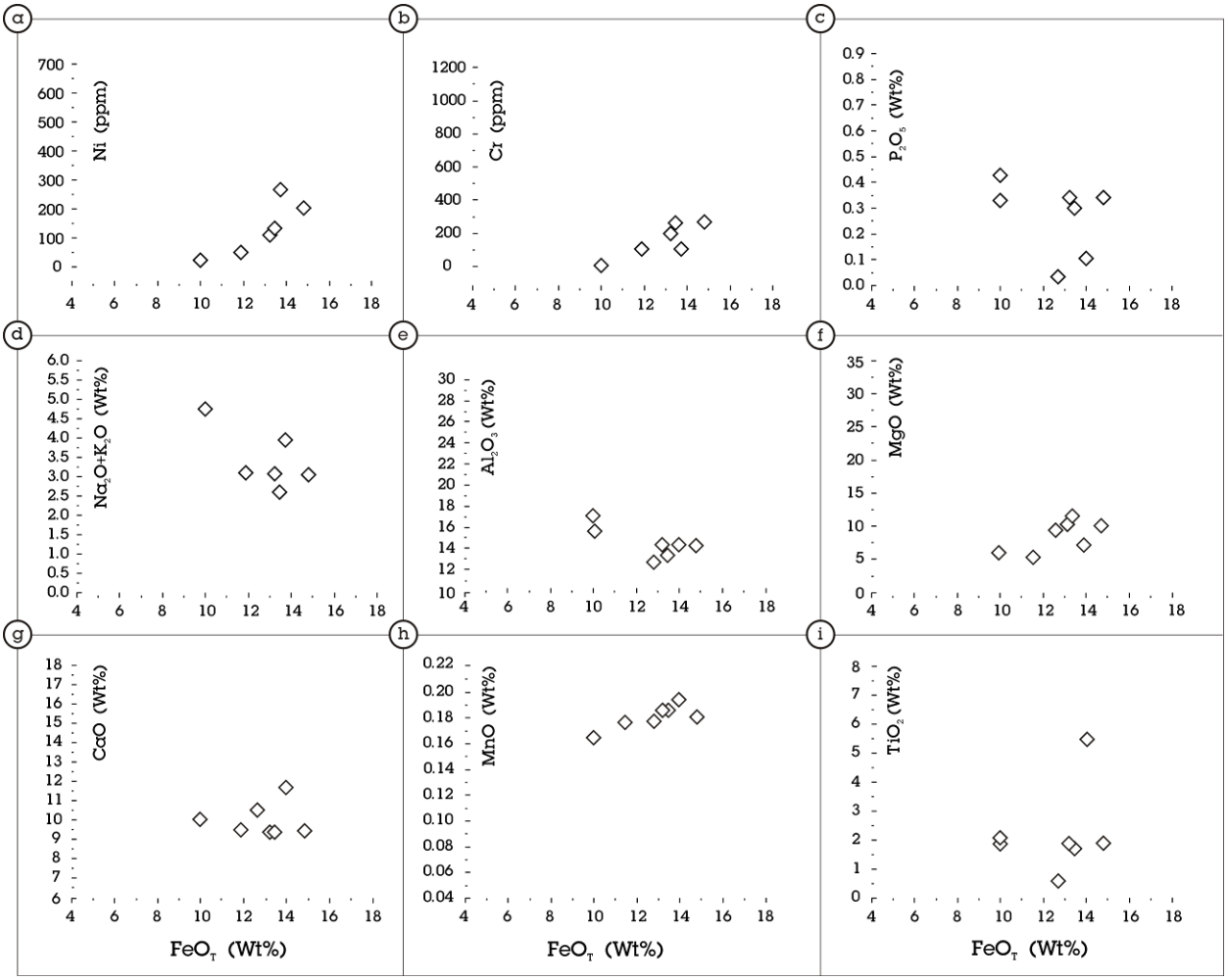

Supplementary Item 2- Analytical methods and procedures

A. Laser ablation zircon U–Pb dating

Two gabbros from the MBPC were chosen for zircon separation using a combination of Wilfley-table washing, heavy liquid separation and magnetic separation. Selected zircon grains from the least magnetic fractions were mounted into a 1-inch disc using epoxy resin. Cathodoluminescence (CL) images were taken using a field emission type EPMA (JEOL JXA-8500F) at the Institute of Earth Sciences (IES), Academia Sinica, Taipei to examine the internal structures of individual zircon grains and select suitable positions for U–Pb analyses. Zircon U–Pb isotopic analyses were performed by using an Agilent 7900 ICP-MS coupled with a Photon Machines (now Teledyne Cetac Technologies) Analyte G2 Excimer laser ablation system equipped at the IES, Academia Sinica, Taipei. A spot size of 30 μm with laser repetition rate of 4 Hz was applied to all analyses; the laser energy density was ~8 J/cm^2. Calibration was performed by using the zircon standard GJ-1 with a $^{207}Pb/^{206}Pb$ age of 608.5 ± 0.4 Ma (Jackson et al., 2004). Zircon standards 91500 and Plešovice (337.1 ± 0.4 Ma; Sláma et al., 2008), were also used for data quality control. Measured U–Th–Pb isotope ratios were calculated by using the GLITTER 4.4 (GEMOC) software and the relative standard deviations of reference values for GJ-1 were set at 2%. The common lead was directly corrected by using the common lead correction function proposed by Anderson (2002), and the weighted mean U–Pb ages and concordia plots were calculated using Isoplot v. 3.0 (Ludwig, 2003). Given that precise age measurements using $^{207}Pb/^{235}U$ and $^{207}Pb/^{206}Pb$ ratios are feasible usually only for Precambrian zircons (cf. Ireland and Williams, 2003), the weighted mean of pooled $^{206}Pb/^{238}U$ ages are taken to indicate the crystallization ages of the samples in this study.

B. Whole rock major and trace elements

Seventy samples of mafic intrusive rocks were collected during mapping and were studied petrographically, with a focus on finding fresh, mineralogically representative examples. Twenty-one representative samples were selected for major and trace element analysis by X-ray fluorescence spectrometry (XRF) and solution inductively coupled plasma mass spectrometry (ICP-MS). XRF analyses were done at Naruto University (Japan) using a Rigaku RIX 2000 instrument with a Rh X-ray source and fused glass discs. Samples were crushed using a jaw crusher and then powdered by hand using an agate mortar and pestle. Finely ground powder was mixed with $Li_2B_4O_7$ at ratio of 1:10 (rock: flux) and analyzed for major elements using fundamental parameter spectrometry methodology. Analytical errors are < 1%. Some samples were analyzed for trace and rare earth elements (REEs) at ACME Labs (Canada) following a lithium metaborate–tetraborate fusion and diluted nitric acid digestion of 0.1 g samples (marked by a star in Table 3). The remaining samples were analyzed for trace elements, including REEs, at the University of the Ryukyus, Japan, using a Thermo Scientific X Series 2 ICP-MS. The analytical procedure is described in Shinjo et al. (2000). Calibration was done in reference to basalt JB-1 (Geological Survey of Japan, GSJ). Replicate analyses of JA-1 (GSJ) and BHVO-2 (United States Geological Survey) — both mafic compositions — typically gave a relative analytical error < 3% and an accuracy of better than 3% for most elements.

C. Whole rock Sr-Nd-Pb isotopic data

The chemical separation of Sr and Nd was performed at the University of the Ryukyus by conventional cation-exchange methods through stepwise washing and eluting of dissolved powder samples by HNO_3 and HCl acids, respectively. All the separation procedures for Sr, Nd and Pb were performed in the clean room of the University of the Ryukyus. Sr was separated by one-step

column separation of 0.1 ml-volume Eichrom Sr-spec resin. Nd was separated by one-step column separation using 1 ml-volume Eichrom Ln-spec resin. Separated Sr and Nd-bearing fractions were dried down and re-dissolved into 0.3 M HNO_3. Instrumental analysis was done using a Thermo Scientific Neptune Plus MC-ICP-MS at the University of the Ryukyus. The standard exponential fractionation law was used for correction of the instrumental mass discrimination of Sr and Nd with internal normalization to $^{86}Sr/^{88}Sr = 0.1194$ and $^{146}Nd/^{144}Nd = 0.7219$. Measured values for NIST SRM 987 and La Jolla Nd standards were 0.710258 ± 19 (2σ, n = 17) and 0.511824 ± 21 (2σ, n = 14), respectively. All measured ratios in this study were normalized to NIST SRM 987 $^{87}Sr/^{86}Sr = 0.71025$ and to La Jolla $^{143}Nd/^{144}Nd = 0.51186$. The normalization of the measured Sr and Nd ratios was based on the mean during the day of standard analysis. In addition, the normalized JNd_{i-1} value was $^{143}Nd/^{144}Nd = 0.512121 \pm 14$ (2σ, n = 8). Chemical separation of Pb was performed using standard HBr-HCl methods with a 0.1 ml-volume Bio-Rad anion exchange resin column. Pb isotope ratios were determined on the Neptune Plus MC-ICP-MS with the Tl addition method to correct for mass fractionation. NIST SRM 981 Pb standard was measured as a calibration reference with the following ratio values: $^{206}Pb/^{204}Pb = 16.9437 \pm 0.0023$, $^{207}Pb/^{204}Pb = 15.5010 \pm 0.0028$ and $^{208}Pb/^{204}Pb = 36.7236 \pm 0.0053$ (2σ, n = 20). Sample Pb isotope ratios were not normalized further.

D. Mineral chemistry

Mineral major element concentrations were determined by EPMA using a JEOL JXA-8800R microprobe at Naruto University, with beam voltage of 15 kV, beam current 15 nA and counting time of 40 s. Further analyses were performed using a Hitachi S3000N scanning electron microscope with EDAX and beam voltage of 20 kV, beam current of 5 nA, and counting times of 100 s at the Department of Geosciences, the University of the Ryukyus.

Supplementary Item 3- Tables

Table 1
LA-ICPMS U–Pb dating for zircon grains separated from the gabbroic intrusion.

	Estimated ratios								Corrected age					
spot	$^{207}Pb/^{206}Pb$	±1σ	$^{207}Pb/^{235}U$	±1σ	$^{206}Pb/^{238}U$	±1σ	$^{208}Pb/^{232}Th$	±1σ	$^{207}Pb/^{235}U$	±1σ	$^{206}Pb/^{238}U$	±1σ	$^{206}Pb/^{238}U$	±1σ
BR18*- Gabbroic intrusion from SE-MBPC														
1	0.04835	0.00132	0.1763	0.00468	0.02645	0.00035	0.00941	0.00039	165	4	168	2	189	8
2	0.0486	0.00099	0.17771	0.00355	0.02653	0.00032	0.00915	0.00035	166	3	169	2	184	7
3	0.05114	0.00112	0.18673	0.004	0.02649	0.00033	0.00912	0.00034	174	3	169	2	184	7
4	0.04997	0.00095	0.17973	0.00337	0.02609	0.00031	0.00893	0.00032	168	3	166	2	180	6
4	0.04959	0.00111	0.17998	0.00396	0.02633	0.00033	0.00934	0.00034	168	3	168	2	188	7
5	0.04963	0.0011	0.1803	0.00391	0.02635	0.00033	0.0091	0.00031	168	3	168	2	183	6
6	0.04993	0.00086	0.18126	0.00313	0.02633	0.00031	0.00923	0.0003	169	3	168	2	186	6
7	0.05064	0.00084	0.18712	0.00311	0.0268	0.00031	0.00927	0.00029	174	3	170	2	187	6
8	0.05138	0.00113	0.18676	0.004	0.02637	0.00032	0.0091	0.00036	174	3	168	2	183	7
9	0.04958	0.00081	0.16917	0.00275	0.02475	0.00028	0.00892	0.00033	159	2	158	2	179	7
10	0.05021	0.00092	0.17825	0.00321	0.02575	0.0003	0.00918	0.00033	167	3	164	2	185	7
12	0.05048	0.00116	0.17998	0.00403	0.02586	0.00032	0.00933	0.00034	168	3	165	2	188	7
13	0.05136	0.00107	0.18202	0.00372	0.02571	0.00031	0.00886	0.0003	170	3	164	2	178	6
14	0.04984	0.00087	0.18108	0.00313	0.02635	0.00031	0.00925	0.0003	169	3	168	2	186	6
15	0.05847	0.00297	0.07152	0.00348	0.00887	0.00016	0.00326	0.00011	70	3	57	1	66	2
16	0.06051	0.00408	0.07325	0.00472	0.00878	0.0002	0.00372	0.00015	72	4	56	1	75	3
17	0.04975	0.00081	0.17959	0.00293	0.02618	0.0003	0.00894	0.00025	168	3	167	2	180	5
18	0.05149	0.00092	0.18719	0.00331	0.02637	0.00031	0.00894	0.00025	174	3	168	2	180	5
19	0.04973	0.00072	0.18019	0.00264	0.02628	0.0003	0.00902	0.00024	168	2	167	2	181	5
20	0.04991	0.00076	0.18263	0.0028	0.02654	0.0003	0.00888	0.00023	170	2	169	2	179	5
21	0.04802	0.00107	0.17782	0.0039	0.02686	0.00033	0.00873	0.00035	166	3	171	2	176	7
22	0.05695	0.00134	0.20813	0.00476	0.02651	0.00034	0.0105	0.0004	192	4	169	2	211	8
23	0.04809	0.001	0.18048	0.00369	0.02722	0.00033	0.00875	0.00032	168	3	173	2	176	6
24	0.04909	0.00083	0.16774	0.00281	0.02478	0.00029	0.00852	0.0003	157	2	158	2	171	6
25	0.05043	0.00091	0.1824	0.00324	0.02623	0.00031	0.00903	0.00031	170	3	167	2	182	6
26	0.04964	0.00093	0.18403	0.0034	0.02689	0.00032	0.00869	0.00028	172	3	171	2	175	6
27	0.04984	0.00112	0.1829	0.00403	0.02662	0.00033	0.00871	0.00029	171	3	169	2	175	6
28	0.04847	0.00108	0.1773	0.00388	0.02653	0.00032	0.00849	0.00027	166	3	169	2	171	5
29	0.04936	0.00075	0.18081	0.00276	0.02657	0.0003	0.00857	0.00024	169	2	169	2	172	5
30	0.04934	0.00074	0.18208	0.00272	0.02676	0.0003	0.00872	0.00024	170	2	170	2	175	5
31	0.05009	0.00095	0.18765	0.00351	0.02717	0.00032	0.00895	0.00025	175	3	173	2	180	5
32	0.04964	0.00088	0.18516	0.00322	0.02705	0.00031	0.00854	0.00022	172	3	172	2	172	4
33	0.04965	0.00097	0.18496	0.00355	0.02702	0.00032	0.00911	0.00036	172	3	172	2	183	7
34	0.04894	0.00113	0.18197	0.00409	0.02697	0.00033	0.00913	0.00036	170	4	172	2	184	7
35	0.04894	0.0012	0.17391	0.00415	0.02578	0.00032	0.0087	0.00033	163	4	164	2	175	7
36	0.06013	0.00128	0.21347	0.00443	0.02575	0.00031	0.00882	0.00031	183	6	163	2	161	2
37	0.04979	0.001	0.18061	0.00355	0.02631	0.00031	0.00891	0.0003	169	3	167	2	179	6
38	0.05056	0.0014	0.18068	0.00486	0.02592	0.00034	0.00904	0.00033	169	4	165	2	182	7
39	0.04969	0.00107	0.18194	0.00383	0.02656	0.00032	0.00881	0.00029	170	3	169	2	177	6
40	0.0498	0.00094	0.18037	0.00336	0.02627	0.00031	0.00864	0.00025	168	3	167	2	174	5
41	0.04952	0.001	0.18323	0.00363	0.02684	0.00032	0.00898	0.00026	171	3	171	2	181	5
42	0.04956	0.00105	0.1823	0.00379	0.02668	0.00032	0.00905	0.00026	170	3	170	2	182	5
* Institute of Earth Sciences (IES), Academia Sinica, Taipei														

	Estimated ratios								Corrected age					
spot	$^{207}Pb/^{206}Pb$	±1σ	$^{207}Pb/^{235}U$	±1σ	$^{206}Pb/^{238}U$	±1σ	$^{208}Pb/^{232}Th$	±1σ	$^{207}Pb/^{235}U$	±1σ	$^{206}Pb/^{238}U$	±1σ	$^{206}Pb/^{238}U$	±1σ
M44b*- Gabbroic intrusion from NW-MBPC														
1	0.04831	0.00073	0.17574	0.00314	0.02599	0.00019	0.00815	0.00025	164	3	165	1	164.1	5
2	0.04933	0.00041	0.18575	0.00475	0.02702	0.00022	0.00836	0.00025	173	5	172	1	168.3	5
3	0.04972	0.00131	0.18392	0.00513	0.02683	0.00031	0.00840	0.00040	171	5	171	2	169.2	8
4	0.04961	0.00091	0.17939	0.00441	0.02644	0.00037	0.00785	0.00035	168	4	168	2	158.1	7
4	0.04983	0.00082	0.18223	0.00663	0.02628	0.00043	0.00832	0.00030	170	7	167	3	167.6	6
5	0.04983	0.00233	0.18634	0.00391	0.02573	0.00022	0.00845	0.00030	174	4	164	1	170.1	6
6	0.04947	0.00135	0.18477	0.00544	0.02645	0.00033	0.00855	0.00025	172	6	168	2	172.1	5
7	0.04957	0.00038	0.17917	0.00356	0.02565	0.00028	0.00835	0.00035	167	4	163	2	168.2	7
8	0.04968	0.00062	0.17828	0.00452	0.02642	0.00036	0.00841	0.00035	167	5	168	2	169.4	7
9	0.04957	0.00443	0.17968	0.00772	0.02668	0.00042	0.00843	0.00035	168	8	170	3	169.8	7
10	0.05255	0.00075	0.18232	0.00512	0.02707	0.00035	0.00800	0.00035	170	5	172	2	161.2	7
12	0.04944	0.00058	0.18219	0.00563	0.02715	0.00034	0.00855	0.00030	170	6	173	2	172.1	6
13	0.04868	0.00052	0.17897	0.00391	0.02639	0.00034	0.00836	0.00025	167	4	168	2	168.3	5
14	0.04973	0.00132	0.18911	0.00430	0.02688	0.00033	0.00870	0.00025	176	4	171	2	175.2	5
15	0.04905	0.00086	0.17088	0.00405	0.02566	0.00062	0.00813	0.00025	160	4	163	4	163.8	5
16	0.05044	0.00042	0.17794	0.00419	0.02643	0.00035	0.00818	0.00040	166	4	168	2	164.8	8
17	0.04933	0.00122	0.18333	0.00377	0.02719	0.00025	0.00846	0.00025	171	4	173	2	170.3	5
18	0.04971	0.00081	0.17730	0.00628	0.02623	0.00044	0.00826	0.00030	166	6	167	3	166.4	6
19	0.04952	0.00411	0.18208	0.00483	0.02648	0.00035	0.00822	0.00035	170	5	168	2	165.6	7
20	0.05051	0.00085	0.18765	0.00481	0.02678	0.00039	0.00865	0.00030	175	5	170	3	174.2	6
21	0.04961	0.00032	0.18516	0.00592	0.02718	0.00037	0.00858	0.00035	172	6	173	2	172.8	7
22	0.04938	0.00033	0.18061	0.00713	0.02631	0.00036	0.00837	0.00020	169	7	167	2	168.6	4
23	0.04891	0.00045	0.18068	0.00577	0.02658	0.00034	0.00843	0.00035	169	6	169	2	169.7	7
24	0.04946	0.00101	0.18194	0.00498	0.02632	0.00035	0.00841	0.00040	170	5	167	2	169.4	8
25	0.05164	0.00061	0.18693	0.00960	0.02746	0.00077	0.00868	0.00035	174	10	175	5	174.7	7
26	0.04977	0.00088	0.18714	0.00664	0.02705	0.00040	0.00867	0.00040	174	7	172	3	174.5	8
27	0.04958	0.00173	0.18632	0.00519	0.02697	0.00036	0.00861	0.00035	173	5	172	2	173.3	7
28	0.04972	0.00175	0.18698	0.00655	0.02712	0.00044	0.00858	0.00020	174	7	172	3	172.8	4
29	0.05019	0.00078	0.18675	0.00521	0.02697	0.00022	0.00861	0.00025	174	5	172	1	173.3	5
30	0.04962	0.00068	0.18299	0.00483	0.02692	0.00021	0.00851	0.00025	171	5	171	1	171.4	5
31	0.04967	0.00203	0.18646	0.00611	0.02755	0.00042	0.00773	0.00025	174	6	175	3	155.7	5
32	0.04990	0.00073	0.18639	0.00519	0.02746	0.00032	0.00872	0.00030	174	5	175	2	175.6	6
33	0.04850	0.00058	0.18674	0.00734	0.02676	0.00058	0.00845	0.00030	174	7	170	4	170.1	6
34	0.04975	0.00151	0.18709	0.00483	0.02722	0.00036	0.00868	0.00035	174	5	173	2	174.8	7
35	0.04971	0.00132	0.18681	0.00717	0.02698	0.00045	0.00863	0.00035	174	7	172	3	173.8	7
36	0.04881	0.00089	0.18671	0.00316	0.02745	0.00017	0.00867	0.00035	174	3	175	1	174.6	7
37	0.04969	0.00062	0.18383	0.00456	0.02761	0.00036	0.00841	0.00030	171	5	176	2	169.3	6
38	0.04930	0.00166	0.18691	0.00540	0.02767	0.00043	0.00866	0.00035	174	5	176	3	174.4	7
39	0.04939	0.00087	0.18664	0.00434	0.02699	0.00031	0.00863	0.00040	174	4	172	2	173.7	8
40	0.05147	0.00051	0.18214	0.00731	0.02685	0.00035	0.00846	0.00040	170	7	171	2	170.3	8
41	0.05046	0.00093	0.18112	0.00688	0.02686	0.00025	0.00848	0.00040	169	7	171	2	170.7	8
42	0.04958	0.00038	0.18454	0.00267	0.02692	0.00134	0.00857	0.00035	172	3	171	9	172.6	7

	Estimated ratios								Corrected age					
spot	$^{207}Pb/^{206}Pb$	±1σ	$^{207}Pb/^{235}U$	±1σ	$^{206}Pb/^{238}U$	±1σ	$^{208}Pb/^{232}Th$	±1σ	$^{207}Pb/^{235}U$	±1σ	$^{206}Pb/^{238}U$	±1σ	$^{206}Pb/^{238}U$	±1σ
M44b*- Gabbroic intrusion from NW-MBPC														
43	0.04947	0.00177	0.18155	0.00470	0.02633	0.00042	0.00838	0.00030	169	5	168	3	168.8	6
44	0.04964	0.00069	0.18109	0.00818	0.02612	0.00027	0.00841	0.00030	169	8	166	2	169.4	6
45	0.04837	0.00088	0.17787	0.00708	0.02671	0.00059	0.00837	0.00030	166	7	170	4	168.5	6
46	0.05243	0.00143	0.17996	0.00390	0.02638	0.00042	0.00832	0.00030	168	4	168	3	167.6	6
47	0.04967	0.00092	0.17546	0.00233	0.02667	0.00038	0.00840	0.00035	164	2	170	2	169.2	7
48	0.04954	0.00078	0.18614	0.00317	0.02748	0.00031	0.00868	0.00025	173	3	175	2	174.7	5
49	0.04963	0.00047	0.18588	0.00492	0.02756	0.00038	0.00872	0.00035	173	5	175	2	175.5	7
50	0.05048	0.00333	0.18366	0.00395	0.02671	0.00032	0.00853	0.00045	171	4	170	2	171.8	9
51	0.04914	0.00115	0.18449	0.00461	0.02643	0.00032	0.00837	0.00045	172	5	168	2	168.6	9
52	0.04997	0.00048	0.17610	0.00810	0.02551	0.00057	0.00821	0.00035	165	8	162	4	165.4	7
53	0.04960	0.00042	0.18241	0.00940	0.02659	0.00103	0.00848	0.00035	170	10	169	7	170.8	7
54	0.05033	0.00053	0.18387	0.00706	0.02661	0.00042	0.00853	0.00025	171	7	169	3	171.8	5
55	0.05140	0.00251	0.18229	0.00755	0.02693	0.00030	0.00850	0.00035	170	8	171	2	171.2	7
56	0.04952	0.00078	0.18339	0.00516	0.02749	0.00046	0.00866	0.00025	171	5	175	3	174.3	5
57	0.04954	0.00042	0.18174	0.00538	0.02633	0.00033	0.00840	0.00035	170	5	168	2	169.1	7
58	0.04962	0.00166	0.17409	0.00917	0.02535	0.00059	0.00788	0.00035	163	9	161	4	158.8	7
59	0.05035	0.00081	0.17719	0.00453	0.02587	0.00025	0.00828	0.00025	166	5	165	2	166.7	5
60	0.04989	0.00055	0.18095	0.00557	0.02671	0.00032	0.00843	0.00025	169	6	170	2	169.8	5
61	0.05013	0.00188	0.18143	0.00714	0.02645	0.00047	0.00862	0.00030	169	7	168	3	173.6	6
62	0.04945	0.00056	0.18268	0.00519	0.02662	0.00031	0.00846	0.00035	170	5	169	2	170.3	7
63	0.05115	0.00168	0.18345	0.00815	0.02658	0.00044	0.00851	0.00035	171	8	169	3	171.4	7
64	0.05471	0.00175	0.17928	0.00831	0.02631	0.00037	0.00830	0.00040	167	8	167	2	167.2	8
65	0.04954	0.00058	0.18768	0.00715	0.02692	0.00047	0.00868	0.00035	175	7	171	3	174.8	7
66	0.05035	0.00032	0.18092	0.00739	0.02694	0.00052	0.00856	0.00045	169	7	171	3	172.3	9
67	0.04977	0.00102	0.18812	0.00547	0.02722	0.00038	0.00874	0.00035	175	6	173	2	175.9	7
68	0.04882	0.00095	0.18111	0.00853	0.02648	0.00051	0.00840	0.00035	169	9	168	3	169.1	7
69	0.04887	0.00044	0.17418	0.00491	0.02583	0.00038	0.00817	0.00025	163	5	164	2	164.6	5
70	0.05292	0.00032	0.17216	0.00479	0.02529	0.00025	0.00802	0.00025	161	5	161	2	161.5	5
71	0.04977	0.00182	0.17195	0.00603	0.02571	0.00049	0.00813	0.00025	161	6	164	3	163.8	5
*ETHz, Department of Earth Sciences Institute of Geochemistry and Petrology														

Table 1
Continued

	Estimated ratios								Corrected age					
spot	$^{207}Pb/^{206}Pb$	±1σ	$^{207}Pb/^{235}U$	±1σ	$^{206}Pb/^{238}U$	±1σ	$^{208}Pb/^{232}Th$	±1σ	$^{207}Pb/^{235}U$	±1σ	$^{206}Pb/^{238}U$	±1σ	$^{208}U/^{232}Th$	±1σ
BN07b- Gabbroic intrusion from SE-MBPC														
1	0.05171	0.00154	0.0392	0.00113	0.0055	0.00007	0.0019	0.00005	39	1	35.4	0.4	38	1
2	0.04541	0.00225	0.03755	0.0018	0.006	0.0001	0.00204	0.00006	37	2	38.6	0.6	41	1
3	0.07431	0.001	1.80196	0.02452	0.1759	0.00193	0.05481	0.00147	1046	9	1045	11	1079	28
4	0.04953	0.00167	0.05729	0.00186	0.00839	0.00012	0.00294	0.00009	57	2	53.9	0.8	59	2
5	0.04907	0.00147	0.05744	0.00167	0.00849	0.00011	0.00296	0.00009	57	2	54.5	0.7	60	2
6	0.1621	0.00229	10.28492	0.14626	0.46021	0.00523	0.13663	0.00407	2429	19	2427	22	2427	24
7	0.04784	0.00419	0.05526	0.00472	0.00838	0.00019	0.00327	0.00015	55	5	54	1	66	3
8	0.0514	0.00428	0.06372	0.00514	0.00899	0.00021	0.00298	0.00012	63	5	58	1	60	2
9	0.06726	0.00098	1.22256	0.01791	0.13185	0.00148	0.04223	0.00113	811	8	798	8	836	22
10	0.08976	0.00131	3.00541	0.04385	0.24287	0.00275	0.07694	0.00214	1409	11	1402	14	1498	40
11	0.0559	0.00357	0.10798	0.00667	0.01401	0.00028	0.00496	0.00018	86	3	89	1	92	3
12	0.06211	0.00432	0.1207	0.00808	0.0141	0.00031	0.0054	0.00021	116	7	90	2	109	4
13	0.05547	0.00249	0.03351	0.00145	0.00438	0.00007	0.00177	0.00007	27.6	1	27.8	0.4	28	1
14	0.05137	0.00149	0.05065	0.00142	0.00715	0.0001	0.00235	0.00008	50	1	45.9	0.6	47	2
15	0.08969	0.00412	0.08698	0.00374	0.00703	0.00014	0.00299	0.00011	42	1	42.7	0.7	46	2
16	0.0503	0.0034	0.04849	0.00318	0.00699	0.00014	0.00233	0.0001	48	3	44.9	0.9	47	2
17	0.0571	0.004	0.05357	0.00362	0.0068	0.00015	0.00227	0.0001	46	4	43.3	0.9	43	0.9
* Institute of Earth Sciences (IES), Academia Sinica, Taipei														

	Estimated ratios								Corrected age					
spot	$^{207}Pb/^{206}Pb$	±1σ	$^{207}Pb/^{235}U$	±1σ	$^{206}Pb/^{238}U$	±1σ	$^{208}Pb/^{232}Th$	±1σ	$^{207}Pb/^{235}U$	±1σ	$^{206}Pb/^{238}U$	±1σ	$^{208}U/^{232}Th$	±1σ
M25a- Gabbroic intrusions from NW-MBPC														
1	0.04852	0.00359	0.03937	0.00271	0.00603	0.00009	0.00189	0.00010	39.2	3	38.8	1	38.2	2
2	0.04832	0.00224	0.03751	0.00354	0.00601	0.00018	0.00201	0.00010	37.4	4	38.6	1	40.6	2
3	0.04941	0.00559	0.03537	0.00272	0.00503	0.00019	0.00161	0.00010	35.3	3	32.3	1	32.6	2
4	0.04848	0.00445	0.03251	0.00451	0.00523	0.00028	0.00161	0.00005	32.5	5	33.6	2	32.5	1
5	0.04856	0.00185	0.03486	0.00359	0.00511	0.00012	0.00159	0.00010	34.8	4	32.9	1	32.2	2
6	0.04949	0.00245	0.03486	0.00159	0.00571	0.00011	0.00173	0.00005	34.8	2	36.7	1	34.9	1
7	0.04916	0.00344	0.03526	0.00364	0.00553	0.00031	0.00175	0.00005	35.2	4	35.6	2	35.4	1
8	0.04776	0.00434	0.03642	0.00761	0.00565	0.00033	0.00178	0.00004	36.3	8	36.3	2	36.1	1
9	0.04820	0.00119	0.04242	0.00161	0.00715	0.00014	0.00224	0.00010	42.2	2	45.9	1	45.3	2
10	0.04788	0.00215	0.04162	0.00122	0.00635	0.00013	0.00204	0.00010	41.4	1	40.8	1	41.3	2
11	0.05015	0.00128	0.04802	0.00141	0.00735	0.00015	0.00234	0.00010	47.6	1	47.2	1	47.2	2
12	0.04872	0.00316	0.05102	0.00335	0.00785	0.00014	0.00245	0.00005	50.5	3	50.4	1	49.4	1
13	0.04896	0.00597	0.03202	0.00535	0.00496	0.00019	0.00161	0.00005	32.0	5	31.9	1	32.4	1
14	0.21371	0.00825	2.85451	0.01488	0.25224	0.00171	0.07512	0.00163	1370	15	1450	11	1465	33
*ETHz, Department of Earth Sciences Institute of Geochemistry and Petrology														

Table 2
Amphibole and clinopyroxene chemical composition for the MBPC gabbros.

(A)	Clinopyroxene				
	Middle Jurassic Low-Ti		Late Eocene High-Ti		
Sample name	M41b		M41	BR13b	
	P1	P2	P1	P1	P2
	(Wt. %)				
SiO_2	53.21	53.48	49.31	47.55	48.16
$A1_2O_3$	1.06	1.57	5.89	6.43	4.55
TiO_2	0.06	0.17	1.96	2.2	2.01
Cr_2O_3	0.03	0.16	0.04	0.03	0.05
FeO	17.41	13.76	7.14	7.7	8.1
MnO	0.35	0.31	0.29	0.19	0.2
MgO	25.89	28.04	13.31	13.82	15.22
CaO	1.04	1.57	21.32	21.31	20.12
Na_2O	0.005	0.03	0.41	0.2	0.32
K_2O	0	0.02	0.27	0.18	0.28
NiO	0.05	0.04	0	0	0
Total	99.10	99.15	99.94	99.61	99.01
	(apfu)				
Si	1.97	1.957	1.897	1.849	1.866
Al	0.02	0.034	0.134	0.147	0.104
Ti	0.002	0.005	0.057	0.064	0.059
Cr	0.00	0.002	0.001	0.000	0.001
Fe	0.54	0.421	0.230	0.250	0.263
Mn	0.01	0.010	0.009	0.006	0.007
Mg	1.43	1.529	0.763	0.801	0.879
Ca	0.04	0.062	0.879	0.888	0.835
Na	0.00	0.001	0.015	0.008	0.012
K	0.00	0.000	0.007	0.004	0.007
Ni	0.002	0.001	0.000	0.000	0.000
***Mg#**	0.73	0.78	0.77	0.76	0.77
*$Mg^{\#} = Mg/(Mg+Fe^{+2})$					

(B)	Amphibole					
	Middle Jurassic Low-Ti		Late Eocene High-Ti			
Sample name	M07		BN07b		BR13b	
	P1	P2	P1	P2	P1	P2
	(Wt. %)					
SiO_2	48.78	48.02	38.21	37.39	38.52	38.76
TiO_2	0.62	0.21	6.40	6.35	5.66	5.32
$A1_2O_3$	8.86	8.78	12.05	13.88	13.76	13.91
FeO	12.31	14.30	15.27	16.70	16.03	15.11
MnO	0.20	0.31	0.30	0.26	0.32	0.15
MgO	16.02	14.95	10.82	10.57	11.30	11.24
CaO	11.51	11.03	11.96	11.55	11.04	11.17
Na_2O	0.35	0.90	2.16	1.12	1.02	0.85
K_2O	0.13	0.28	0.76	0.75	0.89	0.95
Cr_2O_3	0.23	0.34	0.20	0.03	0.00	0.00
NiO	0.00	0.00	0.00	0.00	0.00	0.00
Total	99.01	99.12	98.13	98.60	98.54	97.46
	(apfu)					
Si	6.73	6.69	5.74	5.49	5.60	5.68
Al^{iv}	1.27	1.31	2.13	2.40	2.35	2.32
Al^{vi}	0.17	0.13	0.00	0.00	0.00	0.09
Ti	0.06	0.02	0.72	0.70	0.62	0.59
Cr	0.03	0.04	0.02	0.00	0.00	0.00
Fe^{3+}	1.42	1.51	0.29	1.10	1.30	1.13
Fe^{2+}	0.00	0.16	1.63	0.95	0.65	0.72
Mn	0.02	0.04	0.04	0.03	0.04	0.02
Mg	3.30	3.11	2.42	2.31	2.45	2.46
Ni	0.00	0.00	0.00	0.00	0.00	0.00
Ca	1.70	1.65	1.92	1.82	1.72	1.75
Na	0.09	0.24	0.63	0.32	0.32	0.24
K	0.02	0.05	0.14	0.15	0.17	0.18
OH*	2.00	2.00	2.00	2.00	2.00	2.00
Total	16.82	16.94	17.70	17.28	17.20	17.17
$Mg^{\#}$	1.00	0.95	0.60	0.71	0.79	0.77
Ca/Ca+Na	0.95	0.87	0.75	0.85	0.84	0.88
Amphibole Name	ferri-magnesio-hornblende	ferri-magnesio-hornblende	subsilicic kaersutite	ferri-subsilicic kaersutite		

* $Mg^{\#} = Mg/(Mg+Fe^{+2})$
* Classification base on Leake, 1978; Leake et al. 2004

(C)	Plagioclase											
	Sample BRQ2											
	Pl-1							Pl-2				
	Core				Rim			Core		Rim		
	P1	P2	P3	P4	P5	P6	P7	P1	P2	P3	P4	P5
	(Wt. %)											
SiO_2	49.22	45.08	49.94	53.41	52.64	52.33	51.93	51.92	53.69	52.01	52.13	51.15
$A1_2O_3$	29.78	27.49	30.13	30.34	27.31	29.38	28.12	30.89	29.58	28.33	29.18	29.67
TiO_2	0	0	0	0	0	0	0	0.17	0	0	0	0
Cr_2O_3	0	0	0	0	0	0	0	0.11	0	0	0	0
FeO	0.21	0.25	0.28	0.23	0.38	0.48	0.43	0.56	0.24	0.23	0.16	0.11
MnO	0.04	0.16	0	0	0.03	0.04	0.07	0.1	0	0.02	0.08	0.05
MgO	0.13	0.13	0.52	0	0.06	0.08	0.07	0.34	0	0.08	0.08	0
CaO	17.31	23.58	13.98	12.22	8.01	7.88	8.13	13.35	11.6	8.31	6.13	6.01
Na_2O	1.61	2.94	3.93	4.85	8.85	9.91	9.05	4.24	5.33	9.61	11.05	11.3
K_2O	0.07	0.06	0.14	0.16	0.03	0.05	0.1	0.14	0.15	0.07	0.1	0.14
NiO	0.1	0.2	0	0	0	0.1	0	0	0	0.1	0	0
Total	98.47	99.89	98.92	101.21	97.31	100.25	97.9	101.82	100.59	98.76	98.91	98.43
	(apfu)											
Si	2.72	2.47	2.77	2.86	2.95	2.9	2.92	2.79	2.89	2.91	2.93	2.91
Al	0.97	0.89	0.98	0.96	0.9	0.96	0.93	0.98	0.94	0.93	0.97	0.99
Ti	0	0	0	0	0	0	0	0.01	0	0	0	0
Cr	0	0	0	0	0	0	0	0	0	0	0	0
Fe	0.01	0.01	0.01	0.01	0.01	0.01	0.02	0.03	0.01	0.01	0.01	0.01
Mn	0	0.01	0	0	0	0	0	0	0	0	0	0
Mg	0.01	0.01	0.04	0	0.01	0.01	0.01	0.03	0	0.01	0.01	0
Ca	1.03	1.39	0.83	0.7	0.48	0.47	0.49	0.77	0.67	0.5	0.37	0.37
Na	0.09	0.16	0.21	0.25	0.48	0.53	0.49	0.22	0.28	0.52	0.6	0.62
K	0	0	0	0.01	0	0	0	0	0.01	0	0	0.01
Ni	0	0.01	0	0	0	0	0	0	0	0	0	0
***An%**	92.03	89.75	79.35	73.16	49.95	46.69	49.64	77.3	70.25	48.74	37.87	36.83
*An% = Ca/(Ca+Na+K)												

Table 3

Initial modal proportions of the starting composition used in mantle melting models.

	olivine	orthopyroxene	clinopyroxene	garnet	amphibole	phlogopite	spinel
amphibole-bearing garnet-spinel Lherzolite							
Source mode	0.5	0.22	0.16	0.07	0.02	0	0.03
Reaction mode	0.15	0.15	0.2	0.2	0.1	0	0.2
garnet-spinel Lherzolite							
Source mode-I	0.55	0.255	0.115	0.06	0	0	0.02
Reaction mode	0.15	0.15	0.3	0.2	0	0	0.2
garnet-spinel Lherzolite							
Source mode-II	0.6	0.225	0.11	0.045	0	0	0.02
Reaction mode	0.15	0.15	0.2	0.3	0	0	0.2

Some Kd values of selected trace elements are from for the melting model are from Ersoy 2010 and references cited in this paper. Others from Okamoto 1979; Lemarchfand et al., 1987; Kelemen et al, 1993 in Johnson 1998; Reid 1983; Zack and Brumm 1998; Glazer et al., 1999.

Source mode and reaction mode are taken from Tang et al., 2006; Khalaf et al., 2010.

Table 4
Partition coefficient of mineral phases employed in melting and fractional crystallization modes.

	Partition coefficient								
	References								
	(1)				(2)	(3)	(4)	(5)	(6)
Elements	Opx	Grt	Ol	Pl	Cpx	Am	Spl	Ilm	Apt
La	0.002	0.01	0.0006	0.27	0.0435	0.2	0.001	0.1	2.8
Ce	0.003	0.021	0.0005	0.2	0.0843	0.35	0.0006	0.3	3
Pr	0.0048	0.054	0.0008	0.17	0.124	0.35	0.0006	0.01	4
Nd	0.0048	0.087	0.0010	0.14	0.173	0.65	0.0006	0.01	5
Sm	0.01	0.217	0.0013	0.11	0.283	0.85	0.0006	0.01	6
Eu	0.013	0.32	0.0016	0.73	0.312	0.8	0.0006	0.15	6
Gd	0.016	0.498	0.0015	0.066	0.336	0.95	0.0006	0.27	6
Tb	0.019	0.75	0.0015	0.06	0.364	1.2	0.0006	0.2	6
Dy	0.022	1.06	0.0017	0.055	0.363	1.3	0.0006	0.17	5.4
Ho	0.026	1.53	0.0016	0.048	0.378	1	0.0006	0.2	5
Er	0.03	2	0.0015	0.041	0.351	0.9	0.0006	0.001	4
Yb	0.049	4.3	0.0015	0.031	0.313	0.9	0.0045	0.048	2.6
Lu	0.06	5.5	0.0015	0.025	0.265	0.8	0.0006	0.11	2.2

(1) McKenzie and O'Nions, 1991
(2) Foley et al., 1996
(3) Fujimaki et al., 1984
(4) Kelemen et al, 1993 in Johanson 1998
(5) Ewart and Griffin, 1994
(6) Watson and Green, 1981

Table 5

The results of melting, mixing and fractional crystallization model calculations for Middle Jurassic Low-Ti gabbros.

	Mantle wedge				High crustal level	
	Source	Mixing		NMBM*4	Fractional crystallization	
	PM*1	A1*2: 0.55F/0.45M	EM*3: 80% PM + 20% A1	$F_{melting}$ = 0.15*5	Residual melt*6	Residual solid*7
					F= 0.45	F= 0.35
Rb	0.63	71.04	4.16	27.28	54.95	8.83
Ba	6.99	1019.20	57.60	379.26	722.95	211.27
Th	0.09	5.10	0.34	2.22	4.91	0.81
U	0.02	1.11	0.08	0.50	1.10	0.03
Nb	0.71	4.64	0.91	6.01	13.08	0.39
K	249.98	21038.38	1289.40	8164.83	12407.93	6288.82
La	0.69	16.72	1.49	9.44	18.11	5.76
Ce	1.77	34.55	3.41	20.76	39.35	12.01
Pr	0.28	1.64	0.34	2.01	3.84	1.31
Sr	21.10	473.80	43.73	264.40	514.15	137.15
P	94.98	486.66	114.56	654.94	1438.91	10.36
Nd	1.35	15.51	2.06	11.41	20.49	6.33
Zr	11.20	254.15	23.35	129.59	273.12	24.20
Sm	0.44	2.79	0.56	2.77	4.78	1.84
Eu	0.17	0.61	0.19	0.90	1.26	0.87
Ti	1300.24	1922.51	1331.36	5682.87	10353.85	2710.66
Dy	0.74	1.60	0.78	3.11	4.88	1.78
Y	4.55	8.81	4.77	15.10	29.65	7.36
Yb	0.49	0.72	0.50	1.34	2.40	0.50
Lu	0.07	0.10	0.08	0.18	0.32	0.06

*1 PM: primitive mantle composition (Sun and McDonough, 1989)

*2 Subduction sediment-derived fluids/melts. The parameters used in modeling are: normalizing values from Sun and McDonough 1989, Bulk subducted sediment composition (BOS) are from Plank and Langmuir 1998, sediment fluid partition coefficients (DSF) from Johnson and Plank (1999). Sediment melt (SM) calculated by 5% modal fractional melting of bulk subducted sediment, sediment fluids (SF) composition calculated using BOS and DSF($C_{BOS/DSF}$).

*3 Middle Jurassic Enriched Mantle

*4 NMBM: Non-Modal Batch Melting

*5 15% partial melting of metasomatised garnet-spinel Lherzolite (Supplementary Item 3, Table 1)

*6 Residual melt of fractional crystallization of 0.2 Ol + 0.05 Cpx + 0.45 Pl + 0.3 Am from B_1-magma

*7 Residual solid of Fractional crystallization of 0.05 Cpx + 0.75 Pl + 0.2 Am ± 0.02 Apt from B_1-magma

Table 6
The results of melting, mixing and fractional crystallization model calculations for Late Eocene high-Ti gabbros.

	Source region				High crustal level
	Source	NMBM*2		Mixing*5	Fractional crystallization
		Mode-I	Mode-II		
	PM*1 (GS Lhz)	$F_{melting}$ = 0.05*3	$F_{melting}$ = 0.15*4	60% $Melt_{(5\%)}$ + 40% $Melt_{(15\%)}$	Residual melt*6 F= 0.55
Rb	0.63	12.39	5.60	7.48	12.89
Ba	6.99	136.61	53.65	82.40	142.18
Th	0.09	1.67	0.56	1.01	1.82
U	0.02	0.41	0.14	0.25	0.45
Nb	0.71	14.05	4.75	8.47	15.18
K	249.98	4908.51	1820.56	2959.94	4171.92
La	0.69	12.50	4.50	7.70	13.51
Ce	1.77	30.00	11.44	18.89	32.74
Pr	0.28	5.27	1.82	3.20	5.39
Sr	21.10	347.09	136.05	220.43	370.19
P	94.98	1268.97	540.84	836.98	1506.04
Nd	1.35	18.64	8.30	12.49	20.75
Zr	11.20	161.90	70.89	107.09	184.74
Sm	0.44	4.68	2.57	3.42	5.39
Eu	0.17	2.62	1.14	1.70	2.78
Ti	1300.24	11573.47	7305.13	8720.65	12999.58
Dy	0.74	3.19	3.98	3.30	4.90
Y	4.55	18.35	24.07	19.37	28.91
Yb	0.49	1.16	2.58	1.49	2.35
Lu	0.07	0.14	0.36	0.19	0.29

*1 PM: primitive mantle composition (Sun and McDonough, 1989), PS Lhz: garnet-spinel Lherzolite
*2 NMBM: Non-Modal Batch Melting
*3 5% partial melting of garnet-spinel Lherzolite (Mode-I, Supplementary Item 3, Table 2)
*4 15% partial melting of phlogopite-bearing garnet-spinel Lherzolite (Mode-II, Supplementary Item 3, Table 2)
*5 EM: mixing between mantle-derived magmas
*6 Residual melt of fractional crystallization of 0.5 Ol + 0.35 Cpx + 0.1 Am ± 0.05 Apt from enriched mantle magma

References

Cabanis, B., Lecolle, M., 1989. Le diagramme La/10-Y/15-Nb/8: un outil pour la discrimination des séries volcaniques et lamise en évidence des processus de mélange et/ou de contamination crustale. Comptes Rendus Academie de Sciences Paris Serie II, 309, 2023−2029.

Ersoy, E.Y, Helvachi, C., Palmer, M.R. 2010. Mantle source characteristics and melting models for the early-middle Miocene mafic volcanism in Western Anatolia: implications for enrichment processes of mantle lithosphere and origin of K-rich volcanism in post-collisional settings. Journal of Volcanology and Geothermal Research 198, 112–128.

Foley, S.F., Jackson, S.E., Fryer, B.J., Greenough, J.D., Jenner, G.A., 1996. Trace element partition coefficients for clinopyroxene and phlogopite in an alkaline lamprophyre from Newfoundland by LAM-ICP-MS. Geochimica et Cosmochimica Acta 60, 629–638.

Fujimaki, H., Tatsumoto, M., Aoki, K-i, 1984. Partition coefficients of Hf, Zr, and REE between phenocrysts and groundmasses. Journal of Geophysical Research 89, 662–672.

Glazer, S.M., Foley, S.F., Giinther D., 1999. Trace element compositions of minerals in garnet and spinel peridotite xenoliths from the Vitim volcanic field, Transbaikalia, eastern Siberia. Lithos 48, 263–285.

Holland, T., Blundy, J., 1994. Non-ideal interactions in calcic amphiboles and their bearing on amphibole-plagioclase thermometry. Contributions to Mineralogy and Petrology 116, 433–447.

Johnson, K.T.M., 1998. Experimental determination of partition coefficients for rare earth and high-field-strength elements between clinopyroxene, garnet, and basaltic melt at high pressures. Contributions to Mineralogy and Petrology 133, 60-68.

Khalaf, E.A., Khalaf, M., F., 2010. Polybaric evolution of the volcanic rocks at Gabal Nuqara, north eastern desert, Egypt. In: Biswajit Gh., Gautam S., Jyotisnkr R., (eds). Topics in Igneous Petrology, Springer-Verlag, 277-317.

Kelemen, P.B., Shimizu, N., Dunn, T., 1993. Relative depletion of niobium in some arc magmas and the continental crust: partitioning of K, Nb, La, and Ce during melt/rock reaction in the upper mantle. Earth and Planetary Science Letter 120, 111-134.

Leake, B.E., 1978. Nomenclature of amphiboles. American Mineralogist 63, 1023-1052.

Leake, B.E., Woolley, A.R., Birch, W.D., Burke, E.A.J., Ferraris, G., Grice, J.D., Hawthorne, F.C., Kisch, H.J., Krivovichev, V.G., Schumacher, J.C., Stephenson, N.C.N., and Whittaker, E.J.W. (2003) Nomenclature of amphiboles: additions and revisions to the International Mineralogical Association's amphibole nomenclature. American Mineralogist 89, 883-887.

McKenzie, D., O'Nions, R. K., 1991. Partial melt distributions from inversion of rare earth element concentrations. Journal of Petrology 32, 1021–1091.

Okamoto, K., 1979. Geochemical study on magmatic differentiation of Asama Volcano, central Japan. Journal of the Geological Society of Japan 85, 8, 525–535.

Pearce, J.A., Norry, M.J., 1979. Petrogenetic implications of Ti, Zr, Y, and Nb variations in volcanic rocks. Contributions to Mineralogy and Petrology 69, 33–47.

Pearce, J.A., 1983. Role of the sub-continental lithosphere in magma genesis at acrive continental margins: p. 230-249 in, Hawkesworth, C.J. and Norry, M.J., eds., Continental Basalts and Mantle Xenoliths, Shiva Publishing Ltd., Cambridge, Mass., 272 p.

Schmidt, M.W., 1992. Amphibole composition in tonalite as a function of pressure: an experimental calibration of the Al-in-hornblende barometer. Contributions to Mineralogy and Petrology 110, 304–310.

Watson, E.B., Green, T.H., 1981. Apatite/liquid partition coefficients for the rare earth elements and strontium. Earth Planetary Science Letters 56, 405–421.

Zack, T., Brumm, R., 1998. Ilmenite/liquid partition coefficients of 26 trace elements determined through ilmenite/clinopyroxene partitioning in garnet pyroxene. In: 7th International Kimberlite Conference. Gurney, J.J., Gurney, J.L., Pascoe, M.D. and Richardson, S.H. (Editors), Red Roof Design, Cape Town, 986-988.